TAMPERE UNIVERSITY OF TECHNOLOGY

PEKKA PASANEN

PERFORMANCE OF CENTRIFUGAL PUMP AS A FAN

Master's thesis

Examiner: Professor Reijo Karvinen
Examiner and topic approved by the
Faculty of Science and Environmental
Engineering on 5. December 2012

TIIVISTELMÄ

TAMPEREEN TEKNILLINEN YLIOPISTO
Ympäristö- ja energiatekniikan koulutusohjelma
PEKKA PASANEN: Keskipakopumpun toiminta puhaltimena
Diplomityö, 92 sivua, 12 liitesivua
Syyskuu 2013
Pääaine: Virtaustekniikka
Tarkastajat: Reijo Karvinen
Avainsanat: puhaltimen hyötysuhde, puhaltimen mittaus, rajakerrosanalyysi, pumpun suunnittelu

Tavalliset puhaltimet eivät sovellu kaasun pumppaamiseen korkeapaineisissa järjestelmissä, mikä on johtanut pumppujen käyttämiseen tähän tarkoitukseen. Pumput on alunperin suunniteltu veden pumppaamiseen eikä niiden suorituskyky ilmalla ole ollut tiedossa. Tässä työssä keskipakopumpun suorituskyky ilmalla mitattiin kahdella eri juoksupyörällä. Ilman käyttämistä pumppausnesteenä tutkittiin vertaamalla mittaustuloksia vedellä mitattuihin arvoihin.

Käytetty mittausjärjestelmä suunniteltiin ja rakennettiin alusta alkaen noudattaen puhallinmittausstandardia ISO 5801:2007. Käytettävissä olevien anturien tarkkuus ei ollut riittävä täyttämään standardin vaatimuksia. Työn tarkoituksena oli selvittää pumpun toiminta puhaltimena eikä suorittaa standardoituja mittauksia.

Yksinkertainen tasolevyvirtauksen rajakerrosanalyysi osoitti, että virtauksen kitkakerroin sileällä pinnalla on suurempi ilmalla verrattuna veteen. Pinnankarheuden vaikutus pienentää eroa, koska laminaari alakerros katoaa pinnan ollessa hydraulisesti karhea. Suuri pinnankarheus kasvattaa kitkakerrointa molemmilla virtausaineilla.

Rajakerroksen muuttuminen laminaarista turbulentiksi voi aiheuttaa odottamattomia ilmiöitä juoksupöyrän virtauskanavan sisällä. Rajakerrosanalyysin mukaan ilmavirtaus irtoaa helpommin alhaisemmasta Reynoldsin luvusta johtuen. Virtauksen irtoaminen aiheuttaa häviöitä ja hydraulinen hyötysuhde pienenee merkittävästi.

Mittaustulokset vahvistivat, että pumppua voi käyttää puhaltimena ja toimintakäyrät ovat samankaltaisia. Tuloksina saatiin pumpun toimintakäyrät eri kierrosluvuilla molemmilla juoksupyörillä. Toinen juoksupyörä, jossa on puolikkaat lisäsiivet, tuotti enemmän painetta korkeilla tilavuusvirroilla tavalliseen juoksupyörään verrattuna. Juoksupörän ja kotelon välisen raon koon vaikutus pumpun toimintaan oli mitattavissa, mutta vaikutus ei ole suuri.

Hydraulinen hyötysuhde mitattiin käyttäen momenttimittausta ja termodynaamista menetelmää. Momenttimittaus ei onnistunut, koska laakereihin kohdistuva radiaalivoima ei ollut riittävällä tasolla. Laakerit eivät toimineet oikein ja mitatut kitkatehot olivat liian suuria. Termodynaaminen hyötysuhteen mittaus vahvistaa, että pumpun hydraulinen höytysuhde ilmalla on lähes yhtä hyvä kuin vedellä.

ABSTRACT

TAMPERE UNIVERSITY OF TECHNOLOGY
Master's Degree Programme in Environmental and Energy Technology
PEKKA PASANEN: Performance of Centrifugal Pump as a Fan
Master of Science Thesis, 92 pages, 12 Appendix pages
September 2013
Major: Fluid Dynamics
Examiner: Reijo Karvinen
Keywords: fan efficiency, fan measurement, boundary layer analysis, pump design

The requirements of pumping gas in high pressure environments have led to the use of centrifugal pumps as fans. Pumps are originally designed for pumping water and their performance with air was not known. In this thesis the performance of a centrifugal pump with air was measured with two different impellers. The differences of air and water as a working fluid were studied.

The measurement system was designed and built following the guidelines of the fan measurement standard ISO 5801:2007. The accuracy of the available sensors was not enough to fulfill the requirements of the standard and standardized measurements were not the design target of the measurement system.

A simple flat plate boundary layer analysis showed that the friction coefficient is higher with air on a smooth plate. The surface roughness diminishes the differences because the viscous sublayer disappears in the hydraulically fully rough flow regime. High surface roughness leads to a high friction coefficient with both fluids.

The transition of the boundary layer from laminar to turbulent can have unpredictable effects inside the impeller channel with air and possibly with water in small pumps. The boundary layer analysis also showed that the flow in the impeller channel is more likely to separate with air due to lower Reynolds number. The possible flow separation causes high losses and the hydraulic efficiency deteriorates.

The measurements confirmed that pump can be used as a fan and the operation curves are almost similar. The measurements provided the operation curves of the pump with air at different rotational speeds for both impeller. The impeller with extra half length blades produced higher pressure at high flow rates compared to the normal impeller. The effect of the size of the gap between the impeller and casing was noticeable but not very large.

The fan efficiency measurements were conducted with torque measurement and thermodynamic method. The efficiency measurement with the torque method failed due to insufficient radial load on the bearings. The measured friction power of the bearing unit is too high, because the bearings are not operating correctly. The thermodynamic method showed that the fan efficiency of the pump with air is almost at the same level as the pump hydraulic efficiency with water.

PREFACE

This study was conducted at Tampere University of Technology during the fall 2012 and spring 2013. The measurements were carried out in the laboratory of the Department of Energy and Process Engineering. The measured device was provided by Sulzer Pumps Finland Oy. This work was funded by Tampere University of Technology and EFEU (Efficient Energy Use) program of the CLEEN Cluster for Energy and Environment. The support from Sulzer is greatly appreciated.

The examiner and supervisor for this thesis is professor Reijo Karvinen who has provided valuable insight and guidance during the process. Thanks go to my fellow researchers who have provided valuable feedback and information along the way. For building the measurement system and helping in the designing process, thanks are expressed to laboratory engineer Jarmo Ruusila, without whom the measurement system couldn't have been build. Also many thanks go to Heikki Manninen from Sulzer Pumps firstly for providing the pump device and the research problem and secondly for answering the questions that arose and for providing invaluable insight to the pumping process.

Last but certainly not least I would like to express my greatest gratitude to my beloved fiancée Emilia for withstanding this lengthy process and providing support all along the way and thanks to my little girls Aura and Sara for letting daddy to work so much with the thesis.

Tampere, September 25th

Pekka Pasanen

CONTENTS

LIST OF TERMS AND ABBREVIATIONS

Greek letters

θ momentum thickness [m]

k_{ps} compressibility coefficient

α angle between peripheral and absolute velocity [°]
flow rate coefficient (Chapter 5)

β angle between peripheral and relative velocity [°]
orifice plate diameter ratio parameter (Chapter 4)

δ shaft deflection [m]

η efficiency [%]

η_e electrical or total efficiency [%]

η_h hydraulic efficiency [%]

η_r impeller efficiency [%]

η_v volumetric efficiency [%]

γ slip factor

κ isentropic exponent for an ideal gas

λ_{La} impeller blade inclination angle [°]

μ dynamic viscosity [kg/sm]

ν kinematic viscosity [m^2/s]

ω angular velocity [rad/s]

ϕ dimensionless flow coefficient

ψ dimensionless pressure coefficient

ρ density [kg/m^3]

τ impeller blade blockage factor

τ_s shear stress [N/m^2]

τ_w shear stress at the wall [N/m^2]

τ_{al} allowable shear stress of material [Pa]

Θ absolute temperature [K]

ε expansibility factor

ξ conventional friction coefficient

Superscripts and subscripts

* dimensionless value, length is referred to d_2 and velocity to u_2

$_1$ impeller inlet
control volume inlet (Chapter 2)
fan inlet plane (Chapter 5)

$_2$ impeller outlet
control volume outlet (Chapter 2)
fan outlet plane (Chapter 5)

$_3$ fan inlet pressure measurement plane
$_7$ pressure measurement plane upstream of orifice plate
$_a$ air
ambient

$_B$ variable of the impeller
$_D$ ISO 5801:2007 installation category
$_e$ gauge pressure value
$_m$ meridional velocity component [m/s]
$_r$ rough surface
$_u$ peripheral velocity component [m/s]
upstream (Chapter 5)
$_w$ water
$_\infty$ blade congruent flow
$_{bear}$ bearing
$_{do}$ downstream
$_{fric}$ friction
$_{i,m,a}$ inner, mean and outer streamline
$_{lam}$ laminar
$_{La}$ impeller
$_{max}$ maximum
$_{opt}$ design or best efficiency point operation conditions
$_{ref}$ reference value
$_{seal}$ seal
$_{sg}$ stagnation condition
$_{spec}$ specific
$_{st}$ static
$_{th}$ theoretical
$_{turb}$ turbulent

Other symbols

$\dot{m}$ mass flow rate [kg/s]
$\dot{Q}$ heat flux [W]
$\dot{W}_c$ absorbed work flux [W]
A area [m^2]
B systematic error
b impeller width in meridional section [m]
b_c Coriolis acceleration [m/s^2]
b_z total centrifugal acceleration [m/s^2]
c flow velocity in absolute reference frame [m/s]

C_D total friction or drag coefficient
C_f friction coefficient
c_p specific mass heat capasity in constant pressure [J/kgK]
c_V specific mass heat capasity in constant volume [J/kgK]
D pipe inner diameter [m]
d diameter [m]
orifice plate hole diameter (Chapter 4) [m]
d_d pump outlet inner diameter [m]
d_n impeller hub diameter [m]
d_s pump inlet inner diameter [m]
d_w pump shaft diameter [m]
E total energy [J]
modulus of elasticity (Chapter 5) [Pa]
e impeller blade thickness [m]
F force [N]
f_M Mach correction factor
f_q number of impeller flow entries
g acceleration due to gravity [m/s^2]
H hydraulic head [m]
h enthalpy [kJ/kgK]
h_0 stagnation enthalpy [kJ/kgK]
h_u relative humidity [%]
i incidence angle [°]
I_z the area moment of inertia [m^4]
I_{Tu} turbulence intensity
k_{eq} equivalent sand grain roughness height [m]
L length [m]
L_p impeller blade tip curvature length [m]
M torque [Nm]
molar mass (Chapter 5) [mol/g]
m mass [kg]
M_a torque on pump shaft [Nm]
M_r torque on impeller [Nm]
Ma Mach number
n_q specific speed (dimensional) [$m^{3/4}/s^{3/2}$]
P power [W]
p pressure [Pa]
P_a shaft power [W]
p_d dynamic pressure [Pa]

P_e electrical power, total input power [W]
p_f fan pressure [Pa]
P_L leakage power loss [W]
P_m mechanical power loss [W]
P_r impeller power [W]
P_u useful power, air power [W]
p_v partial water vapor pressure [Pa]
P_{rec} recirculation power loss [W]
P_{RR} disk friction power loss [W]
p_{sat} saturation pressure [Pa]
p_{sf} static fan pressure [Pa]
Q volumetric flow rate [m^3/h] or [m^3/s]
thermal energy [J]
q_m mass flow rate [kg/s]
q_V volumetric flow rate [m^3/s]
Q_E axial thrust balancing device leakage volumetric flow rate [m^3/s]
Q_h auxiliary leakage volumetric flow rate [m^3/s]
Q_{sp} impeller leakage volumetric flow rate [m^3/s]
R specific gas constant of dry air [J/kgK]
radius [m]
r radius [m]
R_u universal gas constant [J/molK]
R_v specific gas constant of water vapor [J/kgK]
R_w specific gas constant of humid air [J/kgK]
R_{sl} momentary streamline curvature [m]
Re_D pipe flow Reynolds number
Re_k roughness Reynolds number
Re_L flat plate Reynolds number the trailing edge
Re_x flat plate Reynolds number at distance x from the leading edge
$Re_{x,crit}$ critical flat plate Reynolds number at distance x from the leading edge
S entropy [J/K]
s standard deviation
T temperature [K] or [C°]
t time [s]
T_d dry bulb temperature [C°]
T_w wet bulb temperature [C°]
t_{95} t-distribution coefficient forthe 95
U internal energy [J]
absoluter error (Chapter 5)

u peripheral velocity [m/s]
specific internal energy [J/kg]
relative error (Chapter 5)
u_∞ freestream velocity [m/s]
u_τ friction velocity [m/s]
V volume [m^3]
v specific volume [m^3/kg]
v_D flow velocity in a pipe [m/s]
W work [J]
w flow velocity in relative reference frame [m/s]
x x-coordinate [m]
y y-coordinate [m]
Y_{th} theoretical work per unit mass [J/kg]
z z-coordinate [m]
z_{La} impeller blade number

Abbreviations

BEP best efficiency point
CAD computer aided design
CFD computational fluid dynamics
DS or PS pressure side on the impeller blade
DTC direct torque control
FEM finite element method
GUI graphical user interface
NPSHr net positive suction head (required) [m]
PIV particle image velocimetry
PWM pulse width modulation
RTD resistance temperature detector
SS suction side of the impeller blade

1. INTRODUCTION

In this chapter the research topic and measured device are introduced. The motivation for the research is briefly discussed first and details about the pump are presented. The measured pump reference operating conditions and performance curves with water are presented. The goal of this chapter is to introduce the reader to the topic and to measured devices.

1.1 Research motivation and fundamentals

Traditionally pumps and fans are considered to be different machine types in the process industry, although they are both based on the same flow phenomena and design principles. This thesis aims to explore the difference between the types by studying how a process pump will perform if it's used as a fan. The pump used for this work is a typical small process pump that is generally used for pumping water.

The reason for this study is that certain industrial processes require a fan which doesn't leak and can operate under high pressure. Fans that can operate under high pressure don't exists and this has led to an idea to use a process pump for pumping gas too. Process pumps have better seals than fans since they need to keep the fluid from leaking and they are already designed to generate and withstand much higher pressure than fans. These properties make pumps suitable for pumping pressurized gas.

The turbo-machinery principles are the same for fans and pumps, thus pump should work similarly as a fan. Basic pump theory indicates that only the required input power should change as the density of the fluid changes, not the generated flow rate and hydraulic head. This study aims to find out how pump works as a fan.

Research method used in this work is mainly experimental, since the pump operating and efficiency curves with air are of main interest. A large part of the thesis consists of designing and implementing a fan performance measuring system which is designed according to the international standard ISO5801:2007. Standardized measuring system design is used because it ensures the quality of the results and enables the use of the measuring system for further research and development. In theoretical part, general pumping theory is briefly reviewed and possible effects of fluid viscosity are considered by utilizing simplified boundary layer analysis to analyze the effect of fluid properties and surface roughness on skin friction. A basic

fan impeller design process is also made using conventional pump design methods to find out the differences in hydrodynamic design between a fan and a pump.

Pump operation with air provides insight to the entire flow phenomenon inside the pump. This information can be used to further improve pump design and operation. Measurements using air could be used in the initial design stage of new impellers and pumps. Measurement system designed for air is more versatile, cheaper and easier to construct than a similar system for water, because the pressure levels and power requirements are much lower. Test impellers can be made from lighter materials and are much cheaper and faster to manufacture. Cheaper and faster experimental testing allows pump designers to use more creative and out of the box ideas which could lead to innovations and improved performance.

1.2 Measured device

1.2.1 Mechanical structure

The pump studied in the thesis is a typical process industry pump and is manufactured by Sulzer Pumps Ltd. The pump is from the ALHSTAR A -series and the exact model is A32-100 O. The pump is a single stage centrifugal pump with a spiral single volute and the impeller design is almost radial. Two different impellers are used and both of them are semi-open type. The pump has a double mechanical seal and a grease lubricated bearing unit. An illustration of an AHLSTAR A -series pump is presented in Figure 1.1.

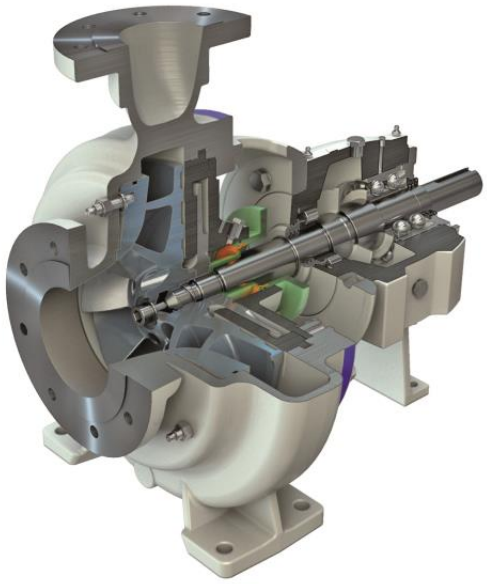

Figure 1.1: *Illustration of AHLSTAR A -series pump [25].*

.

After initial measurements it was concluded that the original bearing unit is too heavy duty for fan usage as it has very large bearing friction which disturbs efficiency measurements. The bearing unit was changed to an alternative one which has ball bearings instead of roller bearings. After the switch, bearing friction was significantly reduced. All final measurement results presented in this thesis are measured using the lighter bearing unit unless stated otherwise. The bearing unit friction losses are an important part of the total friction losses. An illustration of a grease lubricated original bearing unit is shown in Figure 1.2.

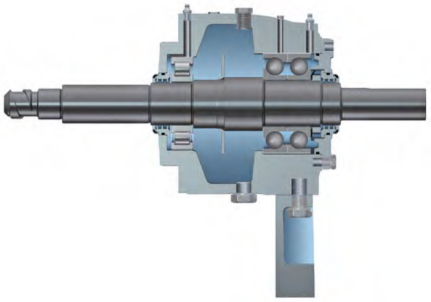

Figure 1.2: *Illustration of bearing unit of an AHLSTAR A -series pump [25].*

The pump is equipped with a double mechanical seal for preventing the pressurized gas from leaking out. The seal type is an Optimal Bore Sulzer Double Mechanical Seal which is a patented structure and an illustration is shown in Figure 1.3.

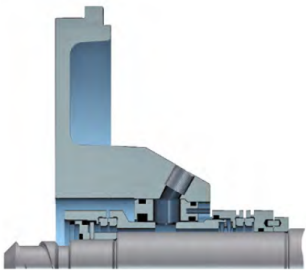

Figure 1.3: *Illustration of Optimal Bore Sulzer Double Mechanical Seal [25].*

The seal consists of two seal face pairs, one just behind the impeller and the other in front of the bearing unit. The seal chamber is flushed with water in order to cool down the seal faces and to lubricate the contact. Sealing liquid flow rate is kept constant with a flow rate of ≥ 2 l/min and the seal chamber is also slightly pressurized in order to ensure liquid penetration between the slip surfaces. The seal chamber pressure level is set to 0,5 bar over atmospheric pressure.

The impellers used in the measurements are both semi-open type which means that they have a back plate but no front plate. The impellers have balance holes

in the center which are used to reduce the axial thrust due to pressure difference over the impeller. The balance holes are not necessary when pump is used as a fan, because with gas the pressure level is only a fraction of pressure levels with liquid and axial thrust is minimal. Both impellers have six blades and the second impeller has extra half-length blades on the outer half. One impeller is shown in Figure 1.4. [28]

Figure 1.4: *Picture of a standard semi-open type impeller of measured device.*

1.2.2 Reference performance data

The reference data for the measured device is provided by the pump manufacturer Sulzer and is gathered from an on-line pump selection tool Sulzer Select [27]. The reference data measured with water and according to the standard ISO 9906:2012 with efficiency grade 2B. The reference data is correlated according to the standard and affinity rules are used to provide the operating curves at different rotational speeds [13]. Geometry data of the pump is shown in Table 1.1, where d_2 is the impeller outer diameter, d_s is the pump inlet inner diameter and d_d is the pump outlet inner diameter. [26, 27]

Table 1.1: *Sulzer AHLSTAR A32-100 O pump data, geometry.*

Property	d_2 [mm]	d_s [mm]	d_d [mm]
Value	330	125	100

The rated flow point or the Best Efficiency Point (BEP) operating conditions are

listed in Table 1.2 [27]. In addition to the BEP, the operation and performance curve for whole operation range at 2960 rpm is presented in Figure 1.5.

Table 1.2: *Sulzer AHLSTAR A32-100 O pump data, BEP-conditions.*

Property	H [m]	Q [m^3/h]	n [1/min]	η [%]	NPSHr [m]
Value	147,4	416,1	2960	81,98	6,29

In Table 1.2, the NPSHr stands for the Net Positive Suction Head required, which means that at BEP there must be at least 6,29 m of net positive suction head present in the system in order to prevent cavitation. The operation and performance curves were provided in spreadsheet format to the author by Sulzer and that data is used in Chapter 6 for comparison between the measured data.

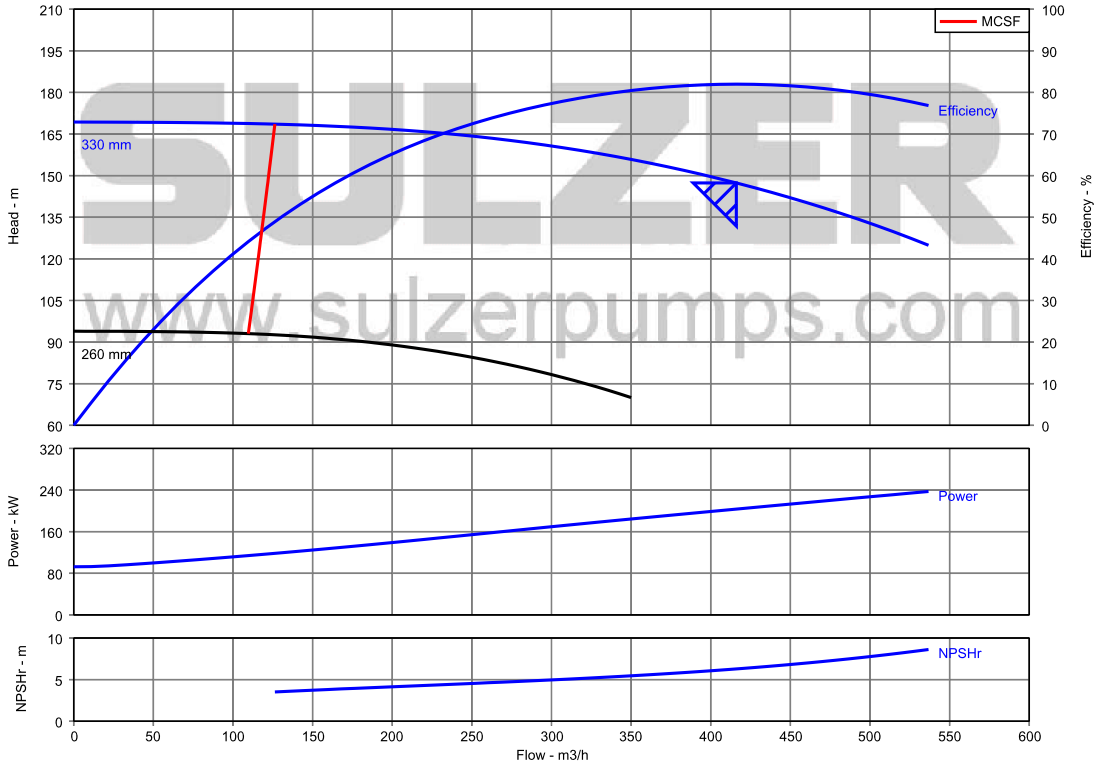

Figure 1.5: *Sulzer AHLSTAR A32-100 O operation and performance curve at* 2960 rpm *[27].*

2. THEORETICAL BACKGROUND

In this chapter the general theory regarding fluid flow in turbo-machines is briefly introduced. The common definitions, the velocity triangles and the conservation laws are presented first and the pump losses are discussed. An analysis of the effect of fluid properties is made mainly by simplified boundary layer analysis and the effect of fluid properties on the skin friction and the secondary losses is estimated.

2.1 Theoretical background regarding turbo-machinery

2.1.1 Pump operation

A pump or a fan can be described as a device which transforms mechanical energy into the energy of the fluid. The energy source is usually an electric motor and power is transmitted via a shaft to a rotating impeller with blades and from the blades further into the fluid. During this process several losses are present at each stage and energy is lost due to friction and volumetric losses. The transmitted useful energy is mostly in the form of pressure and kinetic energy of the fluid. [7, 9]

The purpose of the turbo-machine is to raise the fluid pressure to such level that it overcomes the upstream resistance, for instance the hydraulic losses in a pipeline, and generates a high enough flow rate through the system for the given purpose [28]. The surrounding system and its operation conditions determine the overall operation point and the pump merely adapts to this. The operation point of the pumping system is then formed to the point where the system operation curve and the pump operation curve intersect. [9, 28]

2.1.2 Common definitions

There are several commonly used definitions regarding turbo-machinery, which might not be familiar to the reader. The definition of the impeller dimensions is presented in Appendix A. Dimensional analysis has been used to derive some of the definitions in the past and they are still commonly used and most useful regarding turbo-machinery. It should be noted that it is a common practice to neglect the fluid viscosity and density when these basic definitions are derived. This might lead to errors in some cases as the measurement results suggest, but when the definitions and laws are used in the correct way they are perfectly applicable.

The first definition is the hydraulic head H presented in equation (2.1), where Δp is the pressure rise, ρ is the density of the fluid and g is the acceleration due to gravity and has the value $g = 9{,}81\,\mathrm{m/s^2}$. The pump operation curves are usually presented as a function of the hydraulic head H and the volumetric flow rate Q. Hydraulic head has the dimensions $[H] =$ m and it describes the practical pumping capability of the pump. [9, 17]

$$H = \frac{\Delta p}{\rho g} \tag{2.1}$$

Second definition is the specific speed n_q which is an important parameter and is widely used. The specific speed has many slightly different definitions and the most common and the one that is used in the thesis is presented in equation (2.2), where n is the rotational speed of the pump $[n] =$ rpm, Q_{opt} is the volumetric flow rate and H_{opt} is the hydraulic head at the design point. The definition (2.2) is not dimensionless. [9, 17]

$$n_q = n\frac{\sqrt{Q_{opt}}}{H_{opt}^{0,75}} \tag{2.2}$$

The specific speed relates the pump pressure generation to the flow rate and to the rotational speed. The specific speed practically defines the type of the pump. Pumps with small n_q are usually radial centrifugal pumps and pumps with high n_q are semi-axial or totally axial pumps. In general, when the required flow rate rises the specific speed of the pump increases and when the required head is high the specific speed decreases. The specific speed doesn't determine the exact pump dimensions as the design operating conditions can be met with different pump geometries, but it gives an estimation of the pump type for the given application. [9, 17]

From the dimensional analysis and the assumption of geometrical similarity, it is possible to derive scaling laws for two differently sized but otherwise similar pumps. These scaling laws are known as the affinity laws and they are presented in equations (2.3) and (2.4), where the subscripts 1 and 2 correspond to the different sizes and d is the impeller diameter. [17]

$$\frac{Q_1}{Q_2} = \left(\frac{d_1}{d_2}\right)^3 \left(\frac{n_1}{n_2}\right) \tag{2.3}$$

$$\frac{H_1}{H_2} = \left(\frac{d_1}{d_2}\right)^2 \left(\frac{n_1}{n_2}\right)^2 \tag{2.4}$$

From the assumption of geometrical similarity it is also possible to define the dimensionless flow coefficient φ and the pressure coefficient ψ. These definitions are based on the velocity triangles, which are presented in the subsection below. The flow coefficient determines the amount of the volumetric flow rate scaled by the peripheral speed u. The volumetric flow rate is determined by the meridional flow

velocity component c_m and this leads to equation (2.5). The flow coefficient can be calculated at the impeller inlet and outlet. The pressure coefficient is defined by equation (2.6) at the impeller outlet and the pressure rise is scaled by the outlet peripheral speed u_2. [7, 9]

$$\varphi = \frac{c_m}{u} \tag{2.5}$$

$$\psi = \frac{2gH}{u_2^2} \tag{2.6}$$

The flow and pressure coefficients can be used to present the pump operating curves in a dimensionless form. Their use is still not widely adopted in the industry and conventional $H - Q$ -curves are still dominant. The dimensionless coefficients are useful in presenting experimental results and correlations, and they are widely used in that purpose. [9]

2.1.3 Velocity triangles

The basic theoretical analysis of the fluid flow in turbo-machines relies heavily on the concept of velocity triangles. The velocity triangles define the direction of the fluid flow in the absolute and relative reference frames and the connection between the velocity vectors. The relative reference frame is a rotating reference frame where the fluid velocity is relative to the rotating impeller surface is denoted by $\bar{w}$. In the absolute reference frame the fluid velocity is denoted by $\bar{c}$ and the peripheral velocity vector is $\bar{u}$. The relation between the different velocities is illustrated with a vector diagram in Figure 2.1 and in Figure 2.2. [7, 9, 17]

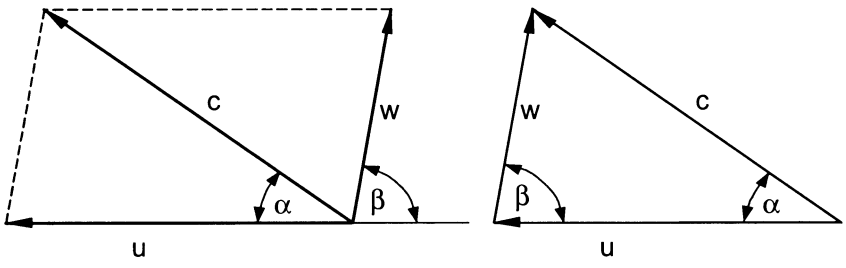

Figure 2.1: *Fluid flow vector diagram [9].*

The velocity vectors defined in Figure 2.1 define the angles between the velocities. The angle α is the angle between the absolute velocity $\bar{c}$ and the peripheral or tangential velocity $\bar{u}$ and is the real flow angle in absolute reference frame. The angle β is the angle between the relative velocity $\bar{w}$ and the peripheral velocity $\bar{u}$ and is the relative flow angle in the rotating reference frame. The velocity triangles can be used to determine the impeller blade angles β_B at the impeller inlet and outlet . The connection between the velocity vectors and the absolute and relative

reference frame is defined by equation (2.7). [7, 9, 17]

$$\bar{c} = \bar{u} + \bar{w} \quad \Rightarrow \quad \bar{w} = \bar{c} - \bar{u} \tag{2.7}$$

By using the flow angles it is possible to define different components of the absolute flow velocity vector $\bar{c}$. The peripheral component $\bar{c}_u$ is the absolute velocity component parallel to $\bar{u}$ and $\bar{c}_m$ is the meridional component which is perpendicular to $\bar{u}$. The velocity vector components are presented in Figure 2.2. [9, 17]

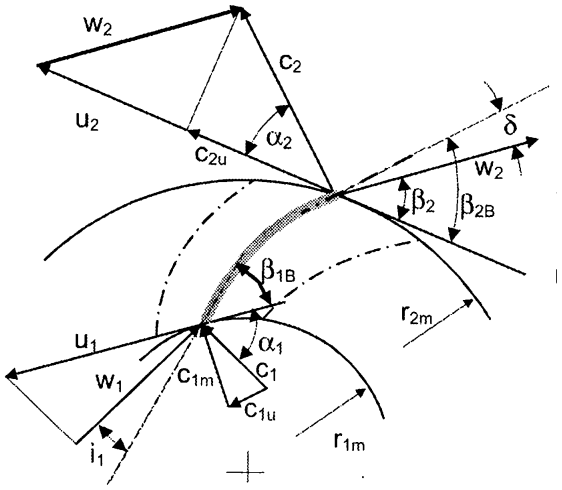

Figure 2.2: *Fluid flow velocity vector components at the inlet and outlet [9].*

The peripheral velocity u is defined by equation (2.8), where ω is the angular velocity, r is the radius and n is the rotational speed and $[n] =$ rpm. [9, 17]

$$u = \omega r = 2\pi \frac{n}{60} r = \pi d \frac{n}{60} \tag{2.8}$$

The meridional flow component is related to the volumetric flow rate by equation (2.8), where Q_{La} is the volumetric flow rate through the impeller, d is the diameter and b is the impeller width in the meridional section. The relation of the meridional flow component to the peripheral velocity component is defined by equation (2.10). [9, 17]

$$c_m = \frac{Q_{La}}{\pi d b} \tag{2.9}$$

$$c_u = \frac{c_m}{\tan \alpha} \tag{2.10}$$

The connection between the relative angle β and the absolute flow velocity components is defined by equation (2.11). The relative velocity can also be determined by using Pythagoras' theorem which yields equation (2.12). The law of cosines gives

another connection between the velocities which is defined by equation (2.13). [9, 17]

$$\beta = \arctan\left(\frac{c_m}{u - c_u}\right) \tag{2.11}$$

$$w = \sqrt{c_m^2 + (u - c_u)^2} \tag{2.12}$$

$$c^2 = w^2 - u^2 + 2uc_u \tag{2.13}$$

The equations (2.9)–(2.13) along with the equation (2.7) are used to determine the different velocity components and required impeller angles at the pump inlet and outlet. A more detailed introduction to the usage of the velocity triangles and to the impeller flow is presented in Chapter 3.

2.1.4 Conservation laws

The flow of a fluid with density ρ through a one-dimensional control volume with inlet area of A_1 and outlet area of A_2 is considered. The corresponding flow velocities perpendicular to the inlet and outlet are c_1 and c_2. It is assumed that mass is not generated or destroyed within the control volume. The conservation of mass or the equation of continuity is defined by equation (2.14), where $\dot{m}$ is the mass flow rate. The equation of continuity is directly applicable to turbo-machinery once the control volume is placed in between the inlet and the outlet including the pump casing, the volute and the impeller. The density is constant if water is used and $\rho = \rho_1 = \rho_2$. [5, 7, 9]

$$\dot{m} = \rho_1 c_1 A_1 = \rho_2 c_2 A_2 \tag{2.14}$$

The conservation of energy can be derived from the first law of thermodynamics. The first law of thermodynamics states that during a complete cycle the sum of the heat supplied to the system and the work done by the system is zero which is defined by equation (2.15). [5, 7]

$$\oint (dQ - dW) = 0 \tag{2.15}$$

If the system state changes, the energy in the system also changes. This is defined by equation (2.16), where $E = U + \frac{1}{2}mc^2 + mgz$ is the total energy of the system. U is the internal energy, $\frac{1}{2}mc^2$ the kinetic energy and mgz is the potential energy. [5, 7]

$$E_2 - E_1 = \oint_1^2 (dQ - dW) \quad \Rightarrow \quad dE = dQ - dW \tag{2.16}$$

Applying equation (2.16) to a fluid flow through a one-dimensional control volume

yields the steady flow energy equation (2.17), where h is the specific enthalpy. [5, 7]

$$\dot{Q} - \dot{W} = \dot{m} \left[(h_2 - h_1) + \frac{1}{2} \left(c_2^2 - c_1^2 \right) + g \left(z_2 - z_1 \right) \right] \tag{2.17}$$

The specific enthalpy is defined by equation (2.18), where $u = U/m$ is the specific internal energy, p is the static pressure and $v = V/m = 1/\rho$ is the specific volume. The specific enthalpy thus includes the pressure energy and thermal energy of the fluid flow. In practice, all the losses in a pump are ultimately converted to heat through viscous dissipation and this increases the internal energy u. [5, 7]

$$h = u + pv \tag{2.18}$$

The stagnation enthalpy h_0 is the combination of the specific enthalpy and the kinetic energy and is defined by equation (2.19). The definition of the stagnation enthalpy is very useful when dealing with compressible fluid flow since it contains the total energy of the fluid flow excluding the potential energy. [7]

$$h_0 = h + \frac{1}{2} c^2 \tag{2.19}$$

The potential energy $g(z_2 - z_1)$ is commonly neglected since its contribution to the total energy balance is very small when the control volume only consists of the turbo-machine. Another commonly made assumption is that the flow through the turbo-machine is adiabatic and the heat flux through the casing is zero implying $\dot{Q} = 0$. [7, 9]

These assumptions together with the definition of the stagnation enthalpy lead to a compact form of the steady flow energy equation which is presented in (2.20). The negative sign in the front of the work flow means that work has to be done to the system in order to increase the enthalpy of the fluid and it's convenient to define the absorbed work flow as $\dot{W}_c$. [5, 7]

$$-\dot{W} = \dot{W}_c = P_r = \dot{m} \left(h_{0,2} - h_{0,1} \right) \tag{2.20}$$

Equation (2.20) is valid for compressible and incompressible flow and for inviscid and viscous flow. It is the common form of the steady energy flow equation. The calculation of the compressible flow relations is presented in detail in Chapter 5.

Using the second law of thermodynamics it is possible to derive equation (2.21), where dS is the change of entropy. Using the definition of specific enthalpy (2.18) with equation (2.21) leads to equation (2.22) for incompressible flow. [5, 7]

$$TdS = du + pdv \tag{2.21}$$

$$TdS = dh - vdp \tag{2.22}$$

For adiabatic incompressible flow with no work transfer the steady state energy equation takes the form (2.23) [7].

$$(h_2 - h_1) + \frac{1}{2}\left(c_2^2 - c_1^2\right) + g\left(z_2 - z_1\right) = 0 \tag{2.23}$$

Differentiating equation (2.23) leads to equation (2.24).

$$dh + cdc + gdz = 0 \tag{2.24}$$

In the case of inviscid fluid flow there are no friction losses and the process is isentropic and $dS = 0$. This leads to the definition $dh = vdp = dp/\rho$ for incompressible flow according to equation (2.22) and further using this information with equation (2.24) leads to equation (2.25). Integrating equation (2.25) over the control volume leads to equation (2.26), which is the Bernoulli's equation for incompressible flow. [7, 9]

$$\frac{1}{\rho}dp + cdc + gdz = 0 \tag{2.25}$$

$$\frac{1}{\rho}\left(p_2 - p_1\right) + \frac{1}{2}\left(c_2^2 - c_1^2\right) + g\left(z_2 - z_1\right) = 0 \tag{2.26}$$

Theoretical work of the pump per unit mass Y_{th} with no losses can be expressed using the Bernoulli's equation (2.27). [9]

$$\frac{P_{th}}{\dot{m}} = Y_{th} = \frac{1}{\rho}\left(p_2 - p_1\right) + \frac{1}{2}\left(c_2^2 - c_1^2\right) + g\left(z_2 - z_1\right) \tag{2.27}$$

The conservation of momentum yields an especially useful result when applied to turbo-machinery. Newton's second law of motion relates the sum of the external forces acting on the mass of a control volume to its acceleration. The sum of all external forces in an arbitrary direction x is equal to the time rate of change of momentum in the same direction which is defined by equation (2.28).

$$\sum F_x = \frac{d}{dt}\left(mc_x\right) \tag{2.28}$$

Applying equation (2.28) to a control volume with a steady mass flow leads to equation (2.29) when the fluid enters the control volume at velocity c_{1x} and leaves at velocity c_{2x}. Equation (2.29) is called the one-dimensional steady flow momentum equation. [7]

$$\sum F_x = \dot{m}\left(c_{1x} - c_{2x}\right) \tag{2.29}$$

Newton's second law of motion can also be applied in the form of moments of forces. The vector sum of the moments of forces about an arbitrary axis a acting

on a mass m of the control volume equals to the time rate of change of angular momentum of the system about the same axis. The natural choice for the moment axis regarding turbo-machinery is the pump shaft going through the impeller and the moment of forces about that axis are perpendicular to both the axis and the radial vector r. This perpendicular velocity component is called c_u. The moment about the pump shaft axis M_r is defined by equation (2.30), where r is the radial distance of the mass center from the axis. [7]

$$r \sum F_u = M_{r,th} \tag{2.30}$$

Applying equation (2.30) to a control volume with steady mass flow rate yields the steady state equation of moment of momentum for the turbo-machine control volume, which is defined by (2.31). [7]

$$M_{r,th} == m \frac{d}{dt} (r c_u) = \dot{m} (r_2 c_{2u} - r_1 c_{2u}) \tag{2.31}$$

Multiplying equation (2.31) with the angular velocity ω and noting that the peripheral speed is $u = \omega r$ leads to equation (2.32) and this form of the momentum conservation is known as the Euler's pump equation. The Euler's pump equation is the ideal situation where no losses are included and it describes the theoretical work of the pump. From equation (2.32) it is clear that stationary blades cannot transfer work to the fluid. [7, 9]

$$\omega M_{r,th} = P_{r,th} = \dot{m} (u_2 c_{2u} - u_1 c_{1u}) \tag{2.32}$$

Using equations (2.27) and (2.32) and substituting equation (2.13) it's possible to derive equation (2.33) for the theoretical total pressure rise in the impeller. The change in potential energy has been ignored. [9]

$$\begin{aligned}
u_2 c_{2u} - u_1 c_{1u} &= \frac{1}{\rho} (p_2 - p_1) + \frac{1}{2} \left(c_2^2 - c_1^2\right) \quad \Leftrightarrow \\
u_2 c_{2u} - u_1 c_{1u} &= \frac{1}{\rho} (p_2 - p_1) + \frac{1}{2} \left(w_2^2 - u_2^2 + 2u_2 c_{2u} - w_1^2 + u_1^2 - 2u_1 c_{1u}\right) \quad \Leftrightarrow \\
-\frac{1}{\rho} (p_2 - p_1) &= \frac{1}{2} \left(w_2^2 - w_1^2 - u_2^2 + u_1^2\right) \quad \Leftrightarrow \\
p_2 - p_1 &= \frac{1}{2} \rho \left(w_1^2 - w_2^2\right) + \frac{1}{2} \rho \left(u_2^2 - u_1^2\right)
\end{aligned} \tag{2.33}$$

2.1.5 Fluid motion through impeller

Flow on a curved path creates a positive pressure gradient according to equation (2.34). The derivation of equation (2.34) is based on the force balance of a

fluid element moving along a curved path. The force balance requires that the centrifugal acceleration is balanced and a positive pressure gradient is generated. Equation (2.34) states that the pressure increases with the radius. The force resulting from the pressure difference provides the balancing centripetal acceleration for the fluid element. [7, 9]

$$\frac{dp}{dr} = \rho\frac{c^2}{r} \tag{2.34}$$

The fluid flow through the impeller follows a spiraling curved path in the absolute reference frame and a curved path between the blades in the relative reference frame. In the relative reference frame the equilibrium of forces is defined by the differential equation (2.35), where b_c is the Coriolis acceleration and b_z is the total centrifugal acceleration, which consist of the centrifugal acceleration and the effect of the momentary streamline curvature R_{sl}. The balance of forces and the relation to the relative flow angle β is illustrated in Figure 2.3.

$$\frac{1}{\rho}\frac{\partial p}{\partial r} = b_c + b_z = 2\omega w + r\omega^2\frac{\partial r}{\partial n} - \frac{w^2}{R_{sl}} \tag{2.35}$$

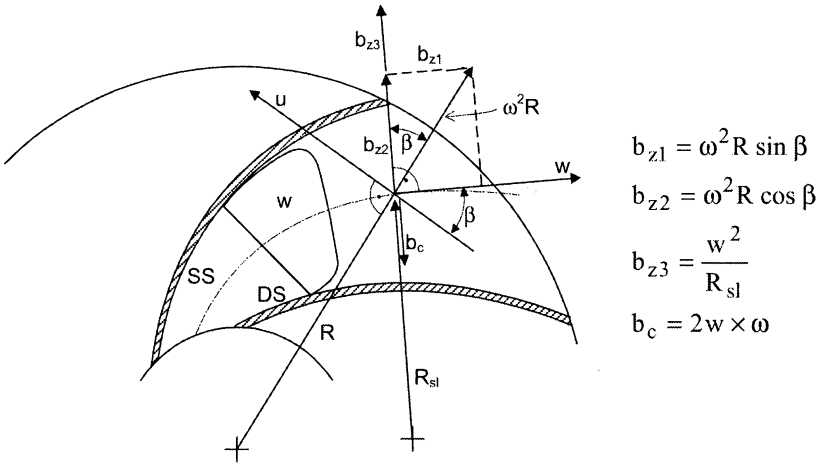

Figure 2.3: *Accelerations acting on a fluid element in the impeller channel [9].*

The Coriolis acceleration is acting in the opposite direction of the centrifugal acceleration. It is important to note that the streamline curvature of the flow generates the static pressure gradient in the pump. The force balance of the fluid element flowing through the impeller is quite complex as can be seen from equation (2.35). The relative velocity w is not constant and neither is the pressure gradient. The meridional curvature provides additional acceleration component to the force balance and in reality three dimensional secondary flows form to fulfill the continuity equation in the impeller channel. [9]

The pressure and suction side of the impeller blades form because the blades generate a non-uniform velocity distribution along the blade in the normal direction of the relative velocity. Integrating the pressure difference along the blades yields the theoretical work per unit mass of the pump. This is the real mechanism how the blade movement is transferred into the energy of the fluid. The Coriolis forces and the centrifugal acceleration enforced by the blades along with the pressure gradient form the delicate and complex equilibrium of forces in the impeller channel. The fluid flow in the impeller channel is always complex and three dimensional because of the secondary flows. [7, 9]

2.2 Pump losses

The total power input P is not fully converted into useful power P_u because of the different losses, which can be divided into external losses and internal losses of the pump. The external losses are the mechanical losses P_m which form in the bearing unit and in the seal. Also the electrical losses in the inverter and the electric motor can be considered as external losses because they are dissipated externally and don't increase the internal energy of the fluid. Traditionally the relative amount of the mechanical losses is small compared to the total power, but when a pump is used as a fan the mechanical losses are significant. [9, 17, 28]

The leakage losses P_L form when the fluid flows back to the impeller inlet from the higher pressure outlet. The leakage flow goes through the annular sealing with closed impellers or the gap between the blades and the casing with semi-open impellers. With semi-open impellers the flow also leaks over the impeller blade from the pressure side to the suction side. The fluid flowing back from the pressure side has to be pumped again and this reduces the efficiency of the pump. The amount of leakage flow is directly proportional to the size of the gap and it's important to keep the gap as small as possible. The leakage flow through the shaft seals and thrust balancing devices is also included in the leakage losses. [9, 17, 28]

The disk friction losses P_{RR} are generated by the skin friction of the rotating impeller surface. The disk friction losses are affected by the surface roughness of the impeller and higher roughness leads to higher disk friction. Higher surface area and rotational speed of the impeller increases the total disk friction which should be taken into account with impeller design. The effect of surface roughness on disk friction with water and air is discussed in more detail in the next section. [9, 17, 28]

The hydraulic losses P_{vh} arise from the viscous dissipation losses. The viscous dissipation converts turbulent fluctuations and velocity gradients into heat. The secondary flows and the uneven flow velocity profiles all contribute to the hydraulic losses. With semi-open impellers the flow over the blade in the gap can be difficult to distinguish from the other hydraulic losses and should be included in them. It is

also possible to define separate recirculation losses P_{rec}, because the flow separation and recirculation cause massive increase in the hydraulic losses. The conversion of velocity into pressure in the diffuser or volute is also subject to the same mixing losses and is included in the total hydraulic losses by definition. [9, 17]

The minimization of the hydraulic and disk friction losses is the key to improving the total pump efficiency. The disk friction losses become increasingly important with small pumps. The hydraulic losses in the pump are mainly determined by the pump geometry and the impeller blade design. The three dimensional flow effects and the secondary flows are hard or impossible to take into account using the one-dimensional design methods and improving the hydraulic efficiency or pump characteristics is a challenging task. [9]

2.3 Boundary layer analysis

The disk friction losses become important when the pump size decreases. Although the fluid flow inside the impeller channel is complex, it is feasible to analyze the skin friction losses using simple flat plate boundary layer theory and assuming a zero pressure gradient in the outer flow. The boundary layer effects of a flat plate have been studied intensively and many useful results for engineering applications have been found using integral methods and similarity. The velocity profile in the wall normal direction along with other quantities have been solved for laminar and turbulent flow. The vast amount of verified experimental results for flat plate flow are important especially for rough surfaces. [23, 30]

In the impeller channel the flow velocity profile does not have time to develop and therefore the boundary layer approach is appropriate. The boundary layer theory is an important and detailed part of fluid dynamics, but in this thesis the analysis is limited to the wall shear stress and the calculation of the friction coefficient and to the flow separation. An illustration of a boundary layer flow velocity profile is presented in Figure 2.4, where $\delta(x)$ is the local boundary layer thickness. [23, 30]

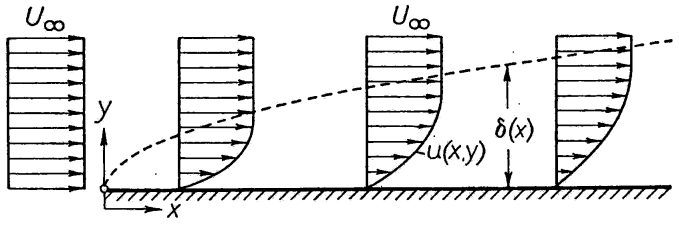

Figure 2.4: *Boundary layer development at a flat plate [23].*

An important factor is the nature of the boundary layer flow. It is a widely used assumption that the boundary layer flow inside turbo-machines is turbulent. This

assumption is valid for water because the flat plate Reynolds number is high, but this might not be the case with air since the flat plate Reynolds number is lower because of the low kinematic viscosity of air. The issue of the boundary transition from laminar to turbulent is also very important and will be discussed below in this section. The flat plate Reynolds number is defined by equation (2.36), where x is the distance from the leading edge and u_∞ is the outer flow velocity. [23, 9]

$$Re_x = \frac{u_\infty x}{\nu} \tag{2.36}$$

2.3.1 Viscosity

The disk friction losses are generated in the boundary layer of the flow where the internal friction of the fluid dissipates kinetic energy into heat. In the boundary layer the flow velocity rapidly decreases from the outer flow velocity to zero at the wall and this generates shear stress between the layers. The dissipated energy is taken away from the kinetic energy of the fluid flow and this causes the friction losses of viscous fluid flows. The dynamic viscosity of the fluid can be thought as the fluids tendency to resist deformation due to external forces. The dynamic viscosity is related to the shear stress τ_s with equation (2.37), where τ_w is the shear stress at the wall. Using an order of magnitude analysis the v-velocity gradient is discarded. [23, 30]

$$\tau_s = \mu\left(\frac{\partial u}{\partial y} + \frac{\partial v}{\partial x}\right) \approx \mu\left(\frac{\partial u}{\partial y}\right) \quad \Rightarrow \quad \tau_w \approx \mu\left(\frac{\partial u}{\partial y}\right)_{y=0} \tag{2.37}$$

Another definition for viscosity is the kinematic viscosity ν. The kinematic viscosity relates the dynamic viscosity to the fluid density ρ and is defined by equation (2.38).

$$\nu = \frac{\mu}{\rho} \tag{2.38}$$

The kinematic viscosity of the fluid is even a more defining parameter in fluid dynamics as it appears for example in the calculation of the Reynolds number. It should be noted that air actually has higher kinematic viscosity than water, because the difference in the dynamic viscosity is not as big as the difference in density. The kinematic viscosity can be thought as the viscous diffusivity of the fluid and it determines how the viscous effects propagate through the fluid, which in turn determines the entire viscous behavior of the flow. [23, 30]

The material properties of air and water are presented in Table 2.1 along with properties of nitrogen for comparison. All material properties are temperature dependent, but the dependency is mild and in the normal operation temperature range of turbo-machines the material properties can be considered constant. The material

properties presented in Table 2.1 are from Basic Heat & Mass Transfer at temperature 300 K. [5, 16]

Table 2.1: *Properties of air, nitrogen and water.*

Fluid	ρ [kg/m^3]	c_p [J/kgK]	$\mu \times 10^6$ [kg/ms]	$\nu \times 10^6$ [m^2/s]
Air	1,177	1005	18,43	15,66
Nitrogen	1,138	1043	17,7	15,5
Water (steam)	0,0255	1870	9,09	356,6
Water (liquid)	996	4178	867	0,87

2.3.2 Friction coefficient

The dimensionless friction coefficient C_f is related to the shear stress at the wall τ_w with equation (2.39). The friction coefficient is a local parameter since the u-velocity gradient in the wall normal direction is not constant and as a result the shear stress at the wall τ_w is a function of x. [23, 30]

$$C_f(x) = \frac{\tau_w(x)}{\frac{1}{2}\rho u_\infty^2} \tag{2.39}$$

The average friction coefficient for a flat plate of length $x = L$ can be calculated by integrating $C_f(x)$ along the x-direction. This produces the total or average drag coefficient C_D for a flat plate which is defined by equation (2.40). [23, 30]

$$C_D = \frac{1}{L}\int_0^L C_f(x)\,dx \tag{2.40}$$

The problem in calculating the friction coefficient directly from equation (2.39) is the unknown shear stress at the wall τ_w, because the u-velocity gradient in the wall normal direction ($\partial u/\partial y$) is generally unknown. This is why integral and similarity solutions of the complete boundary layer equations are used.

A similarity solution for laminar flat plate flow with zero pressure gradient was found by H. Blasius in 1908 and the simple result for laminar flat plate flow friction factor is presented in equation (2.41), where θ is the momentum thickness. The integrated result for the total drag coefficient is presented in equation (2.42). The solution by Blasius is considered to be accurate for flow over smooth laminar flat plate. [23, 30]

$$C_{f,lam} = \frac{0{,}664}{\sqrt{Re_x}} = \frac{\theta}{x} \tag{2.41}$$

$$C_{D,lam} = \frac{1{,}328}{\sqrt{Re_L}} \tag{2.42}$$

With turbulent flow the situation is more complex. Turbulent boundary layers can be analyzed using the Reynolds averaged Navier-Stokes equations, where the instantaneous turbulent velocity fluctuations have been time averaged. Regarding boundary layers, the shear stress has an extra term resulting from the time averaging. For turbulent flow the shear stress is defined by equation (2.43), where the latter term on the right is called the turbulent shear stress. [23, 30]

$$\tau_{s,turb} = \mu \left(\frac{\partial \bar{u}}{\partial y} \right) - \rho \overline{u' v'} \tag{2.43}$$

In the core flow the turbulent shear stress is dominating, because a high velocity gradient in the wall normal direction is only present in the boundary layer. It is therefore fair to assume that the flow is not so dependent on the viscosity of the fluid with turbulent flow. The assumptions made in the dimensional analysis of the pump coefficients are based on this, but this might be questionable when the Reynolds number is smaller and the fluid viscosity effect on the shear stress increases. [30, 17]

There are numerous integral solutions for turbulent flat plate flow. The simplest solutions are based on the so called power-law assumption, which was postulated by Prandtl in 1921 based on the results from pipe flow. The friction coefficient calculated using the power-law assumption is quite accurate, but the accuracy is good only in a limited Reynolds number scale. More precise results for the friction coefficient of turbulent flow over a flat plate have been developed using the inner flow variables.

One such method was developed by Kestin and Persen in 1962, but the original method is quite complex. White developed the method further in 1969 and found an accurate and yet simple result for the turbulent flat plate friction coefficient. The result is presented in equation (2.44) and the integrated total drag coefficient is presented in equation (2.45). These equations are used when the comparison of the friction coefficients are calculated. [30]

$$C_{f,turb} = \frac{0{,}455}{\ln^2 (0{,}06 Re_x)} \tag{2.44}$$

$$C_{D,turb} = \frac{0{,}523}{\ln^2 (0{,}06 Re_L)} \tag{2.45}$$

An important observation is that the friction coefficient increases as the Reynolds number decreases and it effectively means that skin friction is higher with air than with water. This counter-intuitive result is explained by the difference in the kinematic viscosity. The local skin friction coefficient is higher at the beginning of the plate and starts to fall towards the trailing edge. [30]

The effect of surface roughness on friction coefficient

The effects of surface roughness have to be evaluated experimentally because modeling cannot be realistically used to capture the surface roughness. The common way to account for surface roughness is to use the sand grain roughness height k_{eq}. The uniform sand grain roughness height is not similar to the technical roughness of metal surfaces, but equivalent sand grain roughness height values for different materials have been determined. For cast iron surfaces the equivalent sand grain roughness heigth is $k_{eq} = 0{,}25\,\text{mm}$, which is high compared to for example drawn steel with a value $k_{eq} \leq 0{,}03$. [23]

The effect of roughness on the flow is entirely dependent on the height of the roughness elements compared to the boundary layer thickness. If the roughness elements are located entirely in the viscous sublayer of the boundary layer, the effect of roughness is minimal and the surface is called hydraulically smooth. Similarly, if the roughness height exceeds the height of the viscous sublayer layer, the flow is hydraulically fully rough and the effect of fluid viscosity reduces. Between the hydraulically smooth and rough regimes is the transitional phase where the effect of roughness depends on the roughness height. It is possible to define a roughness Reynolds number Re_k by equation (2.46), which is used to describe the effects of surface roughness. [22, 23]

$$Re_k = \frac{u_\infty k_{eq}}{\nu} \tag{2.46}$$

The physical effect of roughness on the boundary layer is that the boundary layer thickness increases and thus the momentum deficit caused by the wall increases. This in turn increases the total friction because the domain of elevated velocity gradient in the wall normal direction is wider. The effect of roughness on the friction coefficient C_f has been investigated experimentally for flat plate and pipe flow.

One useful result which covers the entire roughness regime from hydraulically smooth to fully rough has been developed by White and is presented with equations (2.47)–(2.50). The equation system is implicit in terms on Re_x, C_f and k_{eq}/x and a numerical solution is needed. In equation (2.50), u_τ is the wall-friction velocity. The estimation of the hydraulically smoothness is implicit, because the viscous sublayer thickness depends on the friction coefficient as can be seen from equation (2.50) which contains the wall-friction velocity $u_\tau = \sqrt{\tau_s/\rho}$. [23, 30]

$$Re_x = 1{,}73\left(1 + 0{,}3k^+\right)\exp\left(Z\right)\left[Z^2 - 4Z + 6 - \frac{0{,}3k^+}{1 + 0{,}3k^+}\left(Z - 1\right)\right] \tag{2.47}$$

$$Z = \kappa\lambda \tag{2.48}$$

$$\lambda = \left(\frac{2}{C_f}\right)^{\frac{1}{2}} \tag{2.49}$$

$$k^+ = \frac{k_{eq} u_\tau}{\nu} = \frac{Re_x \, (k_{eq}/x)}{\lambda} \tag{2.50}$$

Simpler correlations exist for the fully rough regime. Schlighting recommends the curve fits presented by equations (2.51) and (2.52) for uniform sand roughness on flat plates. [23, 30]

$$C_{rf,turb} = \left[2{,}87 + 1{,}58 \log_{10} \left(\frac{x}{k_{eq}}\right)\right]^{-2{,}5} \tag{2.51}$$

$$C_{rD,turb} = \left[1{,}89 + 1{,}62 \log_{10} \left(\frac{L}{k_{eq}}\right)\right]^{-2{,}5} \tag{2.52}$$

Example calculation

Theoretical example calculations are presented to compare the effect of the fluid properties and surface roughness on the friction coefficient. In the impeller channel the natural reference for the outer flow velocity u_∞ is the relative flow velocity w which is parallel to the impeller shroud as well as to the blades. A velocity value $u_\infty = w = 20\,\mathrm{m/s}$ is chosen to represent the relative velocity which could be present in a pump used in the measurements. In order to determine the relative velocities in the present pump impeller, the exact blade angles would need to be known and this information is not available. The impeller channel length serves as the length of the boundary layer and the value of $L = 0{,}25\,\mathrm{m}$ is used.

In the calculations it is assumed that the whole boundary layer is turbulent. The local flat plate friction coefficient for air and water is presented in Figure 2.5. Results have been calculated using equation (2.44) and the material properties from Table 2.1.

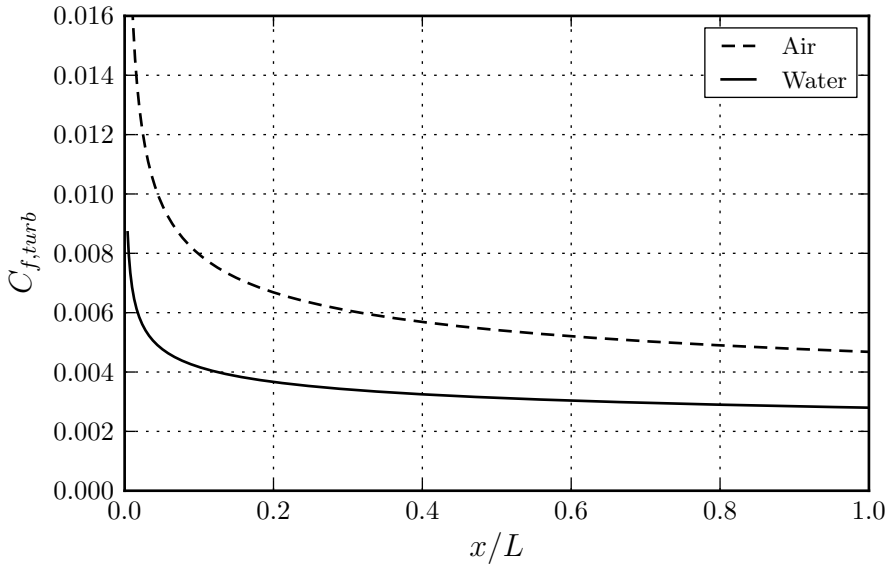

Figure 2.5: *Local friction coefficient for flow over smooth flat plate. Turbulent flow,* $L = 0{,}25\,\mathrm{m}$*,* $u_\infty = 20\,\mathrm{m/s}$*.*

The implicit equation (2.47) is used to estimate the effect of surface roughness on the friction coefficient. The implicit formulation is useful because it solves the friction coefficient for the whole hydraulic roughness regime without information about the hydraulic smoothness. The results using equation (2.47) are presented in Figure 2.6, where the effect of roughness is plotted with two different values of k_{eq}.

When comparing the results in Figure 2.6 and Figure 2.5, it is clear that the friction coefficient is much higher when the surface is rough. Since the friction coefficients are almost identical, another important result is that the flow is in the fully rough regime when $k_{eq} = 0{,}25\,\mathrm{mm}$ and only small differences can be seen when $k_{eq} = 0{,}03\,\mathrm{mm}$. It is therefore perfectly justified to use equations (2.51) and (2.52) to calculate the friction coefficients for a significantly rough surface.

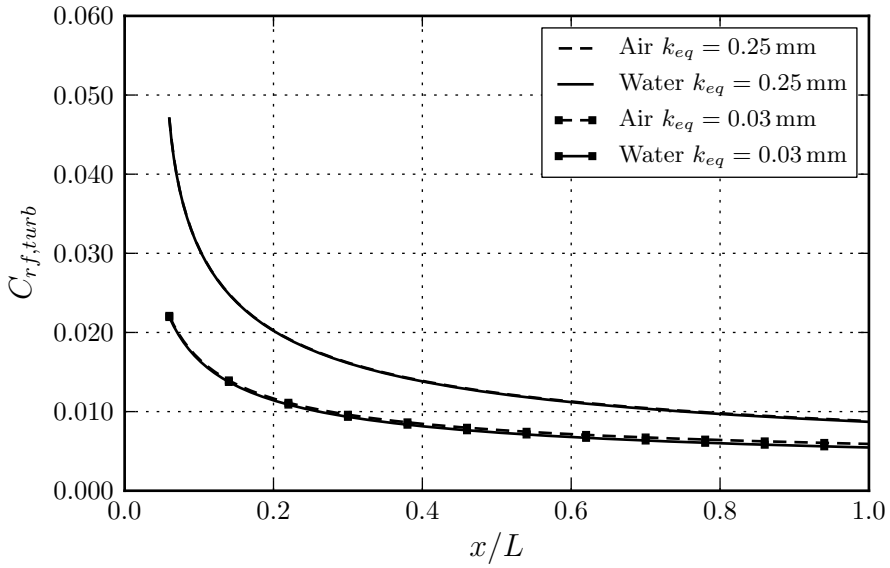

Figure 2.6: *Local friction coefficient for flow over rough flat plate. Turbulent flow,* $L = 0{,}25\,\mathrm{m}$, $u_\infty = 20\,\mathrm{m/s}$, $k_{eq} = 0{,}25\,\mathrm{mm}$ *and* $0{,}03\,\mathrm{mm}$.

The comparison of the mean friction coefficient is presented in Table 2.2. The results have been calculated using equations (2.45) and (2.52). The correlation based on equation (2.52) seems to give lower results for the total friction coefficient than the one based on equation (2.45). This indicates that $k_{eq} = 0{,}03\,\mathrm{mm}$ is already close to a hydraulically smooth surface with air, but not with water.

Table 2.2: *Mean friction coefficient for flow over smooth and rough flat plate. Turbulent flow,* $L = 0{,}25\,\mathrm{m}$, $u_\infty = 20\,\mathrm{m/s}$, $k_{eq} = 0{,}25\,\mathrm{mm}$ *and* $0{,}03\,\mathrm{mm}$.

Fluid and flow condition	C_D
Air (smooth)	0,005379
Water (smooth)	0,003217
Air and water (fully rough, $k_{eq} = 0{,}25\,\mathrm{mm}$)	0,008448
Air and water (fully rough, $k_{eq} = 0{,}03\,\mathrm{mm}$)	0,005128

2.3.3 Boundary layer transition

The boundary layer transition is a complex phenomenon and no universal results have been found because the transition is influenced by numerous factors and the combined effect is difficult to predict. Experiments can provide information how the different factors affect the transition. The most influential factors are the outside pressure gradient, turbulence intensity of the outer flow and surface roughness. [22, 23]

Surface roughness enhances the transition of the boundary layer from laminar to turbulent. Roughness starts to affect the boundary layer transition Reynolds number $Re_{x,crit}$ after the roughness Reynolds number exceeds the value $Re_k > 120$. The effect of uniform sand grain roughness to the boundary layer transition has been studied experimentally by Feindt and the results are presented in Figure 2.7. The roughness scale covered by the measurements presented in Figure 2.7 is limited, but they still give a clear indication that the surface roughness enhances the boundary layer transition. [22]

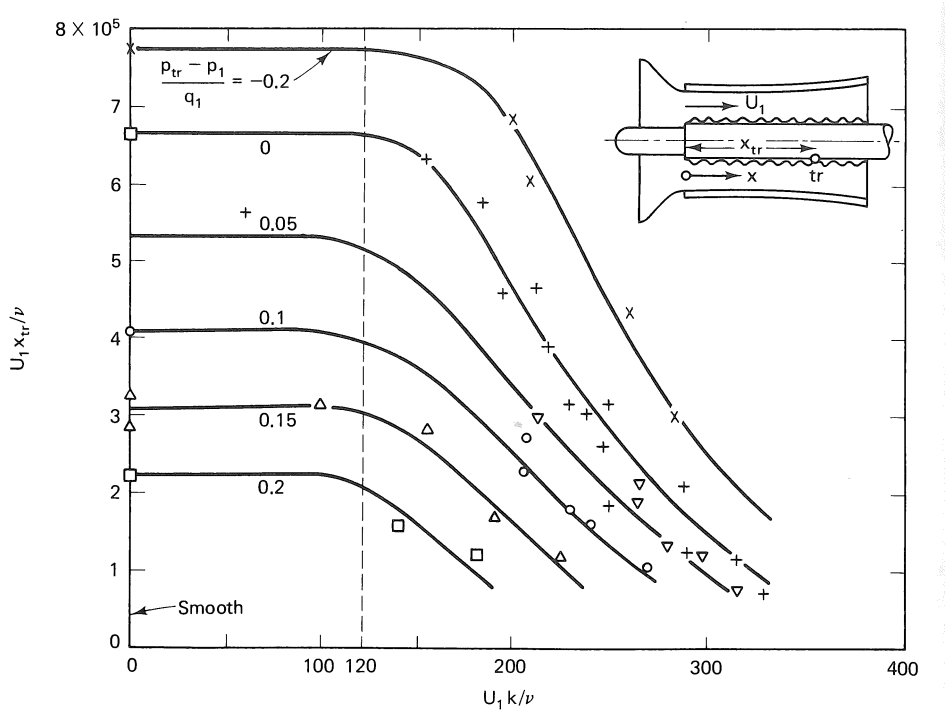

Figure 2.7: *Effect of uniform sand grain roughness and pressure gradient on boundary layer transition [22].*

The turbulence intensity of the outer flow has a significant effect on the transition. The often used value $Re_{x,crit} = 5 \times 10^5$ is applicable only if the outer flow is turbulence free and this is not the case inside a turbo-machine. In fact, the outer flow turbulence intensity in a pump is hard to predict or measure. The turbulence intensity is defined

by equation (2.53), where u' is the root mean square of the fluctuating velocity components. [9, 22]

$$I_{Tu} = \frac{u^{'}}{\bar{u}} \tag{2.53}$$

The turbulence intensity of the incoming flow in the inlet pipe can be used as an estimate for the outer flow turbulence intensity in the impeller channel. One estimate for the pipe flow turbulence intensity I_{Tu} is presented by equation (2.54), where Re_D is the pipe flow Reynolds number in the inlet pipe. [4]

$$I_{Tu} = 0{,}16\,(Re_D)^{-1/8} \tag{2.54}$$

Correlations for the critical Reynolds number of a turbulent flat plate flow as a function of the outer flow turbulence intensity exist. One such correlation has been experimentally found by Van Driest and Blumer and is presented in equation (2.55). Equation (2.55) is implicit, but quite simple to use. Many other implicit formulas have been developed based on experiments. [22, 23]

$$\frac{1690}{Re_{x,crit}^{1/2}} = 1 + 19{,}6Re_{x,crit}^{1/2}\left(I_{Tu}^2\right) \tag{2.55}$$

The effect of the pressure gradient on the boundary layer transition has also been studied and the combined effect of pressure gradient and roughness is presented in Figure 2.7. The results show that a favorable pressure gradient, where pressure drops in the flow direction, keeps the boundary layer laminar longer and an adverse pressure gradient speeds up the transition. The adverse pressure gradient in a pump therefore enhances the boundary layer transition from laminar to turbulent. The combined effect of the surface roughness, outer flow turbulence intensity and pressure gradient on transition is hard to predict and the individual results should only be used as guidelines. [22]

In reality the impeller blade and shroud surface is not flat or straight and complex three dimensional flow patterns are present. In addition to the intensity of the outer flow turbulence also the spectrum of the turbulence has an effect on transition. In a turbo-machine all the mechanism that affect the boundary layer transition are enhancing the transition and the assumption of a totally turbulent boundary layer from the leading edge seems valid if the Reynolds number is high enough. [23, 22]

When a pump is used as a fan the assumption needs to be carefully considered since the Reynolds number is significantly smaller. This also applies to small pumps, because the flow velocities and channel lengths drop accordingly. The effect of a boundary layer transition in pumps has not been studied exclusively.

Example calculation

The transition Reynolds number for a flat plate flow for air and water is presented as an example. The inlet pipe flow velocity and the Reynolds number is calculated first using the operation conditions specified in Table 1.2. The Reynolds numbers are calculated for air and water as working fluids.

$$u = \frac{Q}{A_s} = \frac{0{,}115583\,\mathrm{m^3/s}}{\frac{\pi}{4}d_s^2} = 9{,}26967\,\mathrm{m/s}$$

$$Re_{D,a} = \frac{ud_s}{\nu_a} \simeq 74500 \qquad Re_{D,w} = \frac{ud_s}{\nu_w} \simeq 1{,}34 \times 10^6$$

A remarkable difference in the inlet pipe flow Reynolds numbers results from the difference of the kinematic viscosity. The turbulence intensity of the outer flow for air and water can be estimated using equation (2.54). According to the results, the turbulence intensity of the pipe flow drops as the Reynolds number increases.

$$I_{Tu,a} = 0{,}16\,(Re_{D,a})^{-1/8} = 0{,}039359 \qquad I_{Tu,w} = 0{,}16\,(Re_{D,w})^{-1/8} = 0{,}027424$$

Numerical solution of equation (2.55) gives the critical Reynolds number for a turbulent flat plate flow using the turbulence intensity estimates calculated for the inlet pipe flow and the results are presented in Table 2.3. The dimensionless location for the transition can be calculated from equation (2.36).

Table 2.3: *Critical Reynolds number for flow over smooth flat plate,* $L = 0{,}25\,\mathrm{m}$*,* $u_\infty = 20\,\mathrm{m/s}$*.*

Fluid	$Re_{x,crit}$	I_{Tu}	x/L
Air	48413	0,039359	0,15163
Water	93864	0,027424	0,00408

The results presented in Table 2.3 confirm that for air the laminar boundary layer region can be significant. However, these results only take into account the influence of the turbulence intensity. The effects of the pressure gradient and surface roughness would lower the critical Reynolds number even further, but their combined effect cannot be estimated using simple analysis.

The dependency of the transition point on the volumetric flow through the pump is not simple, because as the volumetric flow rate drops the Reynolds number of the inlet pipe flow also drops. This leads to a higher turbulence intensity which lowers the critical Reynolds number, but at the same time the outer flow velocity in the impeller channel drops which in turn widens the laminar region.

2.3.4 Flow separation

The separation of the boundary layer occurs when the shear stress at the wall drops to zero. This causes to the flow to separate from the wall and a circulating back flow region forms. The separation bubble greatly increases the dissipation losses and causes further flow disturbances in the outer flow because the flow area is abruptly contracted and this affects the core flow. The development of boundary layer separation is presented in Figure 2.8. [23, 30]

The separation of the boundary layer can happen if the movement of the fluid in the near-wall region slows down. This can happen for example in diffusers, where the channel area increases and flow velocity drops due to continuity which creates an adverse pressure gradient where $dp/dx > 0$. The flow in the boundary layer already has a lower kinetic energy because the flow velocity drops to zero at the wall. When the lower energy flow in the boundary layer is subjected to an adverse pressure gradient, the flow near the wall can stop and even reverse and causing flow separation. [23]

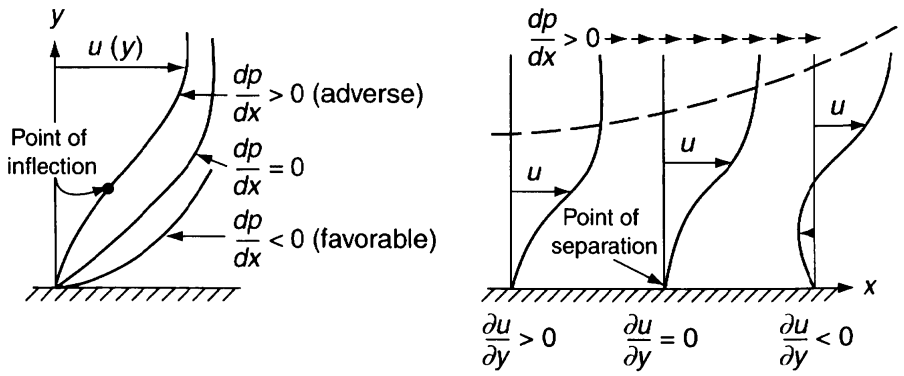

Figure 2.8: *Boundary layer separation and effect of pressure gradient [30].*

The Reynolds number of the flow has an effect on the boundary layer separation, because the turbulent fluctuations enhance the transfer of kinetic energy between the core flow and the boundary layer. The enhanced momentum transfer gives turbulent boundary layers more kinetic energy compared to laminar boundary layers and the boundary layer flow is more difficult to stop. Increasing the Reynolds number increases the momentum transfer and enables the boundary layer to keep attached longer. This is why a laminar boundary layer separates more easily than a turbulent boundary layer. [9, 23]

In an impeller channel there is an adverse pressure gradient present which enhances the flow separation. The curvature of the surfaces also enhances flow separation and the blade surfaces and channels should not have a steep curvature. The flow separation also sets the limit for a diffuser opening angle. The flow separation

happens naturally in a pump when the pump is operating at off-design conditions, because the impeller blades can only provide an attached flow in the design operating point. [9]

The tendency of the flow separation can be taken into account in an impeller blade design using CFD. The two-equation turbulence models widely used in the industry are not suitable for predicting flow separation correctly and especially if a simplified wall treatment is used. The application of CFD in the design of turbomachinery blades is justified at the design conditions where flow separation doesn't happen. Significant care should be taken to make sure that the flow is not near separation as the simple models will fail to predict this. [9, 29]

The lower Reynolds number of the flow with air compared to flow with water makes the boundary layer in fans more susceptible to flow separation. The possible flow separation with air is likely to cause dramatic decrease in the hydraulic performance. The separation of the flow is difficult to predict or measure, and the complex flow inside the pump makes the task even more difficult. It is still justified to say that the possibility of the flow separation in a pump is much obvious with air than with water.

3. IMPELLER DESIGN

In this chapter a comparative design of the pump is done using conventional design methods. The design is made on the basis of a fan. The purpose is to study possible differences in the pump design when air is used. The design follows closely the process described in the book of Gülich, but the traditional design processes in other textbooks are similar. [9, 17]

3.1 Design procedure

The main difference between a pump and a fan is the difference in the properties of the working fluid. Apart from the difference in density and viscosity, the most important difference is the lack of cavitation with air. Cavitation is boiling of water at the pump inlet side if the local pressure drops below water vapor pressure. The pressure drop can be caused by high local fluid velocity or low suction pressure. Thus, preventing cavitation is a limiting factor for the hydraulic design of a pump with water, but not with air.

Designing a pump or a fan is an iterative process due to high degree of freedom in the design of the different components. The desired operation point is usually the only known input value for the design along with the rotational speed. An iterative process results from the fact that given operation conditions can be satisfied with multiple designs. The desired pump operation characteristics outside the desired operation point can also be used to guide the design. A traditional pump design relies heavily on the use of correlations and experimental information. This enables first design phase to be made with medium effort, but the design usually needs further refinement and multiple iterations to achieve its goals.

The first phase of pump design includes the calculation of the main dimensions and impeller blade angles. The main dimensions include diameter of the inlet and outlet as well as dimensions of the casing and impeller. The impeller blade angles need to determined at the inlet and outlet edges of the impeller. In the first stage initial value for the volumetric and hydraulic efficiency and slip factor is needed and these values are calculated from correlations based on the experiments on the existing equipment. It is notable that diffuser is not directly included in the first design phase although it is an essential component of the final product. Exclusion of the diffuser is based on the assumptions of one-dimensional design theory in which

the interaction between the impeller and diffuser is not coupled. The diffuser or volute is designed separately after the impeller design is finished.

After the initial design phase, impeller blades and pump geometry are usually inserted into a CFD-program. The CFD-calculations and 3D CAD-design are common tools nowadays and can be used to further improve the design. This stage of the design process is also iterative and the results from the CFD-calculations are used to revise the design until satisfactory results have been achieved. A common practice in the CFD-calculations is to use steady state two equation turbulence models, for example the $k-\epsilon$ -model, within a rotating reference frame and exploit the rotational symmetry in order to minimize calculation time. The interaction between the impeller and diffuser is usually ignored even in this design stage. The CFD-calculation methods and design softwares are constantly evolving and available computational resources are increasing.

After the CAD-model and the CFD-calculations have been made and the design is satisfactory in theory, an initial prototype of the pump is manufactured. The model testing is a crucial step in order to validate the theoretical design, because commonly used CFD-calculation methods still can't accurately predict the performance. For example, the effect of the surface roughness cannot be modeled reliably numerically even with the best methods available. Emerging technologies in rapid prototyping can affect the modeling stage of the design process since prototyping is becoming faster and cheaper. Faster and cheaper prototyping makes it possible to try out a broader range of different design options before the design process is finished.

3.2 Main dimensions and blade angles

3.2.1 Specific speed

The goal of the design is selected to be the same as the measured pump BEP-conditions listed in Table 1.2. These conditions are $n = 2960\,\text{rpm}$, $H_{opt} = 147{,}4\,\text{m}$ and $Q_{opt} = 416{,}1\,\text{m}^3/\text{h} = 0{,}115583\,\text{m}^3/\text{s}$. The hydraulic head H_{opt} and the volumetric flow rate Q_{opt} determine the operating conditions of the pump. These input values are used to calculate the specific speed n_q which is defined by equation (3.1), where f_q is the number of impeller entries and has the value $f_q = 1$ for a normal single-entry pump [9]. The dimensions used in equation (3.1) are: $[n] = \text{rpm}$, $[H_{opt}] = \text{m}$ and $[Q_{opt}] = \text{m}^3/\text{s}$.

$$n_q = n\frac{\sqrt{Q_{opt}/f_q}}{H_{opt}^{0,75}} = 23{,}7884 \tag{3.1}$$

The definition for n_q in (3.1) is widely used in Europe and is also used in this

thesis. It should be noted that this definition is not dimensionless and n_q has the dimensions $[n_q] = \mathrm{m}^{3/4}/\mathrm{s}^{3/2}$. Further assumptions are made about the incoming flow and it's assumed that the approach flow is swirl free, which means that the incoming flow angle $\alpha_1 = 90°$. The meridional velocity c_m distribution of the approach flow is assumed to be constant. These assumptions are not strictly correct, but they are generally used and considered safe. [17, 9]

3.2.2 Hydraulic and volumetric efficiency estimates

The hydraulic and volumetric efficiency need to be evaluated prior to the actual design. It's reasonable to use statistical correlations based on existing equipment to calculate the initial efficiency values since there is no knowledge about the design yet. An estimate for the hydraulic efficiency $\eta_{h,opt}$ for a single stage radial pump is calculated with equation (3.2), where m is defined by equation (3.3). The reference volumetric flow rate is $Q_{ref} = 1\,\mathrm{m}^3/\mathrm{s}$ and an auxiliary variable a has value $a = 1$ for volumetric flow rates $Q \leq 1\,\mathrm{m}^3/\mathrm{s}$. Equation (3.2) is valid for $n_q \leq 100$ and $Q \geq 0{,}005\,\mathrm{m}^3/\mathrm{s}$. [9]

$$\eta_{h,opt} = 1 - 0{,}055 \left(\frac{Q_{ref}}{Q}\right)^{m} - 0{,}2 \left\{0{,}26 - \log_{10}\left(\frac{n_q}{25}\right)\right\}^2 \left(\frac{Q_{ref}}{Q}\right)^{0{,}1} = 0{,}909851 \quad (3.2)$$

$$m = 0{,}08a \left(\frac{Q_{ref}}{Q}\right)^{0{,}15} \left(\frac{45}{n_q}\right)^{0{,}06} = 0{,}114886 \quad (3.3)$$

Use of equations (3.2) and (3.3) with the given initial values gives an estimate for the hydraulic efficiency and the result is rounded down to $\eta_{h,opt} \simeq 0{,}9$. A more conservative value should be considered if the desired hydraulic head is not reached.

The volumetric efficiency is defined by equation (3.4), where Q_{sp} is the impeller leakage flow rate, Q_E is the leakage flow rate through an axial thrust balance device and Q_h is the leakage flow rate through auxiliaries. The impeller leakage flow rate Q_{sp} is the biggest contributor and it is assumed as an initial estimate that $Q_E = Q_h = 0$. [9]

$$\eta_v = \frac{Q}{Q + Q_{sp} + Q_E + Q_h} = 0{,}951042 \quad (3.4)$$

The volumetric efficiency is related to the flow rate with equation $Q_{La} = Q_{opt}/\eta_v$, where Q_{La} is the total flow rate through the impeller. An estimate for the leakage loss at the impeller can be calculated with equation (3.5), where exponent $m = 1{,}6$ and temporary variable $a = 4{,}1$ for $n_q \leq 27$. The variable z_H is used to estimate the effect of an axial thrust balance device and has the value $z_H = 2$ with balance holes and $z_H = 1$ otherwise [9]. An axial thrust balance device is not needed when the pump is used with gas so the latter value is used. A more precise estimate of

the leakage flow Q_{sp} can be calculated when the impeller type and clearances are known.

$$\frac{Q_{sp}}{Q_{opt}} = \frac{az_H}{n_q^m} \quad \Rightarrow \quad Q_{sp} = Q_{opt}\frac{az_H}{n_q^m} = 0{,}002975\,\mathrm{m}^3/\mathrm{s} \tag{3.5}$$

Equation (3.4) is then used to calculate the volumetric efficiency η_v. It is unclear if equation (3.5) is valid for air and therefore the calculated leakage flow is doubled to make the estimated volumetric efficiency conservative. The resulting volumetric efficiency estimate is $\eta_v \simeq 0{,}95$.

3.2.3 Shaft diameter

The pump shaft diameter d_w needs to be calculated when designing the impeller since it sets the lower limit for the inlet side inner streamline diameter d_{1i}. An illustration of the pump dimensions is presented in Figure L1.1. The design criteria for the shaft diameter is the maximum torque and consequently the maximum power $P_{a,max}$ which has to be transmitted with the shaft. The shaft power is related to the shaft torque M_a with equation (3.6), where ω is the angular velocity and $[n] =$ rpm.

$$P_a = \omega M_a = \frac{2\pi n}{60} M_a \quad \Rightarrow \quad M_a = P_a \frac{60}{2\pi n} \tag{3.6}$$

An estimate for the required maximum power $P_{a,max}$ can be calculated by using the power transferred to the fluid at the design operation point. The power transferred to the fluid is calculated with equation (3.7). The air density ρ_a value is from Table 2.1. [9, 28]

$$P_u = \rho_a g Q_{opt} H_{opt} = 196{,}715\,\mathrm{W} \tag{3.7}$$

The calculated air power is subject to all efficiency losses and the shaft power also includes mechanical losses P_m, which can be very large compared to air power if a mechanical seal is used. Therefore the maximum shaft power must be evaluated carefully and a large safety factor $Sf = 5$ is used. The maximum shaft power is estimated to be $P_{a,max} = SfP_u \simeq 1000\,\mathrm{W}$. The maximum shaft power allows the calculation of the maximum torque using equation (3.6) and the result is $M_a = 3{,}22511\,\mathrm{Nm}$.

Although some sources suggest that the pump start-up torque is between $10-25\,\%$ of the operational torque, it was observed during the measurements that the start-up torque with the unconventional use of a pump with air could be as high as three times the maximum operational torque M_a [3, 28]. Taking into account the possibility of excessively high start-up torque the final estimate for the maximum shaft torque is $M_{a,max} = 3M_a \simeq 10\,\mathrm{Nm}$.

The shaft diameter d_w is calculated using equation (3.8), where τ_{al} is the maximum allowable shear stress of the shaft material and $[\tau_{al}] =$ Pa [19, 9]. The

maximum allowable shear stress is $\tau_{al} = 213\,\text{MPa}$ for steel grade S 355 (EN 10025) [19].

$$d_w = \left(\frac{16P_{a,max}}{\pi\omega\tau_{al}}\right)^{\frac{1}{3}} = \left(\frac{16M_{a,max}}{\pi\tau_{al}}\right)^{\frac{1}{3}} = 0{,}006207\,\text{m} \tag{3.8}$$

The deflection of the shaft must also be calculated because the low torque requirements might allow the shaft diameter to become too small to resist deflection caused by the weight of the impeller and the radial thrust forces. The radial thrust is assumed to be negligible with air because the radial thrust force is proportional to the density of the fluid. [9]

The deflection of the shaft δ can be calculated with equation (3.9), where $q = F/L$ is the uniform load on the shaft of length L by force F, E is the modulus of elasticity of the shaft material and I_z is the area moment of inertia which is defined by equation (3.9) for a solid circular rod [19]. The overhung shaft length is assumed to be $L = 0{,}1\,\text{m}$ in the calculation. The modulus of elasticity of steel is $E = 200\,\text{GPa}$ [19]. The force caused by the impeller weight is calculated with $F = m_{La}g$, where the maximum impeller weight is estimated to be $m_{La} = 20\,\text{kg}$.

$$\delta = \frac{qL^4}{8EI_z} \tag{3.9}$$

$$I_z = \frac{\pi}{64}d_w^4 \tag{3.10}$$

A minimum value for the shaft diameter can be calculated by defining a maximum allowable shaft deflection $\delta_{max} = 50\,\mu\text{m}$ and combining equations (3.9) and (3.10) which leads to equation (3.11). Equation (3.11) defines another condition for minimum shaft diameter in addition to equation (3.8) and the larger diameter is used.

$$d_w = \left(\frac{64qL^4}{8\pi\delta_{max}E}\right)^{\frac{1}{4}} = 0{,}014951\,\text{m} \tag{3.11}$$

With air the shaft diameter is determined by deflection requirements instead of torque and based on equation (3.11) the shaft diameter of $d_w = 0{,}015\,\text{m}$ is selected. An estimate for the radial thrust force should be calculated after the impeller has been designed. If the radial thrust is significant compared to the impeller weight, the shaft diameter should be increased accordingly by adding the radial thrust force to F.

3.2.4 Impeller outer diameter

The impeller outer diameter d_2 is the second impeller parameter which needs to be determined. Determination of the main dimensions of the pump can be done in several ways and the method described here is not the only possibility. One way to

determine the impeller outer diameter is to select the desired head coefficient ψ_{opt} at the operation point. The head coefficient is defined by equation (3.12), where u_2 is the peripheral speed at the impeller outer diameter.

$$\psi = \frac{2gH}{u_2^2} \tag{3.12}$$

The value of head coefficient affects the shape of the $Q - H$-curve and selecting a high head coefficient leads to a flatter curve and might affect the stability of the $Q - H$-curve. The benefit of selecting a high head coefficient is the smaller impeller outlet diameter d_2 whereas the selection of a lower value results in a larger diameter. A lower head coefficient value leads to steeper and more stable $Q - H$-curve at the expense of growing material costs as the pump size increases. The desired value of the head coefficient is somewhere between the upper and lower limit and an experimental formula for the optimal head coefficient as a function of the specific speed is presented in equation (3.13), where the reference specific speed is $n_{q,ref} = 100$. [9]

$$\psi_{opt} = 1{,}21 \exp\left(-0{,}77 n_q / n_{q,ref}\right) = 1{,}00748 \tag{3.13}$$

Gülich also suggests that the head coefficient should be higher for pumps with low specific speeds (below $n_q = 20 - 25$) because of the high dependency of the disk friction losses on the impeller diameter. Selecting the higher head coefficient lowers the impeller outer diameter and thus lowers the disk friction losses [9]. The calculated value is therefore rounded up and the head coefficient at the operation point is selected to be $\psi_{opt} = 1{,}05$.

After the head coefficient has been determined, the impeller outlet diameter d_2 is calculated using equation (3.14). The result is rounded and the selected impeller outlet diameter is $d_2 = 0{,}34\,\mathrm{m}$.

$$d_2 = \frac{60}{\pi n}\sqrt{\frac{2gH_{opt}}{\psi_{opt}}} = 0{,}338621\,\mathrm{m} \tag{3.14}$$

3.2.5 Impeller blade number

The impeller blade number z_{La} has to be selected without knowing the details of the impeller design. The selection of the impeller blade number z_{La} is essentially an optimization problem. If the blade number is too small, an uneven velocity distribution and even flow separation will form at the impeller outlet because the fluid flow doesn't follow the streamlines in the impeller channel. A too small blade number leads to increased turbulence dissipation losses and pressure pulsation. [9, 17]

Selecting the impeller blade number too high will in turn increase the friction losses since the skin friction losses increase along with the impeller area. The impeller blade flow blockage also increases and a high blade number can lead to $Q-H$-curve instability. The pressure pulsation is lower and velocity distribution at the impeller outlet is better with a higher blade number. The designer must carefully consider what is the best value of the blade number for the design.[17, 9].

The selection of impeller blade number can be checked against blade loading after the impeller design is finished. The blade loading is defined by calculating the pressure difference over the blade along the blade curvature. The blade loading curves should be smooth and the loading level should be within the recommended range. If the calculated blade loading is too high, the impeller blade number must be increased and vise versa. [9, 20]

An initial guess has to be made based on experience because no reliable way to estimate the required blade number a priori exists. Gülich suggest avoiding an impeller blade number $z_{La} < 5$ for pumps with static heads $H_{st} > 100\,\mathrm{m}$ since the pressure pulsation can be too high. Most of existing centrifugal pumps with specific speed between 10 and 120 have an impeller blade number in the range of $5 < z_{La} < 7$. [9]

The selected impeller blade number is $z_{La} = 7$. The selecting of high blade number is not based on the definition of blade loading, since the pressure difference is proportional to density and blade loading will likely be low with air. The selection is rather based on the boundary layer analysis which shows that air flow is more likely to deflect and separate compared to the water flow. All the recommendations in pump design are based on the conventional usage and the selection of a higher impeller blade number tries to take the unconventional usage of a pump with air into account.

3.2.6 Impeller inlet diameter

The design criteria for the impeller inlet diameter d_1 are usually related to cavitation properties or suction capability of the pump. This is a fundamental difference between the design for water usage compared to air usage. One possible criterion to determine the impeller inlet diameter is to minimize the relative velocity w_1 at the impeller inlet. The minimum value of the relative velocity can be calculated by differentiating the relative velocity w_1 with respect to the impeller inlet diameter d_1. The differentiation leads to equation (3.15), where d_1^* is the dimensionless impeller inlet diameter. f_{d_1} is the correction factor which takes into account secondary effects such as the blade blockage and uneven velocity distribution, d_n^* is the dimensionless impeller hub diameter and δ_r is a parameter that takes into account the inflow swirl

and is defined by equation (3.16). [9]

$$d_1^* = f_{d_1}\sqrt{(d_n^*)^2 + 1{,}48 \times 10^{-3}\frac{n_q^{1{,}33}}{(\eta_v \delta_r)^{0{,}67}}} = 0{,}368262 \tag{3.15}$$

$$\delta_r = 1 - \frac{c_{1m}}{u_{1m}\tan(\alpha_1)} \tag{3.16}$$

The secondary loss correction factor f_{d_1} takes values between 1,15 and 1,05 falling from $n_q = 15$ to 40 for normal impellers. A linear interpolation yields the value $f_{d_1} \simeq 1{,}125$ for the specific speed $n_q \simeq 24$ [9]. The inflow swirl parameter has the value $\delta_r = 1$, because it is assumed that the inflow is swirl free which means that the inlet approach flow angle is $\alpha_1 = 90°$. The impeller hub diameter $d_n \geq d_w$ is estimated to be $d_n = 1{,}3 d_w \simeq 0{,}02\,\mathrm{m} \;\Rightarrow\; d_n^* = 0{,}058824$ to allow a problem free shaft installation. An estimate for the dimensionless impeller inlet diameter is calculated from equation (3.15) and the result is $d_1^* = 0{,}368262 \;\Rightarrow\; d_1 \simeq 0{,}125\,\mathrm{m}$.

3.2.7 Blade inlet diameter at the inner streamline

The minimum blade inlet diameter at the inner streamline d_{1i} is limited by the shaft mounting and the hub diameter d_n so that $d_{1i} \geq d_n$. For radial impeller geometries with $n_q < 25 \ldots 30$ it is advisable to select a value as small as possible for d_{1i} to improve the $Q - H$-curve stability [9]. The blade inlet diameter at the inner streamline directly affects the impeller blade inlet angle $\beta_{1B,i}$ at the inlet and the angle approaches 90° as the diameter approaches zero. Therefore the blade inlet diameter at the inner streamline has to be selected large enough to avoid excessively large impeller blade angles at the inner streamline. Large impeller blade angles at the inlet can cause flow separation and cavitation especially when operating at off-design conditions. [9, 17]

There is no direct selection method for the diameter d_{1i} and based on the recommendations and guidelines presented above the blade inlet diameter at the inner streamline is selected to be $d_{1i} = 0{,}05\,\mathrm{m}$. The selected diameter has to be revised if the resulting impeller blade inlet angle at the inner streamline is too large.

3.2.8 Impeller inlet blade blockage, blade thickness and edge profiling

The blade blockage factor τ_1 is used to take the impeller blade blockage into account as the finite impeller blade thickness reduces the available flow inlet area at the impeller inlet. The inlet flow velocity c_{1m} at the impeller inlet has to increase to a higher value $c_{1m}^{'}$ when the flow area decreases to fulfill the continuity. This increase in the inlet meridional velocity has to be taken into account since it changes the

inlet velocity triangle. The blade blockage factor τ_1 is defined by equation (3.17), where λ_{La} is the inlet blade inclination angle and e_1 is the blade tip thickness at the inlet.

$$\tau_1 = \left\{ 1 - \frac{z_{La} e_1}{\pi d_1 \sin(\beta_{1B}) \sin(\lambda_{La})} \right\}^{-1} \tag{3.17}$$

The blade inclination angle λ_{La} defines the attachment angle between the impeller shroud surface and the blade and it is used with twisted blades. With the current design it is assumed that $\lambda_{La} = 90°$.

The impeller blade thickness e is determined by the requirements of the manufacturing process and mechanical strength. Experimental selection method suggests that the blade thickness requirements are fulfilled when the relation e/d_2 is selected between 0,016 and 0,022. This yields a minimum blade thickness of $e \simeq 0{,}0054\,\text{m}$ with the selected impeller outlet diameter $d_2 = 0{,}34\,\text{m}$. Pump impellers are usually manufactured by casting and the casting process requires a minimum blade thickness between 3 and 5 mm [3, 9]. The blade loading from pressure is minimal when pump is used with air and therefore a blade thickness of $e = 0{,}003\,\text{m}$ is selected. The selection is backed up by the fact that fan impellers are commonly made by welding using sheet metal. A more thorough investigation including FEM-calculations should be conducted to determine the minimum required impeller blade thickness for fan usage.

In addition to the blade thickness, the blade leading edge profile needs to be decided. Typical approach with pumps is to profile the leading edge with an elliptic profile or a wedge-like profile. With fans it is common to leave the leading edge unprofiled to cut costs. Profiling is used in order to improve the pressure distribution at the blade inlet and to avoid excess local velocities and discontinuities thus also improving the cavitation characteristics. [9, 17]

A simple elliptic profiling can be achieved by minimizing the blade leading edge profile pressure loss. A favorable profile is generated when the relation of the elliptic blade tip length L_p to the blade thickness is $e/L_p = 0{,}2$ [9]. The blade leading edge rounding is estimated to be $e_1 = 0{,}001\,\text{m}$ and following the guidelines the resulting elliptic profile length is $L_p = 0{,}015\,\text{m}$. The blade trailing edge profiling is not done in order to simplify the design and because the selected blade thickness is already small.

3.2.9 Impeller blade inlet angles

Prior to calculating the impeller blade inlet angles β_{1B}, the incidence angle i_1 and the meridional velocity c_{1m} are needed. The incidence angle is defined as the angle between the flow angle with blade blockage β_1' and the impeller blade angle β_{1B} and the flow angle β_1' is determined from incoming flow rate. It is a common practice to

use an incidence angle even at the design point in order to improve the off-design operation of the pump. [9, 17]

The incidence angle is added to the flow angle with blockage $\beta_i^{'}$ according to $\beta_{1B} = \beta_1^{'} + i_1$. The incidence angle is usually selected between 0° and 4°. Using a positive incidence angle shifts the shockless ($\beta_{1B} = \beta_1^{'}$) entry point flow rate slightly above the design best efficiency point. The selected incidence angle for the design is $i_1 = 2°$. [9]

The meridional velocity component at the impeller inlet c_{1m} is calculated using equation (2.9), where A_1 is the flow area at the impeller inlet. The meridional velocity component is calculated without blockage as it is taken into account by τ_1.

$$c_{1m} = \frac{Q_{La}}{A_1} = \frac{Q_{La}}{\frac{\pi}{4}\left(d_1^2 - d_n^2\right)} = 9{,}66603\,\mathrm{m/s}$$

The impeller blade inlet angles can be calculated using equation (3.18), where the inlet blade blockage τ_1 is defined by equation (3.17). The calculation procedure is implicit because the impeller blade inlet angle β_{1B} is also included in τ_1. The inlet flow is assumed to be perpendicular to the impeller inlet and therefore $c_{1u} = 0$.

$$\beta_{1B} = \beta_1^{'} + i_1 = \arctan\left(\frac{c_{1m}\tau_1}{u_1 - c_{1u}}\right) + i_1 \tag{3.18}$$

The blade inlet angle is calculated at the inner, mean and outer streamlines denoted by the diameters d_{1i}, d_{1m} and d_{1a} respectively. The mean streamline diameter is calculated with equation (3.19). It is also assumed that the outer streamline diameter of the impeller blade inlet is the same as the inlet diameter so that $d_{1a} = d_1$.

$$d_{1m} = \sqrt{0{,}5\left(d_{1a}^2 + d_{1i}^2\right)} \simeq 0{,}095\,\mathrm{m} \tag{3.19}$$

The streamline diameters are used to calculate the peripheral velocities at the inlet with equation (2.8) and the results are $u_{1i} = 7{,}7493\,\mathrm{m/s}$, $u_{1m} = 14{,}7236\,\mathrm{m/s}$ and $u_{1a} = 19{,}3732\,\mathrm{m/s}$. The change in the peripheral velocity at the impeller inlet is the reason why the impeller blade inlet angle is not constant and the blade design is three dimensional. The impeller inlet blade angles are calculated using equation (3.18) with the following results:

$$\beta_{1B,i} = 53{,}9° \quad \beta_{1B,m} = 36{,}1° \quad \beta_{1B,a} = 29{,}4°$$

The impeller inlet angle at the inner streamline is quite high, but because cavitation is a limiting factor the higher angle is accepted. If CFD-calculations would show that flow separation occurs near the hub, then the inner streamline diameter d_{1i} should be inceased in order to reduce the angle $\beta_{1B,i}$.

3.2.10 Impeller inlet and outlet width

The impeller width at inlet can be calculated from equation (2.9) by using the definition $d_{1b} = 0{,}5\,(d_1 + d_{1i}) = 0{,}0875\,\mathrm{m}$. The result for the impeller width at the inlet is:

$$c_{1m} = \frac{Q_{La}}{A_1} = \frac{Q_{La}}{\pi d_{1b} b_1} \quad \Rightarrow \quad b_1 = \frac{Q_{La}}{\pi d_{1b} c_{1m}} \simeq 0{,}0435\,\mathrm{m} \tag{3.20}$$

The determination of the impeller outlet width is more difficult because the blade number, the impeller outlet width b_2 and the impeller blade outlet angle β_{2B} are all connected and selection of one influences the other. The blade number is the only parameter which has already been selected. If the impeller outlet width is large, the resulting meridional velocity component c_{2m} is small and this increases the peripheral component c_{2u} by definition of the velocity triangles if the flow stays blade congruent. [9]

The $Q - H$-curve flattens with increasing b_2 and the flow recirculation at the impeller outlet grows as b_2/d_2 grows. This stability requirements of the $Q - H$-curve and growth of flow non-uniformity set the limits for the impeller outlet width together with the obvious condition $b_2 < b_1$. Gülich presents an empirical correlation for the dimensionless impeller outlet width b_2^* and this is presented in equation (3.21), where $n_{q,ref} = 100$. [9]

$$b_2^* = 0.017 + 0.262\frac{n_q}{n_{q,ref}} - 0{,}08\left(\frac{n_q}{n_{q,ref}}\right)^2 + 0.0093\left(\frac{n_q}{n_{q,ref}}\right)^3 = 0{,}074924 \tag{3.21}$$

The dimensionless result is converted and the result for the impeller outlet width is $b_2 \simeq 0{,}025\,\mathrm{m}$. This result is based on experimental data and it used in the further calculations. The connection between b_2, β_{2B} and z_{La} creates the need for initial guessing during the design and empirical correlations are useful in the sense that they make the initial guesses more correct and thus reduce the total time required for the design.

3.2.11 Impeller blade outlet angles

The impeller blade angle at the outlet must be selected to produce the required head with the selected values of d_2, b_2 and z_{La}. This design stage should really be iterative in terms of selecting b_2, β_{2B} and z_{La} to get the best results for the individual design. This design only involves the calculation of the initial impeller blade outlet angle based on the prior selections. A constant impeller outlet angle can be used for pumps with $n_q < 40$ and the designed device falls into this category. [9, 17]

An important parameter called the slip factor γ is introduced to take the non-uniformity of the velocity profile at the impeller outlet into account. The non-

uniform velocity profile is created because the flow doesn't stay blade congruent especially in the outer triangle of the impeller channel, where the impeller channel walls (blades) end at different points considering the relative flow with velocity w. The slip phenomenon is presented in Figure 3.1. The slip factor is related to the peripheral velocities with equation (3.22), where $c_{2u\infty}$ denotes the blade congruent flow velocity component. [9, 17]

$$c_{2u\infty} - c_{2u} = (1 - \gamma)\, u_2 \tag{3.22}$$

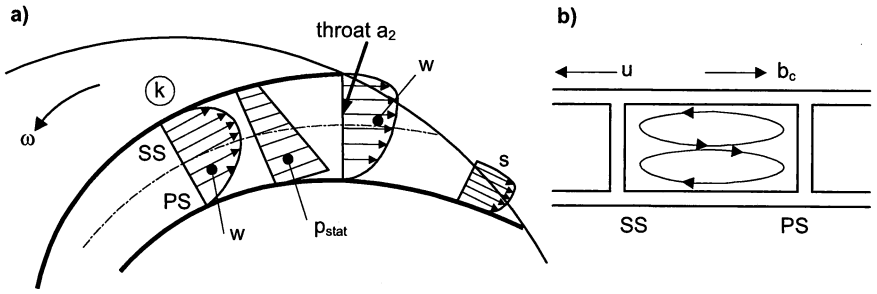

Figure 3.1: *Non-uniform velocity distribution at impeller outlet a) flow between the blades b) secondary flows [9].*

The calculation of the slip factor has been subjected to intensive research because of its importance in the design process. The slip phenomenon is hard to predict correctly by using the one-dimensional approach, because the secondary three dimensional flows have large effects on the flow distribution. The slip factor has to be somehow estimated during the initial design. In this thesis the slip factor γ is calculated following the procedure proposed by Gülich, but many other methods have been developed. [9, 14, 17]

The slip factor is related to the impeller blade outlet angle and the calculation of the slip factor and the impeller outlet angle β_{2B} is again implicit. The slip factor is defined by equation (3.23) for radial impellers, where k_w is defined by equation (3.24) and ϵ_{lim} by equation (3.25). The dimensionless velocity at the mean streamline is calculated with $d^*_{1m} = d_{1m}/d_2 = 0{,}279412$.

$$\gamma = 0{,}98 \left(1 - \frac{\sqrt{\sin(\beta_{2B})}}{z_{La}^{0,7}}\right) k_w \tag{3.23}$$

$$k_w = 1 - \left(\frac{d^*_{1m} - \epsilon_{lim}}{1 - \epsilon_{lim}}\right)^3 \tag{3.24}$$

$$\epsilon_{lim} = \exp\left(-\frac{8{,}16 \sin(\beta_{2B})}{z_{La}}\right) \tag{3.25}$$

The equation system can be simplified by instering the value $k_w = 1$ if the condition $d^*_{1m} < \epsilon_{lim}$ is satisfied. An initial guess with $\beta_{2B} = 25°$ is made and the resulting value $\epsilon_{lim} = 0{,}611004$ fulfills the condition.. The hydraulic head is calculated with equation (3.26), where τ_2 is the blade blockage factor at the impeller outlet and is calculated with equation (3.27). [9]

$$H_{opt} = \frac{\eta_h u_2^2}{g}\left(\gamma - \frac{Q_{La}}{A_2 u_2 \tan(\beta_{2B})}\tau_2\right) \tag{3.26}$$

$$\tau_2 = \left\{1 - \frac{z_{La} e}{\pi d_2 \sin(\beta_{2B})}\right\}^{-1} \tag{3.27}$$

The flow area at the impeller outlet is calculated with $A_2 = \pi d_2 b_2$. The impeller outlet blade angle β_{2B} can be solved iteratively from equations (3.23), (3.26) and (3.27) and the resulting impeller blade outlet angle is $\beta_{2B} = 18{,}6°$, which also fulfills the simplification condition. Using the solved value of β_{2B} the slip factor can be calculated using equation (3.23) and the result is $\gamma \simeq 0{,}838$. The next design step would be the design of the impeller blades once the impeller blade angle at the outlet has been solved.

3.2.12 Results of the main dimensions and blade angle calculations

The results from the previous calculations are collected in Tables 3.1 and 3.2. The main dimensions of the new design are remarkably similar to the known values of the measured device which are presented in Table 1.1. The only measurable difference is the slightly larger outer diameter d_2 in addition to the differences in impeller widths b_1 and b_2, which are slightly larger in the measured device. The impeller blade angles of the current design at the inlet are probably larger compared to the existing device, because the impeller inlet diameter at the inner streamline is smaller resulting in a higher blade angle β_{1B}. The blade angles or dimensions of the pump impeller were not provided by Sulzer and therefore further comparison is not possible.

Table 3.1: *Main dimensions of designed pump.*

Property	Value
$d_1 = d_{1a}$	0,125 m
d_2	0,34 m
d_n	0,02 m
d_w	0,015 m
d_{1i}	0,05 m
d_{1m}	0,095 m
b_1	0,0435 m
b_2	0,025 m
e	0,003 m

Table 3.2: *Impeller blade angles of designed pump.*

Property	Value
z_{La}	7
γ	0,838
$\beta_{1B,i}$	53,9°
$\beta_{1B,m}$	36,3°
$\beta_{1B,a}$	29,4°
β_{2B}	18,6°

The next step would be the design of the impeller blades and the meridional section of the pump. The design of the impeller blades is out of scope of this thesis and is not made. The CFD-calculation is also not done as the final design of the pump impeller was not the purpose of this thesis. The design of the volute or diffuser is omitted, because the design of a single spiral volute is not dependent on the fluid properties. [9, 17]

The main results from the comparative impeller design are that the fluid properties don't have a significant effect on the main pump dimensions. The exclusion of cavitation enables the use of larger impeller blade angles at the inlet, but otherwise the blade angles are unaffected. The greatest differences are to be expected in the design of the impeller blade profiles, because of the difference in the separation tendency between air and water flow.

4. MEASUREMENT SYSTEM

In this chapter the measurement system is presented. The design of the measurement system is strictly based on standard ISO5801:2007 [12]. The measurement system configuration and components including the sensors are presented. The measurement method including the measurement software and process to determine friction losses are described.

4.1 System design

4.1.1 Design principles

The design of the measurement system had to be done because the laboratory of Energy Technology didn't have an existing measurement system for fans. The natural reference for the measurement system design is the international standard for fan measurements ISO 5801:2007. The designed system complies with the standard as perfectly as possible. The principal design goals for the measurement system are:

- The measurement system provides reliable and accurate results to measure the pump performance with air.
- The measurement system is easy to use and re-usable for measuring other fans in the same size range.
- The existing equipment in the laboratory is used as much as possible to keep the cost reasonable.

The goals listed above guide the design process and determine the limits for the system. Accurate enough means that the measurement system is able to detect changes between different pump and impeller designs, but accuracy does not necessary comply with the standard. The main purpose is to see the differences between the designs and not to perform industrial verification quality standardized measurements. Industrial quality measurements would have required significantly larger financial investment into the measurement system than is possible with the available resources.

The standardized measurement system is a good basis for future measurement needs. The torque transducer operation range limits the input power of the fan and

the inlet and outlet pipe diameters limit the possible coupling sizes, but otherwise any fan or pump can be measured. The flow rate measurement with an orifice plate can be adjusted to higher or lower flow rates by altering the size of the orifice as long as the restrictions specified in [11] are fulfilled. The measurement system is best suited for fans with the same inlet and outlet pipe diameters D_3 and D_4, but it can also be used with other coupling diameters with adapters. Use of adapters can be a deviation from the standard if the difference in the pipe diameter is large [12]. The length of the inlet pipe and the flow resistance of the orifice plate and flow conditioners set the lower measurable head limit of the system and very low pressure fans might not be able to overcome the pressure losses. The upper head limit is more versatile as it only depends on the the range of the pressure sensor in the outlet pipe.

The software MATLAB is chosen because it's easy to use and has all the necessary components already in place, which include a GUI design tool, hardware interfaces, robust numerics and data processing capabilities. MATLAB is platform independent and provides an in-built serial reader for the existing data logger. MATLAB code is simple and easy to read and thus a good choice for further development. After initial measurements it was clear that a graphical user interface would greatly simplify and speed up the measurements. The measurement system software consists of a GUI and functions coded purely in MATLAB. The code is completely written in-house and by the author.

The standard specifies four different possible fan coupling setups for the measurements. More than one possible setup is needed because fan installations can differ depending on the application. For instance axial fans in air conditioning units operate in different conditions than large radial primary air supply fans in power stations. The different measurement setups provided by the standard directly reflect the different installations in real operation conditions. Installation category D of the standard covers the installation type of the measured pump and is selected for the measurement system. [12]

4.2 Measurement system configuration

Installation configuration D of the standard ISO 5801:2007 specifies a measurement system where the inlet of the fan has a common inlet section and outlet has a common outlet section. This means that the inlet and outlet are connected to pipes. Flow contraction by a throttle valve can either be in the inlet or in the outlet section and the same goes for the flow rate measurement. It is chosen that the flow rate measurement is in the inlet section and the throttle valve is in the outlet section of the system. The selected material for piping and flanges is acrylic. Plastic material is chosen because it is much cheaper and lighter than metal and friction

losses are smaller.

The inlet for a centrifugal pump is horizontal and it's easier to fit a long horizontal pipe to the inlet rather than a long vertical pipe to the outlet. The section where the flow rate measurement device is located is always longer because of the strict requirements for minimum pipe lengths before and after the flow rate measurement. Keeping the throttle valve in the pressure side could also improve stability of the flow.

For the flow rate measurement there are three allowed measurement methods in the standard: determination by conical or bellmouth inlet, Pitot-static tube traverse and orifice plate. The orifice plate is chosen for its accuracy and simplicity and because it fits well in the ducted configuration. The measurement of flow rate with an orifice plate has its own measurement standard ISO 5167-2:2003.

The main parts for the system are designed according to the standard ISO 5801:2007 and designed the CAD-software SolidWorks. The standard specifies almost all dimensions as a function of the pipe inside diameter because it's an universal way to design measurements systems of different sizes. The dimension units in the attached CAD-drawings are in [mm]. The design of each individual part is presented. The main parts of the measurement system are:

- inlet pipe (including an AMCA cell type flow straightener and a Zanker flow conditioner plate)
- flow rate measurement with an orifice plate
- outlet pipe (including a star type flow straightener)
- throttle valve
- torque transducer on the shaft between the electrical motor and the pump
- pressure and temperature sensors, electrical wiring and a data logger connected to a computer.

A picture of the finished and installed core part of the measurement system is shown in Figure 4.1. The picture also shows the pump and electrical drive with the torque transducer on the shaft. The shaft cover is not in place for keeping torque transducer installation visible. All the pressure sensors are attached to the wooden panel along with the seal cooling liquid flow control valve. Temperature sensors for temperature difference based efficiency measurement can be seen just upstream of the inlet and downstream of the outlet of the pump. The orifice plate is briefly visible in the lower right corner of Figure 4.1. The throttle valve on top of the outlet pipe, the first half of the inlet pipe and the ambient air condition measurements are missing from the

picture. Schematics of the measurement system with sensor locations is presented in Appendix 3.

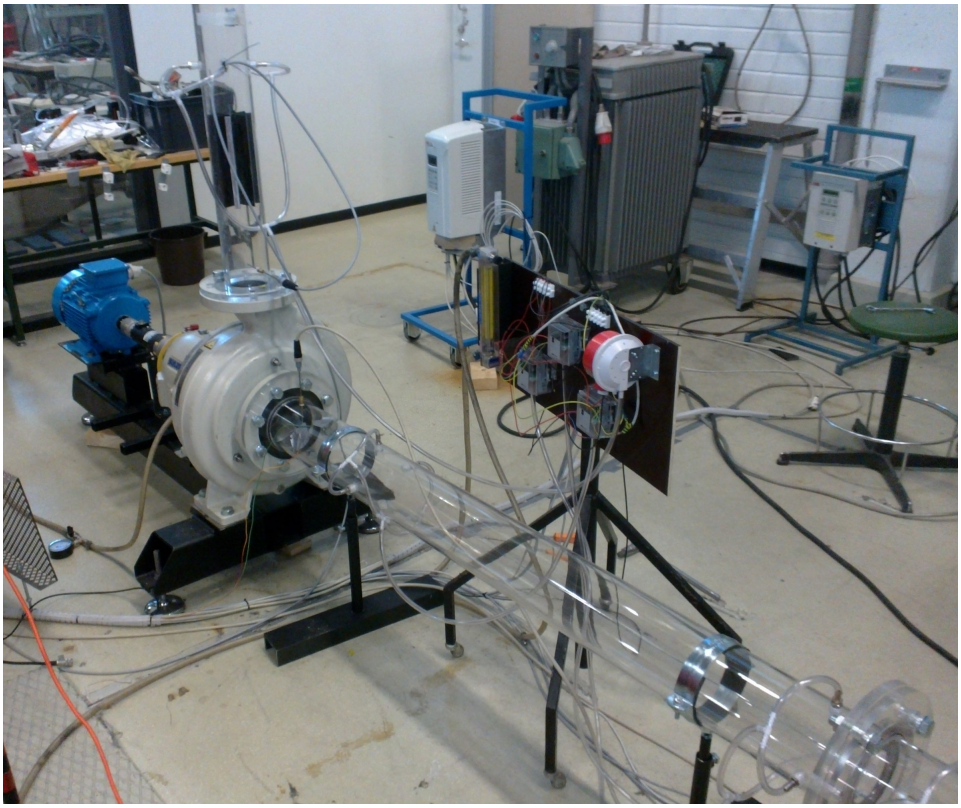

Figure 4.1: *Picture of assembled measurement system.*

4.2.1 Inlet pipe

The inlet pipe consists of three parts and the pipe is acrylic with inner diameter $D_4 = 126\,\text{mm}$ and a wall thickness of 5 mm. The parts are connected to each other with flanges which are bolted together. The flanges have a rubber seal ring to prevent leakage and the connection to the pump inlet has a seal ring. Total length of the inlet pipe is 5 m and the length of the individual parts is (starting from the intake): 2 m, 1,5 m and 1,5 m. The dimensional drawings of the input pipe parts and flanges can be found in Appendix 2. An assembly drawing of the inlet pipe is shown in Figure 4.2.

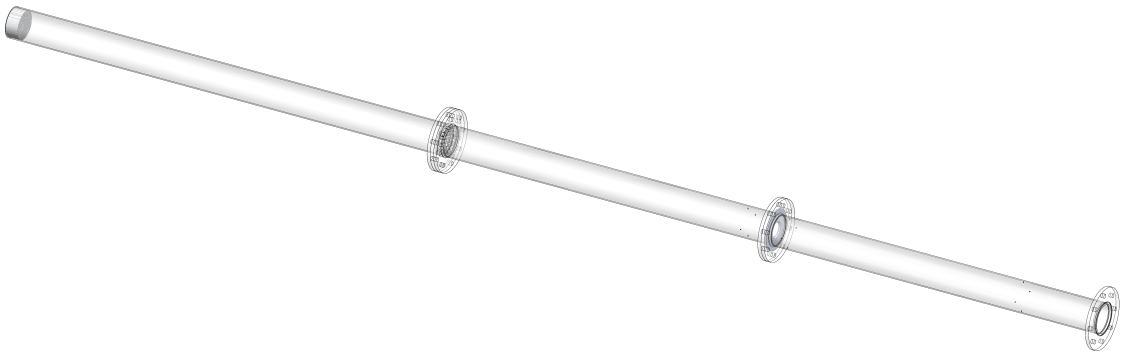

Figure 4.2: *Inlet pipe assembly.*

The first part includes an AMCA cell type flow straightener at the intake to prevent pre-swirl of the flow entering the pipe. A detailed view of the AMCA is shown below in Figure 4.3 and a dimensional drawing of the part is in Appendix 2. An existing AMCA cell with matching dimensions was used and cut to specified length and diameter.

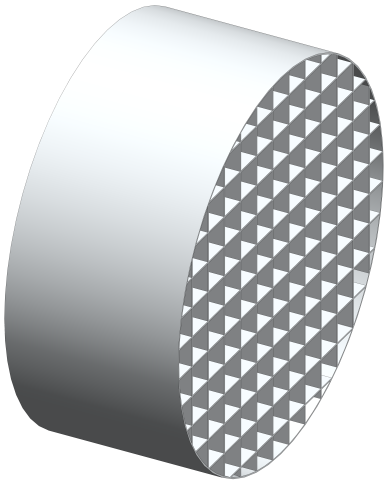

Figure 4.3: *AMCA cell type flow straightener.*

Between the first and second part there is a Zanker flow conditioner plate which is required upstream of an orifice plate. The purpose of the Zanker plate is to enhance the evenness of the flow velocity profile before the orifice plate flow rate measurement. An illustration of the Zanker flow conditioner plate is presented in Figure 4.4 and a detailed dimensional drawing is in Appendix 2. The outer holes in Figure 4.4 are for connecting the plate between flanges and the holes clustered in the center are for equalizing the flow velocity profile.

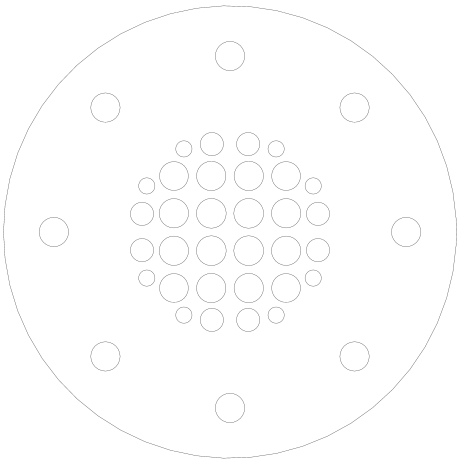

Figure 4.4: *Zanker flow conditioner plate.*

4.2.2 Flow rate measurement

Between the second and the third part there is the orifice plate for measuring the flow rate. The second and third part of the inlet pipe have pressure measurement taps upstream and downstream of the orifice plate and the third part has taps upstream of the pump. A special flange with a countersink is used to fit the orifice plate precisely. A dimensional drawing of the special flange is presented in Appendix 2.

The orifice plate measurement uses the so called D and $D/2$ pressure taps, which means that the upstream pressure measurement plane is located at the distance D upstream of the orifice plate and the downstream pressure measurement plane is located at the distance $D/2$ downstream of the plate. The pressure tap distances are measured from the upstream face of the orifice plate [11, 12]. A detailed drawing of the orifice plate configuration and pressure tap locations can be found in Appendix 2 and an illustration of the orifice plate is presented in Figure 4.5.

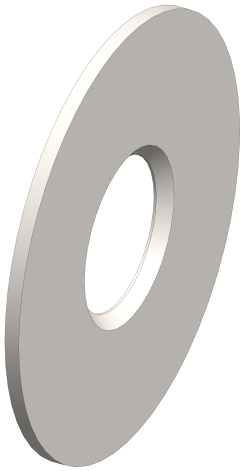

Figure 4.5: *Illustration of the orifice plate.*

The original design of the system had an orifice plate with the orifice diameter $d = 63\,\text{mm}$ but it turned out to be too small and the design was revised so that the orifice size used in the measurements is $d = 81{,}9\,\text{mm}$. The orifice plate flow measurement is the largest source of the inlet pipe pressure loss and the amount of the pressure loss is related to the size of the orifice [11]. The pressure loss of the inlet pipe determines the maximum attainable flow rate of the measurement system and thus sets the upper limit for the flow rate measurement scale. The ratio of the orifice diameter to pipe diameter $\beta = d/D$ has to be in the range $0{,}2 \leq \beta \leq 0{,}75$ and $p_{do}/p_u > 0{,}75$. [12]

A larger orifice results in a wider flow rate measurement range but with a decrease in measurement accuracy of the low flow rate at the end of the measurement range, because the pressure difference Δp drops and the relative measurement error increases. Optimal measurement accuracy would require several differently sized orifice plates to be used for different flow rate ranges. In the thesis only the orifice plate with the orifice diameter of $d = 81{,}9\,\text{mm}$ is used for all flow rates.

The third part which connects to the pump inlet includes the pressure measurement taps upstream of the pump. Standard ISO 5167-2:2003 specifies that there should be at least $7D$ pipe length after the orifice plate to recover the full velocity profile after the contraction in the orifice [11]. Pressure is always higher just upstream of the pump which means that the velocity in the pipe has reduced after the orifice part of the pressure is recovered. The contraction generates a high net pressure loss in the orifice plate pressure measurement. The location of the upstream pressure measurement plane from the pump inlet plane is $3D$. A detailed drawing can be found in Appendix 2 and the location of pressure measurements is presented in Appendix 3.

4.2.3 Outlet pipe and throttle valve

The outlet pipe is vertical and connected to the pump outlet flange. An illustration of the outlet pipe configuration is shown in Figure 4.6. The flow restriction valve is not shown in Figure 4.6. A detailed dimensional drawing is in Appendix 2.

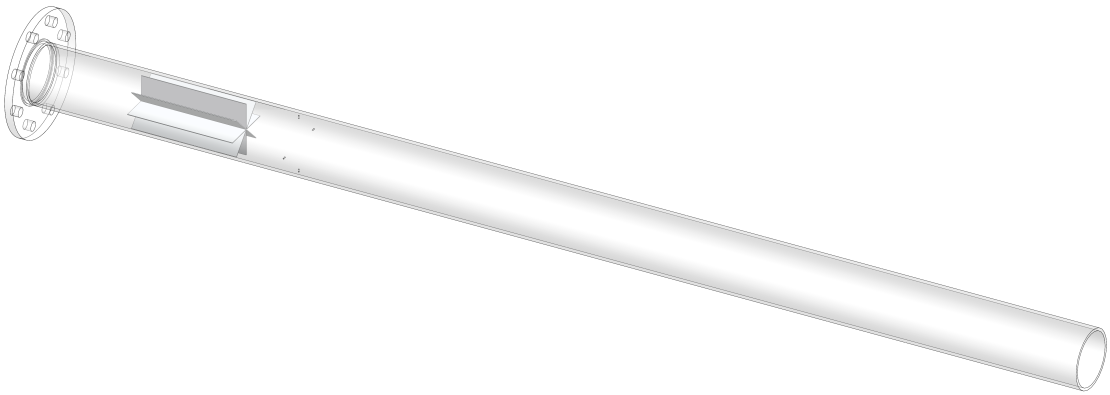

Figure 4.6: *Drawing of the outlet pipe assembly.*

The outlet pipe has a star type flow straightener upstream of the outlet pressure measurement plane to diminish the possible swirl of the outflow. A flow straightener is always required before the outflow pressure measurement [12]. A star type flow straightener allows radial movement of the flow and it is the best possible flow straightener to be used before the pressure measurement because it allows for flow profile and pressure development while preventing flow from swirling [12]. An illustration of a start type flow straightener is shown in Figure 4.7 and a dimensional drawing is in Appendix 2.

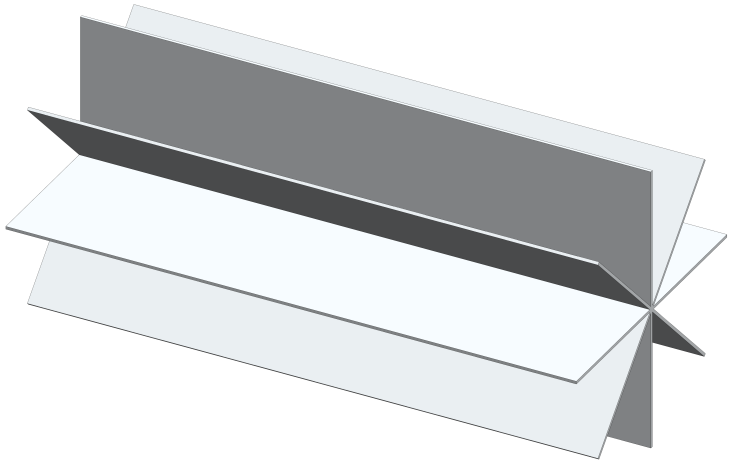

Figure 4.7: *Star type flow straightener.*

At the top end of the pipe there is a butterfly valve which is used to restrict the flow. The valve is manually operated which causes the operating point values to deviate slightly between measurements, because the flow contraction valve can't be adjusted exactly to the same position. A slight deviation of the operating point values is however insignificant because it doesn't matter how the points are divided along the operation curve as long as there is enough point resolution to capture the shape of the operation curve and the points are evenly distributed. More measurement points should be present in a range where a large operation curve gradient is present. [12]

4.2.4 Torque transducer

A torque transducer is located on the shaft between the pump and the electric motor. The torque transducer measures the torque input to the pump shaft and is part of the shaft with its couplings. The torque transducer type is Datum Electronics M420 with an operation range ±25 Nm [6]. A smaller torque measurement range of ±10 Nm would suffice for the normal pump operation with air, but a transducer with a wider range was selected in order to ensure that the pump start-up torque, which can easily exceed 10 Nm, doesn't break the transducer.

The torque transducer is coupled to the electric motor and to the pump with two flexible TRASCO/GP clutches. A big difference in the shaft diameters between the pump and torque transducer made the coupling problematic. The clutch connection to the pump shaft had to be lathed because the pump axle diameter is 42 mm and the torque transducer shaft diameter is 15 mm and such clutches are not for sale. The torque transducer has a digital signal output from the unit and the signal is routed to the data logger through a digital-to-analog conversion unit. The torque transducer and the assembled coupling is shown in Figure 4.8 and the schematics are in Appendix 3.

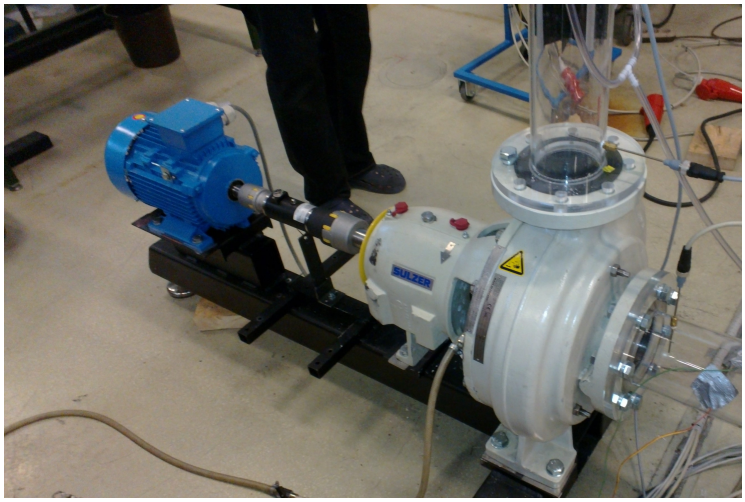

Figure 4.8: *Torque transducer with assembled coupling.*

4.2.5 Sensors and other measurement equipment

The sensors used in the measurement system are pressure sensors and temperature sensors. All directly measured variables with descriptions are listed in Table 4.1 and schematics of measurement system with sensor locations is in Appendix 3. The pump inlet and outlet air temperature and bearing temperature measurements are not part of the standard ISO 5801:2007. The bearing temperatures are measured in order to ensure similar operating conditions between the measurements, because the bearing temperatures have an effect on the torque values.

Table 4.1: *Direct sensor measurement variables and descriptions.*

Variable	Description
p_{e7}	gauge pressure upstream of flow rate measurement device
p_{e5}	gauge pressure downstream of flow rate measurement device
p_{e3}	gauge pressure at inlet pressure measurement section
p_{e4}	gauge pressure at outlet pressure measurement section
n	rotational speed at pump axle
M	torque at pump axle
T_a	ambient air temperature
h_u	air relative humidity
p_a	absolute ambient air pressure
T_{bear1}	bearing temperature 1 (closer to impeller)
T_{bear2}	bearing temperature 2 (closer to electric drive)
T_1	air temperature at pump inlet
T_2	air temperature at pump outlet
P_e	motor electrical input power (from inverter)

The measurement of the ambient air moisture level is done with a psychrometric method. The air moisture sensor has built-in psychrometric charts for converting the temperature difference to relative humidity [2]. The moisture sensor outputs dry bulb temperature and this temperature reading is used as the primary ambient air temperature. The ambient air conditions should be measured near the inlet pipe intake but in a location where the air is stationary [12]. The absolute ambient pressure is also needed in the calculations. An absolute air pressure sensor is placed at the same location as the moisture sensor. All the measurement sensor types and accuracies are listed in Table 4.2. [1, 2, 6, 10, 18]

Table 4.2: *Measurement sensor manufacturers, types and accuracies.*

Variable	Manufacturer	Type	Accuracy	Range
p_{e7}	Huba Control	699	±0,6 % FS	±0 . . . 1600 Pa
p_{e5}	Huba Control	699	±0,6 % FS	±0 . . . 2500 Pa
p_{e3}	Huba Control	699	±0,6 % FS	±0 . . . 2500 Pa
p_{e4}	Huba Control	650	±1,5 % FS	±0 . . . 2500 Pa
n	Datum Electronics	M420	±0,1 % FS	±0 . . . 3000 rpm
M_a	Datum Electronics	M420	±0,1 % FS	±0 . . . 25 Nm
T_a	ALNOR	Therm2246-2	±0,1 °C	−5 . . . 45 °C
h_u	ALNOR	Therm2246-2	±1 %	10 . . . 100 %
p_a	Freescale Semiconductor	MPX4115	±1,5 kPa	15 . . . 115 kPa
T_{bear1}	thermocouple wire	Type K	±1,5 °C	−40 . . . 375 °C
T_{bear2}	thermocouple wire	Type K	±1,5 °C	−40 . . . 375 °C
T_1	Nokeval	TRE-150-3.0-A	±0,15 °C	−30 . . . 350 °C
T_2	Nokeval	TRE-150-3.0-A	±0,15 °C	−30 . . . 350 °C
P_e	ABB	ACS800	±78,125 W	0 . . . 4000 W

The other measurement system equipment includes two DC voltage sources for the pressure sensors, a data logger HP 34970A and a desktop PC, which is connected to the data logger with a serial cable. One DC voltage source is adjusted to output 24 V for the measurement system gauge pressure sensors and the other is adjusted to output 5,1 V for the ambient air absolute pressure sensor. The data logger has three card modules installed:

- HP 34970A multifunction module for inverter measurements and control,
- HP 34901A for 4-wire RTD air temperature measurements T_1 and T_2,
- HP 34901A for 2-wire measurements of all the other variables.

The data logger has its own internal measurement accuracy which varies depending on the measurement. The accuracy includes the switching, conversion and measurement error of the data logger. The one year calibration values are used and relevant accuracies are listed in Table 4.3

Table 4.3: *HP 34970A data logger accuracies for different measurements.*

Measurement	± % of reading	± % of range	Absolute error
DC Voltage	0,0035	0,0005	
DC Current	0,050	0,005	
Temperature (RTD)			0,06 C°
Temperature (Thermocouple K)			1,0 C°

An electric motor and an inverter are also a part of the measurement system. The electric motor, which can be seen in Figure 4.8, is manufactured by Sino Growth and the motor type is MS 112M-2. The electric motor rated power is 4 kW and the rotational speed is 2880 rpm at 50 Hz. The motor is controlled with an AC inverter ABB ACS800, which is connected to the data logger. An analog output from the inverter outputs the electric motor power as a percentage of the rated power. The analog output is a constant current output with the range $0-20$ mA and a resolution of 10 bits which results in the range and accuracy listed in Table 4.2.

4.2.6 Measurement software

Fan measurement is a special task and there is no existing software solutions for it. General data logging software exists, but they fit poorly to fan measurement needs. The fan performance measurement includes a lot of data processing and calculations have to be performed to get the desired measurement output. This would require several post-processing steps with different software in addition to the data logging phase. A much more convenient way is to use only one software which can perform the calculations in the background. Therefore a specific new measurement software was coded with MATLAB. The software is designed to be easily modifiable to other types of measurement systems.

The software connects to the data logger with a RS-232 serial port and all the data logging is done using a serial connection. The software also controls the inverter and starting and stopping the pump and setting the pump speed can be done remotely. The main tasks of the software are:

- calculate the air properties and other measurement quantities from sensor readings using standardized algorithms,
- display relevant readings in physical quantities to the user,

- display operation and performance curves as they are measured,
- log and save measurement data to matrices.

The software has functions for monitoring the measurements, logging the raw data input and logging the operation and performance curves. The raw measurement function is used to measure the friction losses. The software implements all the calculations defined by the measurement standard ISO 5801:2007 and the underlying equations are presented in Chapter 5. A screenshot of the running software GUI is presented in Figure 4.9.

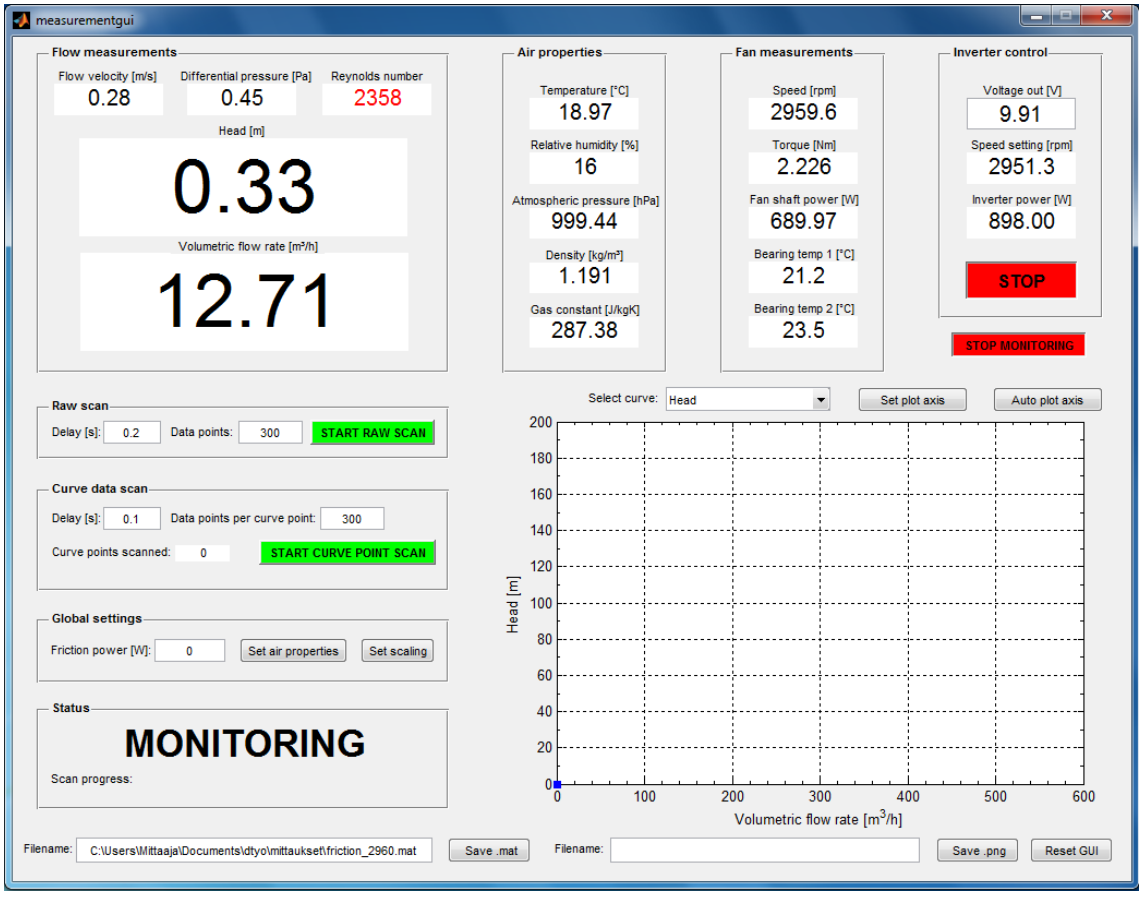

Figure 4.9: *Screenshot of measurement system GUI.*

4.3 Determination of friction losses

The determination of the bearing and seal friction losses is a crucial step in the pump performance measurement. The total work entering the fluid must be compared to the total work entering the impeller in order to determine the hydraulic performance of the pump. The total energy entering the impeller cannot be directly measured, because energy is transferred with the pump shaft which is attached to the bearing unit and seal in addition to the impeller. The torque measurement is placed between

the electric motor and the pump shaft and thus only the total torque (energy) entering the pump shaft can be measured. The only way to measure the energy entering the impeller is to deduct the bearing and seal friction losses from the total energy.

In order to measure the seal and bearing unit friction losses, the torque measurements were carried out when the impeller was removed. This ensures that no energy is transferred to the fluid and only the bearing and seal friction losses are using up the energy entering the pump shaft. An additional weight should be inserted in place of the impeller to make sure that bearing unit is under the precisely same radial load as it is when the impeller is in place. This procedure was not used in this thesis and it was assumed that the bearing and seal friction has only minimal dependency on the impeller gravitational force.

The friction measurements were carried out for the original bearing unit and for the lighter unit with ball bearings. In order to determine the ratio between the bearing and the seal friction, additional measurements were done with the seal removed. This way only the bearing unit is the source of friction loss which can be measured directly from pump the shaft with the torque transducer. The seal friction can then be calculated by subtracting the bearing friction from the total friction. Measurements without the seal were done only with the original heavier bearing unit, but a similar seal friction should be present in the lighter unit because the seal type is the same.

It was found that the bearing unit requires a significant warm-up time before the torque level reached a stable value. The bearing unit temperature seems to affect the torque measurement stability as well as the torque levels. With cold bearings, the torque ripple and torque levels were higher. This behavior is expected because the temperature affects the material properties of the lubricant. As the lubricant warms up because of viscous friction, the operation of the bearing unit stabilizes.

In order to monitor the bearing unit temperature, two K-type thermocouples were attached to the side of the bearing unit. These temperature measurements were used for monitoring the warm-up and for determining when similar and stable operating conditions were reached. It was determined that at least a half an hour warm-up period at full speed is needed to reach stable temperatures. It was also found that rotational speed affects the bearing temperature and temperatures drop when the speed is lower. This is because the friction forces of the bearings and the seal are proportional to the rotational speed and the heat generation due to friction is therefore lower.

4.4 Measurement method

All operation and performance curves presented in the thesis are measured with the same measurement equipment. The pump bearing unit was warmed to similar temperatures before every measurement. The warm-up was done by running the pump at full speed until stable operating conditions were reached. The seal cooling liquid flow was checked before every run. The electrical equipment had a minimum warm-up time of one hour before any measurements were done. The gauge pressure sensors and torque transducer zero levels were set after the warm-up time before performing the actual measurement runs. The zero levels were also checked and set between measurement runs at different rotational speeds.

A pump or a fan produces a seemingly steady flow but the underlying process is unsteady. The periodic nature of the underlying pumping process causes pressure pulsation and flow rate fluctuation. This shows up in the flow rate and pressure measurements as ripple around an average value. A significant amount of single measurements need to be recorded and averaged in order to get a representative value of an operation curve point. The amount of measurements per curve point directly affects the total time required for measurements. Based on the recommendations of the standard ISO 5801:2007 and experimental measurements, it was decided that the following configuration for the measurements would be used:

- 300 single measurements cycles per curve point are taken with a delay of 0,1 s,
- 3000 single measurements cycles per friction measurement are taken with a delay of 0,1 s.

Arithmetic average of single measurements cycles is used as a measurement result and the standard deviation is calculated to be used in the calculation of the measurement error. In addition to the 0,1 s delay between the measurements an internal switching delay of the data logger exists. The switching delay is around 0,2 s for one measurement cycle. It would have been possible to use a smaller delay between the measurement cycles with the sensors and the data logger, but a longer time frame is chosen because it averages the underlying flow instability. The torque measurements proved to be particularly difficult and that is why a significantly larger sample size was used in the friction measurements. The seal and bearing friction results based on torque measurements are used in efficiency calculations and they need to as accurate as possible.

The operation and performance curves were measured at 11 different rotational speeds per impeller starting from 2960 rpm and down to 1470 rpm with steps of 150 rpm. All the curves presented in Chapter 6 are measured and not calculated with the affinity rules. The friction measurements were done at the same rotational

speeds as the operation curve measurements. The selected rotational speed range represents the useful operation range of the pump in real applications.

The pump has an adjustable gap between the casing and the impeller. The gap between the impeller and the casing determines the volumetric losses of the device. The volumetric losses rise in time because the gap becomes larger due to abrasion. An adjustable gap is used in order to take into account the effect of abrasion. The gap size can be adjusted outside the pump using three bolts which move a ring shaped piece of the casing axially inside the pump.

The effect of the gap size on operation and performance curves was studied by performing measurements with two different gap sizes. The normal operation setting for the gap size is 0,5 mm and it's used as a first measurement setting. The gap size cannot be directly measured inside the pump. The adjustment bolt threads have a specified rise and one third of a revolution corresponds to 0,5 mm of gap size. The first setting is achieved by closing the gap completely and then opening the bolts one third of a revolution. In another measurement setting the gap is fully open which means that the gap is as wide as possible. From counting the revolutions this represent a gap size of 1,0 ... 1,5 mm which is denoted by 1,0 + mm in the results. The measurements of the gap effect were not done at every rotational speed but with steps of 300 rpm in the speed range.

5. CALCULATION OF RESULTS

This chapter presents the equations and calculation procedure to get the results from the raw sensor measurements. The calculations are presented starting from raw sensor measurements from the data logger. The calculation procedure is entirely based on the standard ISO5801:2007 and transfer functions of the raw readings are sensor specific.

5.1 Air properties

Air is considered as an adiabatic compressible ideal gas by the standard ISO5801:2007. The ambient air property measurements are important because they are needed in almost every other measurement variable calculation. The air properties are measured constantly and updated during every measurement cycle.

The ambient air pressure p_a is a directly measured variable. The other required variables are the ambient air temperature T_a and the ambient air density ρ_a. The ambient air temperature is also a directly measured variable but the density needs to be calculated. Ambient air is a mixture of water vapor and dry air and the water vapor content along with the ambient pressure and temperature determine the density of the gas mixture. The water vapor content is measured with the moisture sensor.

The moisture sensor, which is based on the psychrometric method, measures the dry bulb and wet bulb temperature of the ambient air. Dry bulb temperature T_d is the same as the ambient air temperature T_a. The wet bulb temperature T_w is the temperature of a wet bulb which is artificially moisturized all the time and a small fan generates air flow around the wet bulb. The air flow causes evaporation of water to the ambient air and the rate of evaporation is proportional to the moisture difference between the wet bulb and the ambient air. The evaporation transfers heat away from the wet bulb and causes T_w to drop.

The temperature difference between the dry bulb temperature T_d and the wet bulb temperature T_w is therefore dependent on the evaporation rate, which itself depends on the moisture difference. For example, if the ambient air relative humidity h_u is already 100 %, no water can be evaporated and the evaporation rate is zero which means that the temperature difference between the bulbs is also zero. The psychrometric moisture measurement method is simple and robust, but requires

some maintenance to ensure adequate air flow and moisturizing.

The saturation pressure of water vapor p_{sat} depends on temperature and psychrometric charts or correlations can be used to determine it. The moisture sensor used has inbuilt psychrometric charts and it directly outputs the ambient air relative humidity h_u along with the ambient air dry bulb temperature T_d [2]. The relative humidity is a relation of partial water vapor pressure p_v of the air to the saturation water vapor pressure p_{sat} at a given temperature. Relative humidity is defined by equation (5.1), where $(p_{sat})_{T_d}$ is the saturation water vapor pressure at the dry bulb temperature. [12]

$$h_u = \frac{p_v}{(p_{sat})_{T_d}} \quad \Rightarrow \quad p_v = h_u \, (p_{sat})_{T_d} \tag{5.1}$$

As the relative humidity h_u is a directly measured variable, only saturation water vapor pressure is needed in order to calculate the partial water vapor pressure of ambient air. The measurement standard ISO5801:2007 provides a formula for calculating $(p_{sat})_{T_d}$ and the correlation is defined by equation (5.2). Equation (5.2) is valid from 0 °C to 100 °C. [12]

$$\begin{aligned} (p_{sat})_{T_d} &= 610{,}8 + 44{,}442 T_d + 1{,}4133 T_d^2 + 0{,}02768 T_d^3 \\ &\quad + 2{,}55667 \times 10^{-4} T_d^4 + 2{,}89166 \times 10^{-6} T_d^5 \end{aligned} \tag{5.2}$$

In order to relate the partial water vapor pressure to the gas properties of humid air, the ideal gas law is applied. The ideal gas law in its basic form is defined by equation (5.3), where n is the molar amount of the gas, V is volume of the gas, Θ is temperature of the gas in $[K]$ and R_u is the universal gas constant and $R_u = 8{,}13447\,\mathrm{J/mol\,K}$. [5, 16]

$$pV = nR_u\Theta \tag{5.3}$$

Equation (5.3) can be modified by inserting the definition $n = m/M$, where m is the mass of the gas and M is the molar mass of the gas, along with the definition of density. This leads to a modified form of the ideal gas law which is presented in equation (5.4). Because R_u is an universal constant and M a gas specific material property, their relation is also constant and is called the specific gas constant $R_{spec} = R_u/M$.

$$p = \rho \frac{R_u}{M} \Theta \quad \Rightarrow \quad p = \rho R_{spec} \Theta \tag{5.4}$$

The state of an ideal gas at any point can be determined from equation (5.4) if two of the variables are known. In order to apply equation (5.4) to ambient air density calculation, specific gas constant of humid air R_w needs to be determined first. Following the assumption that air is treated as an ideal gas mixture, the value

of humid air gas constant must be between dry air specific gas constant R and water vapor specific gas constant R_v. The exact value of R_w depends on the air humidity which is defined as the relation of partial water vapor pressure p_v to total ambient air pressure p_a. A formula for calculating the humid air gas constant based on the relative difference between dry air and water vapor specific gas constants is given in ISO 5801:2007 and defined by equation (5.5). The values of known constants $R = 287\,\mathrm{J/kg\,K}$ and $R_v = 461\,\mathrm{J/kg\,K}$ can be inserted in equation (5.5) for simplicity. [12]

$$R_w = \frac{R}{1 - \left(\frac{R_v - R}{R_v}\right)\frac{p_v}{p_a}} = \frac{287}{1 - 0{,}378\frac{p_v}{p_a}} \tag{5.5}$$

The density of the ambient air can now be calculated from equation (5.4) using the result from equation (5.5) and the measured values of p_a and $\Theta_a = T_a + 273{,}15$. The density of humid air at any given section x of the measurement system is calculated using equation (5.6) assuming that the absolute pressure p_x and temperature Θ_x are known.

$$\rho_x = \frac{p_x}{R_w \Theta_x} \tag{5.6}$$

The stagnation temperature of air is an important variable when air is considered as an adiabatic ideal gas. The stagnation temperature is the temperature of the moving gas when it's brought adiabatically to rest [5, 12]. This means that the stagnation temperature of the air doesn't change in the inlet pipe although air velocity and pressure can change. This is formally expressed with equation (5.7).

$$\Theta_{sg1} = \Theta_{sg3} = \Theta_a \tag{5.7}$$

The stagnation temperature is affected by any device which insert energy into the air. The stagnation temperature downstream of the pump is defined by equation (5.8) where P_r is the impeller power, q_m is the mass flow rate and c_p is the heat capacity of air at constant pressure. The value of $c_p = 1008\,\mathrm{J/kg\,K}$ is used in the initial calculations. [12]

$$\Theta_{sg2} = \Theta_{sg1} + \frac{P_r}{q_m c_p} = \Theta_{sg4} \tag{5.8}$$

The stagnation temperature is always higher than the temperature of the fluid. The fluid temperature can be related to the stagnation temperature using Mach number Ma_x and equation (5.9), where κ is the isentropic exponent for an ideal gas and for air it has the value $\kappa = 1{,}4$ [12]. Equation (5.9) implies that the temperature of the fluid depends on its velocity at a given section. Equation (5.9) is valid for

$\kappa = 1{,}4$ and $Ma_{sgx} < 0{,}45$.

$$\frac{\Theta_{sgx}}{\Theta_x} = 1 + \frac{\kappa - 1}{2} Ma_x^2 \tag{5.9}$$

If the flow velocity is known, the fluid temperature can be calculated from equation (5.10). The heat capacity c_p can be expressed using the relation of the gas constant R_w to heat capacity c_V and c_p. The relation $R_w = c_V - c_P$ and the definition of the isentropic exponent $\kappa = c_p/c_v$ lead to equation $c_p = (\kappa/(\kappa - 1))\, R_w$ for the heat capacity in constant pressure.

$$\Theta_x = \Theta_{sgx} - \frac{v_x^2}{2c_p} = \Theta_{sgx} - \frac{v_x^2}{2\,(\kappa/(\kappa - 1))\, R_w} \tag{5.10}$$

The dynamic viscosity of air is temperature dependent and a correlation equation (5.11) is used. Equation (5.11) is valid from $-20\,^{\circ}\mathrm{C}$ to $100\,^{\circ}\mathrm{C}$ [12]. The kinematic viscosity ν is calculated with equation (2.38).

$$\mu = (17{,}1 + 0{,}048 T_x) \times 10^{-6} \tag{5.11}$$

5.2 Flow rate

The flow rate is measured using an orifice plate with D and $D/2$ wall pressure tapings and the location of the pressure measurements is presented in Appendix 3. The inlet pipe inner diameter is $D_1 = D_3 = 126\,\mathrm{mm}$ and the orifice diameter is $d = 81{,}9\,\mathrm{mm}$. Using the convention of standard ISO5801:2007, the upstream pressure measurement plane in the inlet pipe has subscript 7 or u and downstream pressure measurement plane has subscript 5 or do. The pressure difference Δp is defined by $\Delta p = p_u - p_{do} = p_7 - p_5 = p_{e7} - p_{e5}$. The upstream density ρ_u is calculated from equation (5.6) using air properties of the corresponding measurement plane. The ratio of the orifice diameter to the inlet pipe diameter $\beta = d/D$ is a defining parameter for any pressure differential flow rate measurement device and is needed in the calculations. For the used measurement system β has the value $\beta = 0{,}0819/0{,}126 = 0{,}65$.

The general formula for calculating the mass flow rate using a pressure differential device is equation (5.12), where α is the flow rate coefficient, ε is the expansibility factor, ρ_u is the upstream density and Δp is the pressure difference over the device. [12]

$$q_m = \alpha \varepsilon \pi \frac{d^2}{4} \sqrt{2 \rho_u \Delta p} \tag{5.12}$$

The flow rate coefficient α and the expansibility factor ε are experimental variables and calculated using correlations. The flow rate coefficient α depends on

the Reynolds number Re_D which in turn depends on the velocity in the inlet pipe. This dependency leads to an iterative calculation of the mass flow rate using equation (5.12) and the flow rate coefficient equation (5.13) which is called the Stolz formula [12]. Other formulations for α exist and one them is the Reader-Harris/Gallagher equation which is used in the standard ISO 5197-2:2003 along with a different formulation for ε [11]. The Stolz formula is used to fulfill the requirements of the standard ISO 5801:2007.

$$\begin{aligned}\alpha &= \left(1-\beta^4\right)^{-0,5}\left[0{,}5959+0{,}0312\beta^{2,1}-0{,}184\beta^8+0{,}0029\beta^{2,5}\left(\frac{10^6}{Re_D}\right)^{0,75}\right. \\ &\quad \left.+0{,}039\beta^4\left(1-\beta^4\right)^{-1}-0{,}0158\beta^3\right] \end{aligned} \tag{5.13}$$

The expansibility factor ε only depends on constants and the pressure difference Δp and can be calculated directly. The expansibility factor is defined by equation (5.14) [12]. The expansibility factor doesn't change inside the iteration loop and needs to be calculated only once in every measurement cycle.

$$\varepsilon = 1-\left(0{,}41+0{,}35\beta^4\right)\frac{\Delta p}{\kappa p_u} \tag{5.14}$$

The flow velocity can be expressed with the pressure difference Δp by first using the definition of mass flow rate, which leads to equation (5.15). Substituting equation (5.12) into equation (5.15) and inserting the result into the definition of Reynolds number equation (5.16) leads to a useful formulation of Reynolds number. The final form can be directly used in the iterative calculation of mass flow rate.

$$q_m = \rho_u q_V = \rho_u v_D A_D = \rho_u v_D \pi \frac{D^2}{4} \quad \Rightarrow \quad v_D = \frac{4q_m}{\rho_u \pi D^2} \tag{5.15}$$

$$Re_D = \frac{Dv_D}{\nu} = \frac{4q_m}{\pi D\mu} = \frac{\alpha\varepsilon d^2}{\nu D}\sqrt{\frac{2\Delta p}{\rho_u}} = \frac{\alpha\varepsilon\beta d}{\nu}\sqrt{\frac{2\Delta p}{\rho_u}} \tag{5.16}$$

Prior to iterative flow rate calculation initial guess values are needed. As the fluid temperature is a function of yet unknown flow velocity, an initial guess has to be made. The initial values for upstream air kinematic viscosity ν_7 and air density ρ_7 are calculated using ambient air temperature $\Theta_7 = \Theta_a$ and using equations (5.6), (5.11) and (2.38). The initial value for the flow rate coefficient α is calculated using equation (5.13), but leaving out the fourth term inside the brackets which contains the yet unknown variable Re_D. The initial value for Reynolds number Re_D is calculated from equation (5.16) using other initial guess values.

It is now possible to calculate first estimate for the mass flow rate q_m using equation (5.12). The first value for flow velocity v_D can be calculated from equation (5.15) using the first value of q_m. After the initial calculation iteration the loop is started. The iteration procedure is continued until the relative error between iteration rounds is below 10^{-8}. The relative error is calculated with equation (5.17).

$$err = |1 - q_m/q_{m,old}| \tag{5.17}$$

The iteration loop goes through the following steps:

1. Update upstream air temperature Θ_7 using equation (5.10).
2. Update material properties using Θ_7 and equations (5.6), (5.11) and (2.38).
3. Calculate Reynolds number Re_D using equation (5.16).
4. Calculate flow rate coefficient α from equation (5.13).
5. Calculate mass flow rate q_m using equation (5.12).
6. Update inlet pipe flow velocity v_D using equation (5.15).
7. Check convergence with equation (5.17) and return to step one or break loop if convergence is reached.

The mass flow rate q_m is solved in every measurement cycle. The flow velocity v_D is calculated using equation (5.15). The volumetric flow rate q_{Vsg1} is defined by equation (5.18), where inlet stagnation density ρ_{sg1} is defined by equation (5.19). This definition of the volumetric flow rate which uses the inlet stagnation conditions is used in the measurement results. The iteration procedure is fast and uses only tens of milliseconds on the measurement computer.

$$q_{Vsg1} = \frac{q_m}{\rho_{sg1}} \tag{5.18}$$

$$\rho_{sg1} = \frac{p_{sg1}}{R_w \Theta_{sg1}} \tag{5.19}$$

5.3 Fan pressures

Two different pressures are used when calculating fan pressures. The normal pressure p or p_e is the measurable total pressure value and the stagnation pressure p_{sg} or p_{esg} is the pressure which is attainable if the fluid flow is brought to rest isentropically. The location of the pressure sensors is shown in Appendix 3. Both pressures can be used to calculate the total fan pressure, but usually the fan pressure p_{fD} refers to the difference between the stagnation pressure of the fan inlet and outlet

and is calculated with equation (5.20). This is also how the fan pressure is defined in the standard ISO5801:2007. The static fan pressure p_{sfD} is calculated with equation (5.21) and is always smaller than the fan pressure calculated with stagnation pressures. The subscript D refers to the measurement system installation category in the standard ISO 5801:2007.

$$p_{fD} = p_{esg2} - p_{esg1} = p_{sg2} - p_{sg1} \tag{5.20}$$

$$p_{sfD} = p_{e2} - p_{esg1} = p_2 - p_{sg1} \tag{5.21}$$

The difference between the stagnation and total pressure increases when the Mach number Ma and flow velocity in the outlet pipe rises. The measurement standard ISO5801:2007 specifies that if the reference Mach number Ma_{2ref} is smaller than 0,15, the flow can be regarded incompressible. The Mach number at section x is defined by equation (5.22), where A_x is the area of the section, v_x is the mean flow velocity at the section and $c_x = \sqrt{\kappa R_w \Theta_x}$ is the speed of sound at that section. The reference Mach number Ma_{2ref} is calculated with equation (5.22) at fan outlet using the properties of atmospheric air.

$$Ma_x = \frac{v_x}{c_x} = \frac{q_m}{A_x \rho_x \sqrt{\kappa R_w \Theta_x}} \tag{5.22}$$

In this thesis the compressible form of the equations is always applied and the compressibility effects are taken into account. This makes the calculations somewhat more complex but at the same time allow the measurement system software to be used with high pressure fans without modification.

The Mach correction factor f_{Mx} is used in order to correct the fan pressure with compressibility effects and is defined by equation (5.23). The Mach correction factor is close to unity when the flow velocities are small.

$$f_{Mx} = \frac{p_{sgx} - p_x}{p_{dx}} \tag{5.23}$$

5.3.1 Fan inlet pressure

The fan inlet pressure p_{e1} or $p_1 = p_{e1} + p_a$ and the fan inlet stagnation pressure p_{esg1} or p_{sg1} is a calculated value because the inlet pipe pressure measurement plane is not located at the fan inlet but at a distance of $3D_3$ upstream. The location of the pressure sensors is shown in Appendix 3. The inlet side stagnation pressure at the measurement plane is called p_{e3} or $p_3 = p_{e3} + p_a$. In order to calculate the fan inlet stagnation pressure p_{esg1}, the pressure p_{esg3} at the pressure measurement plane needs to be determined first. The flow friction pressure loss between the inlet

pressure measurement plane and fan inlet plane needs to be calculated.

The calculation of the stagnation pressure p_{esg3} is done first and it requires the calculation of the Mach number and the Mach number correction factor f_{M3}. The calculation of the Mach number Ma_x and fluid temperature Θ_x can be done if the pressure p_x and the stagnation temperature Θ_{sgx} are known and this is the case at the inlet pressure measurement plane. M^2 is introduced to simplify the calculation and is defined by equation (5.24).

$$M^2 = \left(\frac{q_m}{A_x}\right)^2 \frac{\kappa - 1}{2\kappa} \frac{R_w \Theta_{sgx}}{p_x^2} \tag{5.24}$$

The fluid temperature is related to the stagnation temperature by equation (5.9) which contains an unknown variable Ma_x. The same relation can also be expressed using M^2 to solve Θ_x and further to solve Ma_x. The temperature relation using M^2 is presented in equation (5.25). The Mach number Ma_x can then be solved from equation (5.26).

$$\frac{\Theta_{sgx}}{\Theta_x} = \frac{1 + \sqrt{1 + 4M^2}}{2} \tag{5.25}$$

$$Ma_x = \sqrt{\left(\frac{\Theta_{sgx}}{\Theta_x} - 1\right) \frac{2}{\kappa - 1}} \tag{5.26}$$

M^2 is calculated first using equation (5.24) at inlet pressure measurement plane with p_3, A_3 and $\Theta_{sg3} = \Theta_a$. Next temperature Θ_3 is solved from equation (5.25) and finally the Mach number Ma_3 is calculated using equation (5.26). The density ρ_3 is calculated using equation (5.6) and the flow velocity v_3 at the inlet pressure measurement plane is calculated using equation (5.15).

In order to calculate the Mach correction factor f_{M3}, the stagnation pressure p_{sg3} and the dynamic pressure p_{d3} have to be calculated. The stagnation pressure p_{sg3} can be calculated with equation (5.27) when Ma_3 and p_3 are known. The dynamic pressure is defined by equation (5.28).

$$p_{sgx} = p_x \left(1 + \frac{\kappa - 1}{2} Ma_x^2\right)^{\frac{\kappa}{\kappa - 1}} \tag{5.27}$$

$$p_{dx} = \rho_x \frac{v_x^2}{2} = \frac{1}{2\rho_x} \left(\frac{q_m}{A_x}\right)^2 \tag{5.28}$$

The Mach correction factor f_{M3} can now be calculated using equation (5.23). The conditions at inlet pressure measurement plane are now fully resolved and the solution can proceed to solve p_{sg1} at the fan inlet. The fan inlet stagnation pressure p_{sg1} is calculated with equation (5.29), where $(\xi_{3-1})_3$ is the conventional friction

coefficient.

$$p_{sg1} = p_3 + \frac{1}{2}\rho_3 v_3^2 f_{M3} \left[1 + (\xi_{3-1})_3\right] \tag{5.29}$$

The conventional friction coefficient $(\xi_{3-1})_3$ is negative and takes into account the pipe friction pressure loss in the pipe section between the pressure measurement plane and the fan inlet. The conventional friction coefficient $(\xi_{3-1})_3$ is calculated with equation (5.30), where the Reynolds number Re_{D3} is calculated from equation (5.16) with v_3, ρ_3 and μ_3 calculated from equation (5.11) using Θ_3.

$$(\xi_{3-1})_3 = -\left(0{,}015 + 1{,}26 Re_{D3}^{-0{,}3}\right) \tag{5.30}$$

The fan inlet stagnation pressure p_{sg1} is calculated from equation (5.29) after calculating the conventional friction factor from equation (5.30). The pressure p_1 needs to be solved, because the density ρ_1 is needed to calculate the average fluid density ρ_m with equation (5.31).

$$\rho_m = \frac{\rho_1 + \rho_2}{2}. \tag{5.31}$$

The fluid temperature Θ_1 needs to be solved first. The fluid temperature can be solved using the stagnation Mach number Ma_{sg1} and the Mach number relation to the fluid and stagnation temperature. The fluid stagnation density ρ_{sg1} is solved first with p_{sg1} and $\Theta_{sg1} = \Theta_a$ using equation (5.6). The stagnation Mach number can be solved from the modified form of equation (5.22), which is achieved by inserting $\rho_x = p_x / R_w \Theta_x$ into equation (5.22) and using the stagnation air properties. The modified form is presented in equation (5.32). After solving Ma_{sg1} from equation (5.32), the Mach number at the fan inlet is solved from equation (5.33).

$$Ma_{sgx}^2 = \frac{q_m^2}{A_x^2 \rho_{sgx}^2 \kappa R_w \Theta_{sgx}} = \frac{q_m^2}{A_x^2 \kappa p_{sgx} \rho_{sgx}} \quad \Rightarrow \quad Ma_{sgx} = \sqrt{\frac{q_m^2}{A_x^2 \kappa p_{sgx} \rho_{sgx}}} \tag{5.32}$$

$$Ma_x = Ma_{sgx} \sqrt{1 + 1{,}217 Ma_{sgx}^2 + 1{,}369 Ma_{sgx}^4 + 10 Ma_{sgx}^6} \tag{5.33}$$

When Mach number Ma_1 is known, temperature Θ_1 is solved from equation (5.9). Solving the Mach number also enables the calculation of pressure p_1 using equation (5.27). Having solved both p_1 and Θ_1, the desired density ρ_1 can now be solved from equation (5.6) and this concludes the calculation of fan inlet pressure.

5.3.2 Fan outlet pressure

The calculation of the fan outlet pressures p_{sg2} and p_2 follows almost the same procedure as the calculation of the fan inlet pressure. The location of the pressure

sensors is shown in Appendix 3. The calculation procedure is briefly introduced and the differences are highlighted. The outlet pipe pressure measurement plane is located at a distance of $5D_4$ downstream from the fan outlet. The outlet pipe inner diameter differs from the inlet pipe inner diameter and is 100 mm.

A flow straightener is located between the fan outlet and the pressure measurement plane. The swirl in the flow would affect the pressure readings at the outlet pressure measurement because the rotating fluid velocity would lower the sensible pressure. The swirl velocity is impossible to measure and to take into account and that's why any swirl has to be eliminated from the flow before the outlet pressure measurement.

The first difference in the calculations is in the stagnation temperature Θ_{sg4} which now includes the impeller power P_r. The stagnation temperature Θ_{sg4} is calculated with equation (5.8). It should be noted that the outlet stagnation temperature doesn't include the friction losses and useful energy of the outflow.

The calculation of the pressure p_{sg4} proceeds with calculation of the stagnation temperature Θ_{sg4} and then calculating M^2 and the fluid temperature Θ_4 from equations (5.24) and (5.25). The density ρ_4 is updated using Θ_4 and equation (5.6) and the calculated value is used to update the velocity v_4 with equation (5.15). Next the Mach number Ma_4 is calculated from equation (5.26). When the Mach number Ma_4 is known, the stagnation pressure p_{sg4} and the dynamic pressure p_{d4} are calculated using equations (5.27) and (5.28). Finally the Mach correction factor f_{M4} is calculated using equation (5.23). The pressure is now resolved at the pressure measurement plane and the calculation proceeds to resolve the pressure at the fan outlet.

The pressure losses between the fan outlet and the pressure measurement plane are taken into account with the conventional friction coefficient $(\xi_{2-4})_4$. In the outflow pipe these pressure losses include the pipe friction pressure loss and also the pressure loss resulting from the flow straightener in the outlet pipe. The outlet pipe conventional friction coefficient is calculated with equation (5.34), where Re_{D4} is calculated with equations (5.16) and (5.11). The last term on the right is the friction factor of the flow straightener.

$$(\xi_{2-4})_4 = 0{,}015 + 1{,}26Re_{D4}^{-0,3} + 0{,}95Re_{D4}^{-0,12} \tag{5.34}$$

The pressure at the fan outlet is calculated with equation (5.35). At the outlet side, the friction losses are added to the pressure reading contrary to the inlet side where they are subtracted.

$$p_{sg2} = p_4 + \frac{1}{2}\rho_4 v_4^2 f_{M4}\left[1 + (\xi_{2-4})_4\right] \tag{5.35}$$

Additional calculations are needed at the fan outlet in order to solve the pressure p_2. The stagnation Mach number Ma_{sg2} is calculated using stagnation air properties and equation (5.32). The Mach number Ma_2 is then calculated using equation (5.33). The fluid temperature Θ_2 is calculated from equation (5.9). The outlet pressure p_2 is solved from equation (5.27) and finally the density ρ_2 is calculated using equation (5.6). This concludes the calculation of the fan outlet pressure. The fan pressures p_{fD} and p_{sfD} can now be calculated using equations (5.20) and (5.21).

5.4 Efficiencies

5.4.1 Fan air power and impeller power

The fan efficiencies are calculated by comparing the fan air power to different input power values. The fan air power P_{uD} and the static fan air power P_{usD} represent the amount of energy that has entered to the fluid and input power values represent the energy input to the system. Relating these values yields the efficiencies. Several different efficiency values can be calculated for fans.

In order to calculate the efficiencies, the fan air power and the static fan air power need to be calculated first. The fan air power is defined by equation (5.36) and the fan static power is defined by equation (5.37). In equation (5.36), k_p is the compressibility coefficient which takes the compressibility effects into account. When calculating the static fan pressure from equation (5.37) the same parameter is called k_{ps}.

$$P_{uD} = q_{Vsg1} p_{fD} k_p \tag{5.36}$$

$$P_{usD} = q_{Vsg1} p_{sfD} k_{ps} \tag{5.37}$$

The compressibility coefficients k_p and k_{ps} are calculated with equation (5.38), where r and Z_k are temporary variables defined by equations (5.39) and (5.40). The static compressibility coefficient k_{ps} is calculated similarly with equation (5.38), but the fan pressure p_{fD} is replaced by the static fan pressure p_{sfD} in equations (5.39) and (5.40).

$$k_{ps} \text{ or } k_p = \frac{Z_k \log_{10}(r)}{\log_{10}[1 + Z_k (r-1)]} \tag{5.38}$$

$$r = 1 + \frac{p_{fD}}{p_{sg1}} \tag{5.39}$$

$$Z_k = \frac{\kappa - 1}{\kappa} \frac{P_r}{q_{Vsg1} p_{fD}} \tag{5.40}$$

The electrical input power P_e is a directly measured value from the inverter and it doesn't need to be calculated. The fan shaft power P_a is an indirectly measured

value and is calculated from the measured shaft torque M_a and the rotational speed n using equation (3.6).

The impeller power P_r is calculated by subtracting the combined seal and bearing friction P_{fric} from the shaft power P_a. This is defined by equation (5.41). The friction power P_{fric} is determined using equation (3.6) the pump with the impeller removed. The determination of impeller power P_r is the largest error source in the efficiency calculations, because P_{fric} can be several times larger than the impeller power P_r in fan usage.

$$P_r = P_a - P_{fric} = P_a - (P_{seal} + P_{bear}) \tag{5.41}$$

5.4.2 Fan efficiencies

The conventional fan efficiency η_{rD} is defined by equation (5.42). The fan efficiency compares the fan air power P_{uD} to the impeller power P_r.

$$\eta_{rD} = \frac{P_{uD}}{P_r} \tag{5.42}$$

Another efficiency definition is the static fan efficiency η_{srD}, which compares the static fan air power P_{usD} to the impeller power and is defined with equation (5.43). The static fan efficiency is always lower than conventional fan efficiency. The difference between the two increases when flow velocity in the outlet pipe increases.

$$\eta_{srD} = \frac{P_{usD}}{P_r} \tag{5.43}$$

Efficiency can also be calculated against the shaft power P_a and this is called the fan shaft efficiency and is defined by equation (5.44). The fan shaft efficiency is calculated by comparing the air power to the power entering the shaft. The fan shaft efficiency thus takes the bearing and seal losses into account and is lower than the efficiencies calculated using the impeller power. The fan static shaft efficiency can be calculated similarly using static air power.

$$\eta_{aD} = \frac{P_{uD}}{P_a} \tag{5.44}$$

Finally the total or the electrical efficiency η_{eD} can be calculated with the electrical input power P_e to the system. The electrical efficiency can be regarded as the total efficiency of the fan system since it includes all the possible losses. The electrical efficiency is defined by equation (5.45) and has by definition the lowest value of all the efficiencies.

$$\eta_{eD} = \frac{P_{uD}}{P_e} \tag{5.45}$$

5.5 Fan efficiency using thermodynamic measurement method

The impeller power can be measured indirectly with the temperature readings Θ_{sg1} and Θ_{sg2} if mass flow rate q_m is known. The location of the temperature sensors is shown in Appendix 3. The impeller power P_r can be solved from equation (5.8) which leads to equation (5.46). Equation (5.46) implies that the impeller power is directly proportional to the difference between the stagnation temperature values.

$$\Theta_{sg2} = \Theta_{sg1} + \frac{P_r}{q_m c_p} \quad \Rightarrow \quad P_r = q_m c_p \left(\Theta_{sg2} - \Theta_{sg1}\right) \tag{5.46}$$

Equation (5.46) exploits the fact that all energy entering the impeller is transferred to the fluid. Some of the transferred energy is in useful form as the fan air power but some of the energy is wasted through viscous dissipation which transforms kinetic energy directly into heat. After the impeller power P_r is determined from equation (5.46), the fan air powers can be calculated as before with equations (5.36) and (5.37). The temperature based measurement is therefore an alternative way to measure the fan efficiencies.

However, measuring the fluid flow temperature accurately is difficult. The difficulties arise from the fact that the temperature rise is very low even with air, which has a significantly lower heat capacity than that of water. Another problem is that the measured temperature is neither the stagnation temperature Θ_{sg} or the fluid temperature Θ but something in between. This is because in reality fluid doesn't slow down isentropically when it collides with the stagnation point formed by the temperature probe. In an isentropic process, the fluid temperature is related to the stagnation temperature with equation (5.10).

The losses of the non-isentropic deceleration are accounted by using a recovery factor r_r in equation (5.10) which leads to equation (5.47), where Θ_{probex} is the sensible temperature reading from the temperature sensor probe. The recovery factor r_r represents the fraction of kinetic energy transferred to the probe. Literature suggest several values for recovery factor r_r depending on the probe installation and a value $r_r = 0{,}68$ is used for a probe that is parallel to the flow [15]. The flow velocity v_x is a known variable from the separate mass flow rate measurement. The stagnation temperature Θ_{sgx} is solved from equation (5.47).

$$\Theta_{sgx} = \Theta_x + \frac{v_x^2}{2c_p} \quad \Rightarrow \quad \Theta_{probex} = \Theta_x + r_r \frac{v_x^2}{2c_p} = \Theta_{sgx} + \left(r_r - 1\right) \frac{v_x^2}{2c_p} \tag{5.47}$$

Further difficulties are introduced by the heat transfer effects to the surroundings. The heat transfer to surroundings can be rather complex and impossible to take into account by calculations. The effect of heat transfer is minimized by placing the

temperature probes directly upstream of the inlet and downstream of the outlet. Some heat transfer will still be transferred through the pump metal casing, but it is neglected in the calculations.

5.6 Errors

The standard ISO5801:2007 specifies that the measurement errors are calculated using the root-sum-square method. For each measurement the uncertainty U is calculated using equation (5.48), where B is the systematic uncertainty or the bias limit, t_{95} is the t-distribution uncertainty factor based on the 95 % confidence level and s is the random measurement error or precision index. In the current measurements the sample size is $N = 300$ and the t-distribution confidence level has the value $t_{95} = 1{,}96$. [12, 15]

$$U_i = \sqrt{B^2 + (t_{95}s)^2} \tag{5.48}$$

The precision index is s calculated for each data point using the standard deviation function of MATLAB. The standard deviation s is calculated using equation (5.49), where y_i is the single measured value and $\bar{y}$ is the mean value of the data point. [15]

$$s = \sqrt{\frac{1}{N}\sum_{i=1}^{N}(y_i - \bar{y})} \tag{5.49}$$

The systematic measurement errors consist the sensor and conversion errors, including the uncertainties of calculating parameters using correlations. The systematic measurements error sources B_i are combined to form the total systematic uncertainty B using the root-sum-square method according to equation (5.50). [15]

$$B = \sqrt{\sum B_i^2} \tag{5.50}$$

The total error for the measured parameter is calculated by combining the single measurement errors using the sensitivity analysis. If the measured parameter y is a function f of different single parameters x_i, the total measurement error for that parameter is defined by equation (5.51). [15, 12]

$$U_y = \sum \left| \frac{\partial f}{\partial x_i} U_i \right| \tag{5.51}$$

Finally the relative error for the measured parameter y is calculated with equation (5.52), where R is the best estimate for that parameter calculated with function f using the mean values. The standard ISO5801:2007 specifies allowable relative un-

certainties for different measurement parameters. [12]

$$u_y = \frac{U_y}{R} \tag{5.52}$$

6. MEASUREMENT RESULTS

In this chapter the results from the measurements are presented. The presented results are mainly in the form of operation and performance curves. The results from friction measurements are presented in the beginning of the chapter and then the operation curves followed by the efficiency curves. The calculated measurement errors are presented at the end of the chapter. The measurement results for the pump operation and performance curves have been calculated according to the standard ISO 5801:2007 and the calculation procedure presented in Chapter 5. The measurement results have not been filtered or processed.

6.1 Results of friction power measurements

The friction power measurements were conducted with the original heavy bearing unit and with the lighter ball bearing unit. The lighter bearing unit was in use with all the presented efficiency measurement results. All the friction power measurements were done after a warm-up period of one hour and with the impeller detached. In the bearing friction power measurement the seal was removed and only the bearings were present.

The measurement accuracy with the old bearing unit was significantly worse than with the new ball bearing unit. In order to improve the measurement accuracy, the original heavy bearing unit was replaced with a lighter one and the shaft lining was checked with a laser. The inverter controlling the electric motor was switched to a newer version ABB ACS-800 from the old version ACS-300. The newer inverter has DTC torque control and the old has regular PWM torque control. The improvement in the friction torque measurement can be seen in Figures 6.1 and 6.2.

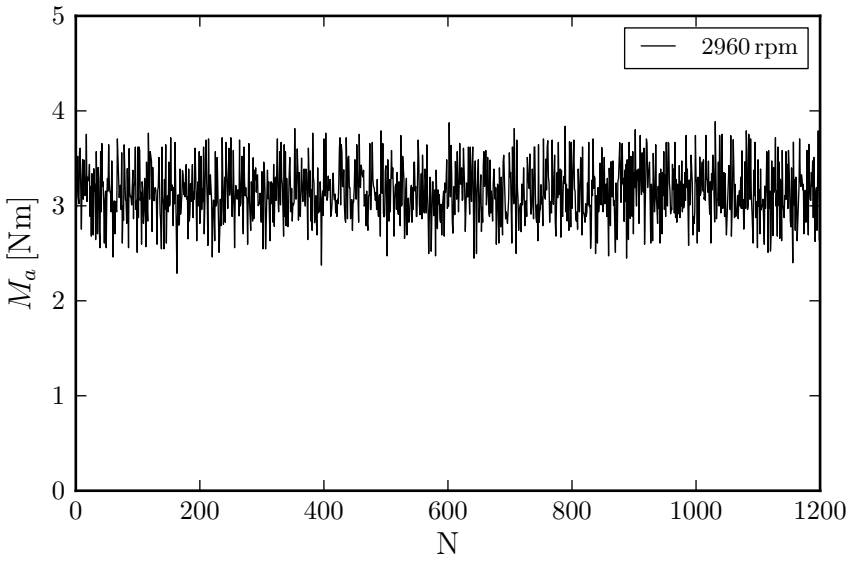

Figure 6.1: *Friction torque of seal and bearing unit, heavy bearing with ACS-300.*

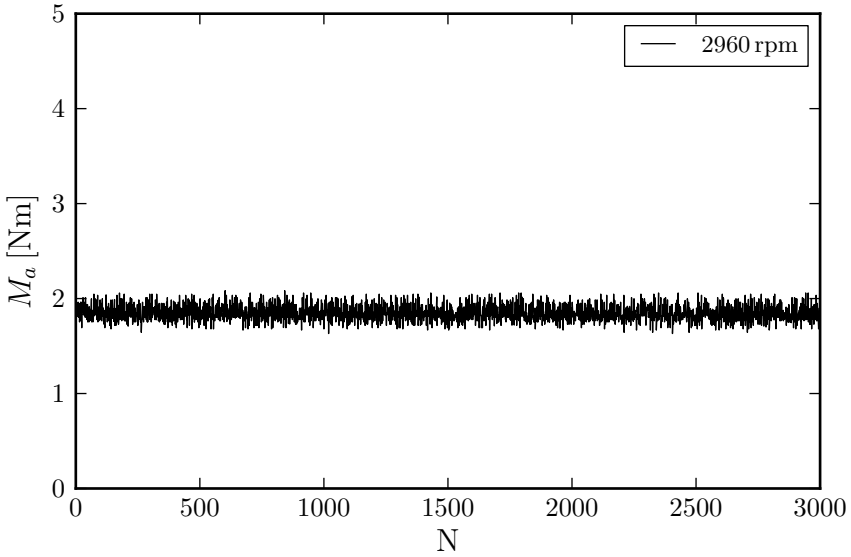

Figure 6.2: *Friction torque of seal and bearing unit, light bearing with ACS-800.*

The results using the old heavy bearing unit are presented in Table 6.1 and the results using the lighter bearing unit are presented in Table 6.2. The friction power P_{fric} is calculated by multiplying the measured torque with the rotational speed according to equation (3.6). The seal friction power P_{seal} is calculated by subtracting the bearing friction power P_{bear} from the total friction power according to equation (5.41).

The friction losses with the lighter bearing unit are smaller than the friction losses with the heavy bearing unit, which was expected. However, the results in Table 6.2 show that the measured total friction power for the seal and bearing unit is too high

compared to the air power. This is confirmed by comparing the results of the torque based efficiency measurement in Figure 6.8 to the results of the thermodynamic efficiency measurement presented in Figure 6.9.

The friction power measurements using the torque transducer are not suitable for measuring the total friction power of the seal and the bearing unit, because the radial load on the bearings doesn't exceed the minimum load specified by the bearing manufacturer. If the radial load is below the minimum specified value, the bearings are not operating correctly and the balls of the bearing can slide instead of rolling. This results in the high friction power values presented in Tables 6.1 and 6.2. [24]

With water there is more radial and axial load on the bearings and the minimum load is exceeded more easily, but with small pumps the radial load in the design point can still be inadequate. If the bearings are not operating correctly, they will eventually be damaged. The torque based friction power and efficiency measurement is therefore not suitable for measuring the friction power of a bearing unit which is operating below the minimum specified radial load on the bearings.

Table 6.1: *Friction power losses with the heavy bearing unit and double mechanical seal at different rotational speeds.*

n [rpm]	P_{fric} [W]	P_{bear} [W]	P_{seal} [W]
2960	975	350	625
2210	608	208	400
1470	290	51	239

Table 6.2: *Friction power loss compared to measured shaft power at BEP with impeller 1 with the light bearing unit and double mechanical seal at different rotational speeds.*

n [rpm]	P_{fric} [W]	$P_{a,1}$ W
2960	572	1059
2660	490	858
2360	412	781
2060	341	614
1760	275	509
1470	227	409

6.2 Pump operation curves

The measured pump operation curves with air with impeller 1 and 2 are presented in Figures 6.3 and 6.4. The operation curves were measured for both impellers and with different settings for the gap size.

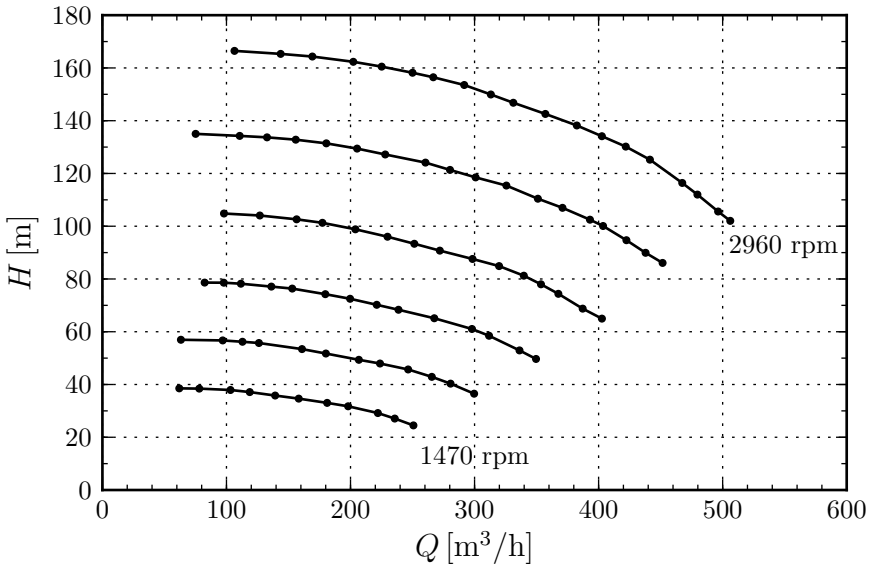

Figure 6.3: *Pump operation curves with air at different rotational speeds with impeller 1. Rotational speed interval between the curves is* 300 rpm *starting from* 2960 rpm.

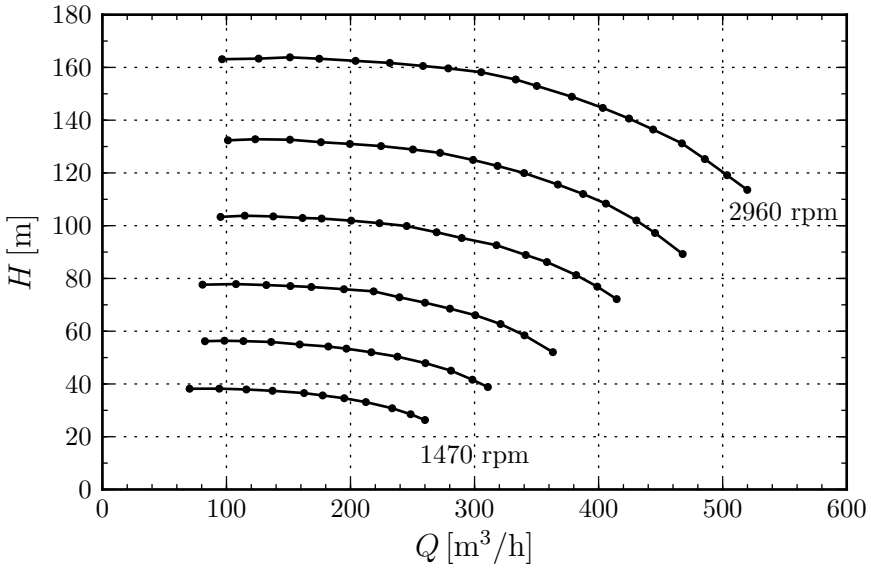

Figure 6.4: *Pump operation curves with air at different rotational speeds with impeller 2. Rotational speed interval between the curves is* 300 rpm *starting from* 2960 rpm.

Impeller 2 produces slightly flatter operation curves compared to impeller 1 and it also produces higher hydraulic head at higher flow rates. The behavior of the operation curves with both impellers is consistent throughout the rotational speed range. The measured results confirm that the pump can be used as fan without any modifications and the pump operation is steady with air.

The comparison of the operation curves between air and water is presented in Figure 6.5 and the comparison between the impellers in Figure 6.6. The comparison between air and water is done only with impeller 1, because the reference water operation curve is measured using the same impeller. The reference operation curve is converted to lower rotational speeds using the affinity laws presented in equations (2.3) and (2.4).

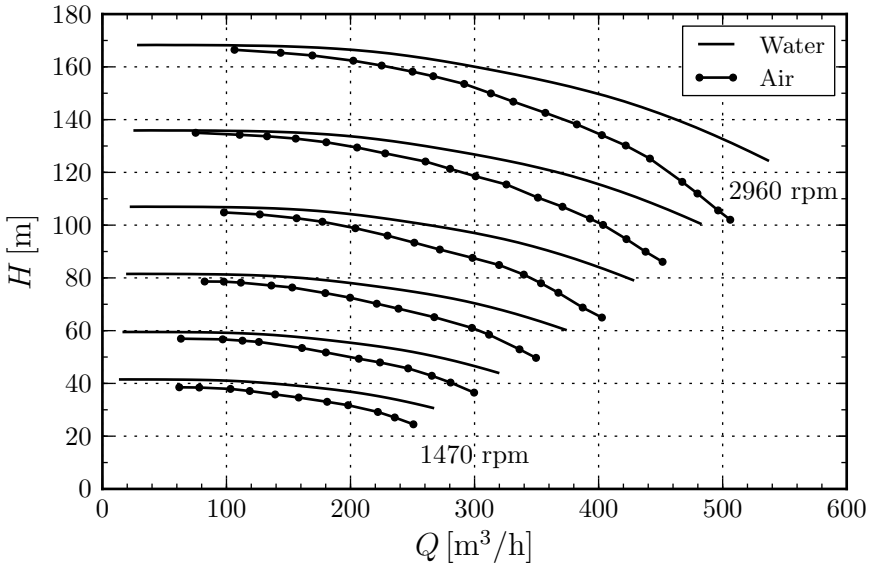

Figure 6.5: *Pump operation curves with air and water at different rotational speeds with impeller 1. Rotational speed interval between the curves is* 300 rpm *starting from* 2960 rpm.

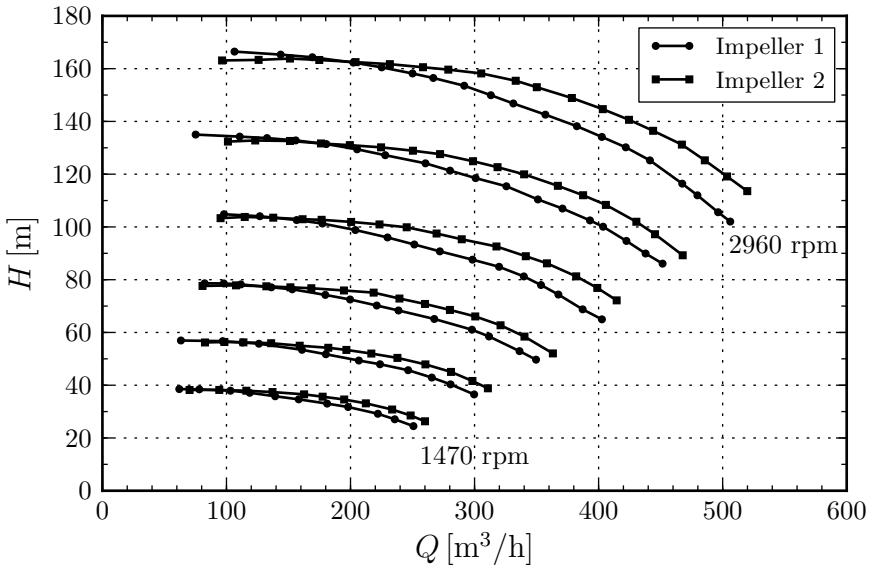

Figure 6.6: *Pump operation curves at different rotational speeds with impeller 1 and impeller 2. Rotational speed interval between the curves is* 300 rpm *starting from* 2960 rpm.

The operation curves presented in Figure 6.5 show that the achievable hydraulic head with air is lower compared to water and the difference increases as the volumetric flow rate increases. The results show that there are differences in the operation curves between air and water although the effect is not dramatic. Similar results have been found when pump operation with water has been compared to pump operation with a fluid with a higher kinematic viscosity. The scale of the differences in operation curves is however larger than what is predicted from the difference in viscosity. [9]

The difference between the impellers is visible in the operation curves presented in Figure 6.6. Higher hydraulic head with increasing volumetric flow rate is achieved with impeller 2. The results suggest that the amount of slip and velocity non-uniformity at the impeller outlet is reduced using the extra half length blades. The reduced slip results in a higher hydraulic head according to equation (3.22).

The effect of the gap size between the casing and the impeller on the operation curves is presented in Figure 6.7. The effect of the gap size was measured with both impellers and the result measured with impeller 1 is shown. The gap setting 0,5 mm is the normal operation setting and the gap setting 1,0 + mm corresponds to setting the gap fully open.

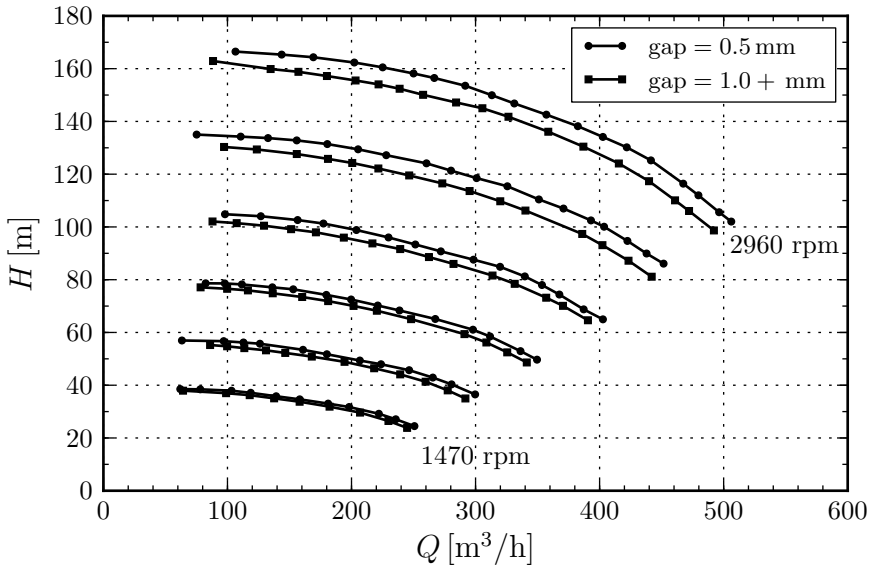

Figure 6.7: *Pump operation curves at different rotational speeds with impeller 1 with different gap sizes. Rotational speed interval between the curves is* 300 rpm *starting from* 2960 rpm*.*

The larger gap size has a similar effect at all volumetric flow rates. Increasing the gap size lowers the achievable hydraulic head and volumetric flow rate by a small margin. The larger gap size increases the volumetric losses and enhances the secondary flows over the impeller blades from pressure side to suction side.

6.3 Pump efficiency curves

The efficiency curves measured with the torque measurement method with air at 2960 rpm with impeller 1 and 2 are presented in Figure 6.8 and the efficiency curves measured with the thermodynamic method are presented in Figure 6.9. The efficiency level measured with air using the torque method is low with both impellers compared to the reference efficiency level measured with water, but the efficiency level measured with the thermodynamic method is close to the reference efficiency level.

The fan efficiency level measured with the torque method is not correct. This assumption is confirmed by comparing the measured efficiency level to the reference level and to the fan efficiency measured with the thermodynamic method, which is presented in Figure 6.9. The maximum attainable efficiency for centrifugal fans in the market is between 70 % and 85 %, which also indicates that the measured efficiency level with torque method is wrong [8, 21]. The low fan efficiency level with the torque based measurement results from the incorrect friction power measurements.

The best efficiency point shifts to a lower volumetric flow rate with the thermodynamic method compared to the torque method. With the torque method the best

efficiency point is at the same volumetric flow rate as the reference best efficiency point with water.

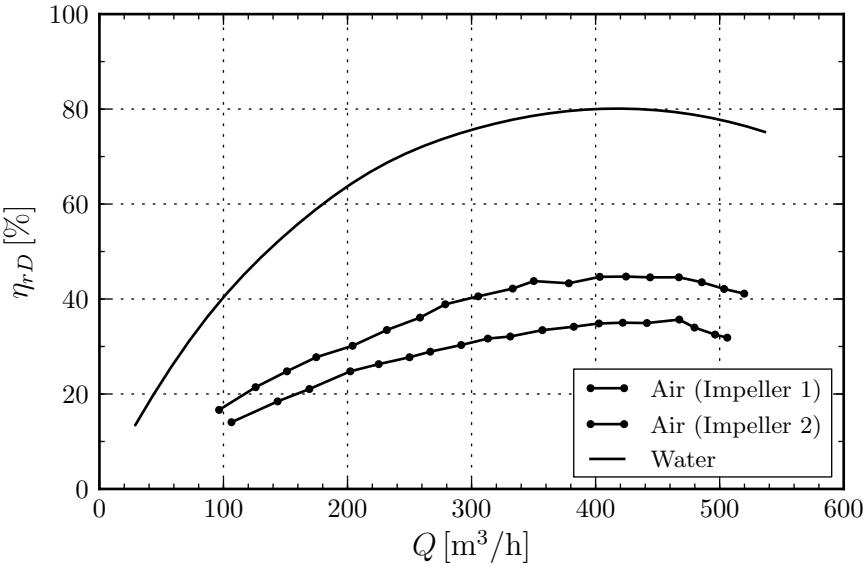

Figure 6.8: *Fan efficiency curves at* 2960 rpm *with impeller 1 and 2 measured with torque method compared to reference efficiency curve with water. Maximum fan efficiency with impeller 1 is* 35,01 % *at* $Q = 421{,}9\,\mathrm{m^3/h}$ *and with impeller 2* 44,73 % *at* $Q = 424{,}5\,\mathrm{m^3/h}$.

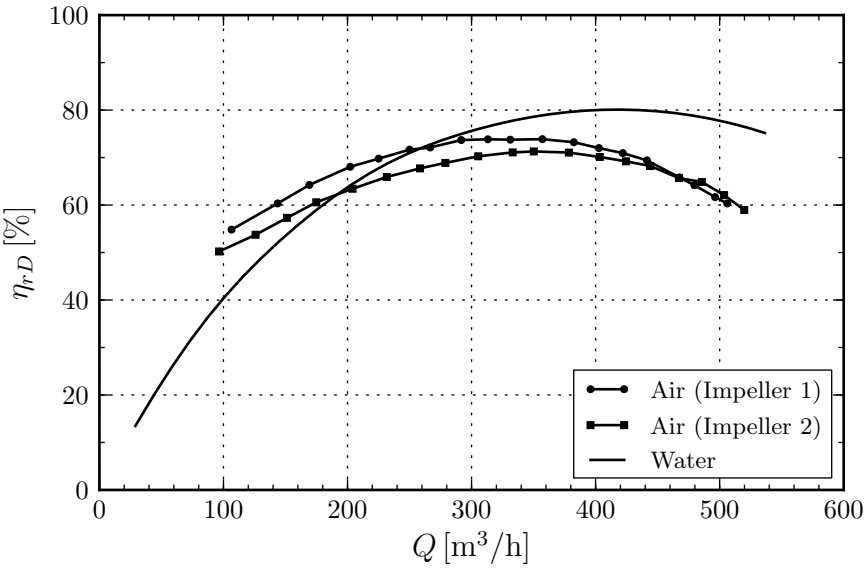

Figure 6.9: *Fan efficiency curves at* 2960 rpm *with impeller 1 and 2 measured with thermodynamic method compared to reference efficiency curve with water. Maximum fan efficiency with impeller 1 is* 73,87 % *at* $Q = 357{,}1\,\mathrm{m^3/h}$ *and with impeller 2* 71,29 % *at* $Q = 350{,}2\,\mathrm{m^3/h}$.

The effect of the gap size between the impeller and casing on fan efficiency measured with impeller 1 is presented in Figure 6.10. The result shows that the larger gap size decreases the fan efficiency by a small margin. The effect is similar at all volumetric flow rates.

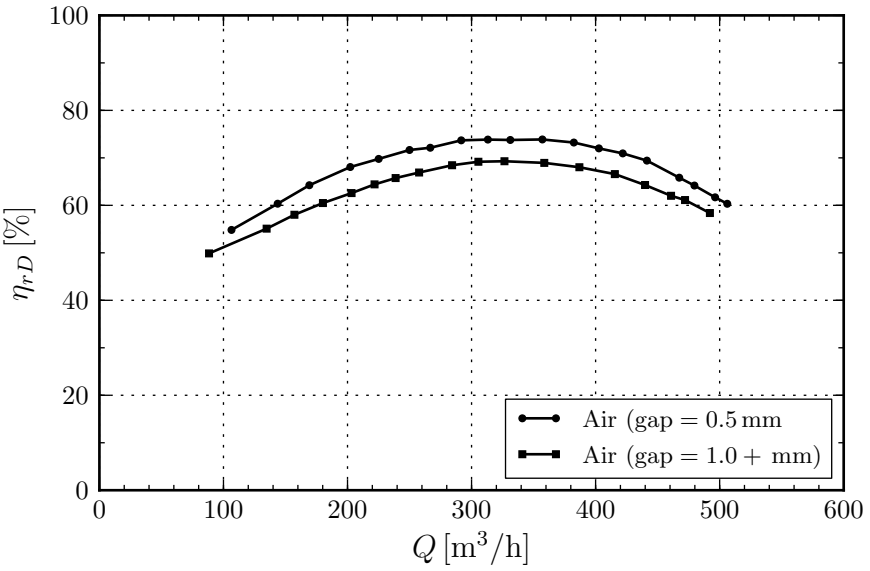

Figure 6.10: *Fan efficiency curves at* 2960 rpm *with impeller 1 measured with thermodynamic method with different gap size.*

The results from the efficiency measurements using the thermodynamic method confirm that the efficiency with air is at the same level as with water. The fan efficiency is better with impeller 1 at smaller flow rates, but the difference decreases at higher flow rates. The difference in the fan efficiency between the impellers is small considering the overall measurement accuracy of the measurement system.

The difference between the different measurement methods is large and the efficiency level with the torque method is not correct. Based on the measurements it seems that the thermodynamic method is more suitable for measuring the fan efficiency, if the friction losses cannot be determined reliably.

6.4 Error analysis

The measurement errors of the relevant directly measured parameters are presented in Table 6.3. The errors are calculated by averaging the errors of different measurement curves. The relative errors of calculated variables are presented in Table 6.4.

Table 6.3: *Measurement errors of selected direct measurement variables.*

Variable	Relative error u [±%]
p_{e7}	8,0
p_{e5}	2,9
p_{e3}	2,4
p_{e4}	16,2
n	0,1
M_a	8,5
T_a	0,5
h_u	3,0
p_a	1,5
T_1	1,0
T_2	0,9

Table 6.4: *Measurement errors of selected calculated measurement variables.*

Variable	Relative error u [±%]
p_{fD}	10,4
P_r (torque)	15,3
P_r (thermodynamic)	13,4
P_{uD}	33,9
q_m	11,5
η_{rD} (torque)	59,6
η_{rD} (thermodynamic)	47,3

The error analysis shows that the problematic measurements are the upstream pressure p_{e4} and the torque measurement M_a. Also the measurement accuracy of the volumetric flow rate is not good due to high errors in the pressure measurements. The high errors in the directly measured variables lead to high errors in the calculated measurement parameters in Table 6.4.

The error analysis shows that the measurement accuracy of the fan efficiency is unacceptably high and the results should be used with caution. The efficiency measurement with the torque transducer failed, because the radial load on the bearings was not sufficient and the bearing unit was not operating correctly. The random error of the shaft torque measurement might also be affected by the incorrect operation of the bearing unit. The measurement error of the impeller power with the thermodynamic method is slightly lower, but the efficiency calculation suffers from the bad accuracy of the air power measurement.

The overall measurement accuracy of the system is not satisfactory, but it could

be significantly improved with better sensors, especially with better pressure sensors. The random errors and the systematic errors are both equally high. The systematic errors could be influenced with better equipment and the random errors with better planning of the measurement.

7. CONCLUSIONS

This chapter consists of the conclusions about the results. The theoretical results and the measurement results are discussed and in the end suggestions are made about future research possibilities.

7.1 Theoretical consideration

The overall conclusion from the results of this thesis is that the separation of turbomachinery into pumps and fans is quite artificial from the perspective of fluid dynamics. The perceived separation arises from the different mechanical construction of the devices. The mechanical difference results from the only major difference between the fluids – the density. The higher density of water means that more power have to used in pumping of water compared to pumping of air.

The density difference also creates a difference in the pressure level as can be seen from the equation (2.34), where the pressure gradient is scaled by the density of the fluid. Because of the higher pressure level, thicker impeller blades and a thicker pump casing have to be used. The mechanical differences between pumps and fans are the result of structural needs and not the result of different hydrodynamic behavior between air and water.

The only property that causes differences in the hydrodynamic behavior is the viscosity of the fluid. The theoretical analysis in Chapter 2 shows that air has higher kinematic viscosity than water and the difference is only in the order of one decade, not three. This implies that the compared fluids are quite similar in the perspective of fluid dynamics.

The impeller design presented in Chapter 3 verifies that the design of a pump or a fan is not influenced by the properties of the fluid. This is because the conventional design of a pump relies on one-dimensional theory of the fluid flow. The minor influence of the fluid viscosity is highlighted by the fact that fluid viscosity is not included in the definition of the specific speed, which can be called the most important dimensionless pump parameter. The only difference in the pump design is the lack of cavitation with air. In the perspective of the hydraulic design, a pump or a fan is the same device and the geometric design is the same if the fluid viscosity is ignored. The slip factor is the only parameter which takes flow non-uniformity and viscous effects into account and the effect of fluid viscosity on the slip factor is

not entirely known.

The similarity in the pump geometry doesn't mean that the flow behavior of air and water is similar. A simple flat plate boundary layer analysis done in Chapter 2 provides some insight to the differences. The lower kinematic viscosity of air results in a significantly lower Reynolds number of the flow with air compared to the flow with water. The dominance of the turbulent viscosity in turbulent flows decreases the functional differences between the fluid viscosities as long as the turbulence level is adequate.

The boundary layer analysis shows that when the Reynolds number decreases, the effect of the fluid viscosity increases. The flat plate Reynolds number is lower by definition if the flow velocity or the channel length decreases or the fluid kinematic viscosity increases. This implies that the effects caused by a low Reynolds number are visible in a device of the same size with air but not necessary with water. It also means that the effects might not be visible in large devices, but could be present in small devices.

The possible effects of the low Reynolds number are the increased length of the laminar region of the boundary layer and the easier separation of the boundary layer. The transition of the flow from laminar to turbulent depends on multiple things including the surface roughness, the pressure gradient and the turbulence intensity of the outer flow. The effect of transition is hard to predict and calculate and it is usually neglected since the boundary layer is assumed to be fully turbulent. This assumption needs to be considered carefully especially with fans but also with small pumps.

The separation of the boundary layer causes losses in the hydraulic efficiency, because the forming back flow region generates high velocity gradients and thus increases the viscous dissipation. Separating flow can cause unexpected behavior and the operation curves can be affected. The flow separation is influenced by many factors including the pressure gradient and the streamline curvature of the surface.

The effect of the surface roughness was studied separately with the boundary layer analysis. The effect of the surface roughness is important with small devices, because the relative amount of the disk friction losses in the total hydraulic losses increases as the size of the device decreases. The analysis in Chapter 2 shows that for a smooth surface the friction coefficient of the flow is higher with air than with water. The difference in the friction coefficient between the fluids vanishes when a hydraulically rough surface is used. A surface is hydraulically rough, if the roughness elements penetrate through the viscous sublayer. The surface roughness always increases the friction coefficient and the total boundary thickness increases. The use of surface finishing should be considered for all the wetted surfaces inside a turbo-machine in order to minimize the disk friction losses.

7.2 Measurement results

The pump operation with water and air using the same device has not been studied exclusively in the past. The design and construction of the measurement system provided an invaluable insight to fan and pump measurements and to flow measurements. The measurement system succeeded in the task it was designed for, but the measurement accuracy could have been better.

The measurement results for the pump with air show that a centrifugal pump can be used as a fan without any modifications. The operating curves presented in Chapter 6 show that the pump operation with air is steady and consistent throughout the rotational speed range. The difference in the operating curves between air and water seems to increase when the volumetric flow rate increases. The differences are also larger at higher rotational speeds. This indicates that the difference in the operation is somehow related to the flow velocity inside the pump.

The effect of disk friction increases as the speed of the impeller surface increases, but it cannot explain the dependency on the volumetric flow rate. It is suspected that the increased kinematic viscosity in addition to the possible flow separation and recirculation is causing the difference in the pump operation between air and water. This assumption is backed up by the fact that the operation curve with impeller 2 is flatter.

The extra half length blades on the impeller outer diameter can improve the blade congruence of the flow and prevent recirculation in the outer triangle of the impeller channel according to Chapter 2. The reduced slip increases the perpendicular velocity component of the flow and the generated pressure rises according to equation (2.32). The improved pressure generation of impeller 2 compared to impeller 1 can be seen in Figure 6.6. This implies that the extra half length blades are beneficial at least with air.

The effect of the size of the gap between the impeller and the pump casing on pump operation is noticeable but the effect is small. The increased gap size increases the volumetric losses and lowers the achievable hydraulic head of the pump. The effect is similar at all volumetric flow rates.

The measurement of the pump efficiency with air proved to be difficult due to incorrect operation of the bearing unit. The torque method is not suitable for measuring the fan efficiency if the radial load on the bearings is not adequate. The rated minimum radial load on the bearings depends on the bearing type and size and the required level is not met when air is used. The correct operation of the bearing unit should be confirmed when the torque measurement method is used.

The thermodynamic efficiency measurement method proved to be successful. The quality of the efficiency measurements using the thermodynamic method are good

compared to the torque method. The thermodynamic measurement method is affected by the accuracy of the temperature sensors and the data logger, but it is not affected by the mechanical losses of the seal and bearing unit. The thermodynamic method is thus a more direct way to measure the impeller power. The temperature difference that needs to be measured is very small and the method is unusable with water. The small temperature difference makes the thermodynamic method susceptible to unknown error caused by heat transfer.

The problem with the efficiency measurements accuracy is the high measurement error of the air power. It is caused by the poor accuracy of the pressure sensors of the measurement system. The uncertainties in the measurement of the flow rate and in the pressure measurements accumulate and the relative error of the efficiency measurement is high. The results of the thermodynamic efficiency measurements are qualitatively good and the efficiency level is correct compared to the reference level measured with water.

The efficiency measurements showed that the efficiency level of the pump with air is similar compared to the efficiency level with water. The measured efficiency level is comparable with the efficiency levels of existing centrifugal fans. The measured efficiency difference between the impellers is small and decreases at higher volumetric flow rates. The larger gap size between the impeller and casing decreased the fan efficiency at all volumetric flow rates by a small margin.

The observed shift of the best efficiency operation point to a lower flow rate could be caused by the calculation method of the thermodynamic efficiency. The recovery factor used in the equation (5.47) affects the stagnation enthalpies and the effect is larger at high volumetric flow rate because the flow velocity increases. The effect of the recovery factor on the temperature measurement should be studied further.

7.3 Suggestions for future research

The effects of the low Reynolds number of flows in fans and small pumps should be studied further. The flow separation in the impeller channel could be studied using advanced CFD-methods. The CFD-calculations provide an interesting tool to study the complex flow behavior inside the pump. The possible flow separation with air is suspected to be the main cause for the operational difference between air and water. The possible transition effects of the boundary layer should be studied together with the flow separation. The measurable difference between the impellers should also be studied further.

The current pump design method where the impeller and volute are designed separately should be replaced by a coupled method at least in the CFD phase of the design process. The coupled model increases the complexity of the design but it should be used in order in further improve the hydraulic efficiency of small pumps,

because the importance of secondary flow effects and minor losses is higher with small devices.

The effect of surface roughness can be studied experimentally by measuring the same impellers with different surface finishing levels. The surface roughness effects can be measured with air and the results should be directly applicable to flow with water.

Measurements are needed in all of the suggested future research topics. The complexity of the fluid flow in turbo-machines necessitates the use of experiments for validation purposes, because the CFD-methods are not reliable enough. The accuracy of the existing measurement system could be improved by acquiring better pressure and temperature sensors and by revising the measurement method. The existing system is otherwise perfectly suitable for future research.

As a final conclusion it is suggested that a new experimental measurement system is built using the existing measurement system as a basis. The new measurement system should include a turbo-machine, which has been designed for the purpose and thus the geometry is known. This enables the simultaneous use of CFD and measurements to study the flow in a turbo-machine. If possible, the device should built from acrylic in order to enable the use of PIV-measurements for validation purposes. The future research can improve the overall understanding of the fluid flow in a pump and at the same time improve the CFD-methods used in the pump design process.

REFERENCES

[1] ABB Oy. *Firmware Manual, ACS800 Standard Control Program 7.x.* http://www05.abb.com/global/scot/scot201.nsf/veritydisplay/6f96ed70e1b467a9c12578f80034ed25/$file/EN_ACS800_Standard_FW_L.pdf. Accessed June 19, 2013.

[2] Alnor Oy. *Digitaali-Psykrometri ALNOR Therm2246-2, Käyttöohje.*

[3] Anderson, H. *Centrifugal Pumps and Allied Machinery*, 4th ed. Elsevier, Oxford, 1994. 486 p.

[4] ANSYS, Inc. *ANSYS® Academic Research, Release 14.5, Help System, FLUENT User's Guide.*

[5] Cengel, Y. A., and Boles, M. A. *Thermodynamics: An Engineering Approach*, 6th ed. McGraw-Hill, New York, 2008. 1018 p.

[6] Datum Electronics Ltd. *M420 Rotary Torque Transducers.* http://www.datum-electronics.co.uk/files/documents/Datum%20M420.pdf. Accessed June 19, 2013.

[7] Dixon, S. L., and Hall, C. A. *Fluid Mechanics and Thermodynamics of Turbomachinery.* Elsevier/Butterworth-Heinemann, Oxford, 2010. 459 p.

[8] Fläkt Woods Group. *Direct driven single inlet fans.* http://www.flaktwoods.com/products-services/buildings/products/ventilation-solutions/fans-and-ventilation/centrifugal-fans/direct-driven-single-inlet-fans/. Accessed September 24, 2013.

[9] Gülich, J. F. *Centrifugal Pumps*, 2nd ed. Springer, Heidelberg, 2010. 964 p.

[10] Huba Control AG. *Relative, and differential pressure transmitter type 699.* http://www.hubacontrol.com/fileadmin/user_upload/domain1/Produkte/EN/Datenblatt/699_pressure_sensor.pdf. Accessed June 19, 2013.

[11] International Organization for Standardization. *ISO 5167-2:2003 Measurement of fluid flow by means of pressure differential devices inserted in circular cross- section conduits running full. Part 2: Orifice plates*, 2003.

[12] International Organization for Standardization. *ISO 5801:2007 Industrial fans - Performance testing using standardized airways*, 2007.

[13] International Organization for Standardization. *ISO 9906:2012 Rotodynamic pumps - Hydraulic performance acceptance tests - Grades 1, 2 and 3*, 2012.

[14] Koivikko, M. *Modelling the Effect of Geometric Parameters on the Performance and Efficiency of Centrifugal Pump Impellers.* Doctoral Dissertation, Tampere University of Technology, Tampere, 2006.

[15] Lee, T.-W. *Thermal and Flow Measurements*, 1st ed. CRC Press, Boca Raton, 2008. 390 p.

[16] Mills, A. F. *Basic Heat & Mass Transfer*, 2nd ed. Prentice Hall, New Jersey, 1999. 1000 p.

[17] Neumann, B. *The Interaction Between Geometry and Performance of a Centrifugal Pump*, 1st ed. Mechanical Engineering Publications, London, 1991. 311 p.

[18] Nokeval Oy. *TRE-sarjan lämpötila-anturit.* `http://www.nokeval.com/pdf/datasheets/fi/TRE-sarjan_anturit.pdf`. Accessed June 19, 2013.

[19] Outinen, H., and Salmi, T. *Lujuusopin perusteet*, 1st ed. Pressus Oy, Tampere, 2004. 464 p.

[20] Peck, J. F. Investigations conserning flow conditions in a centrifugal pump, and the effect of blade loading on head slip. *Proceedings of the Institution of Mechanical Engineers 164* (1951).

[21] Ronnila, M. *Keskipakopuhaltimen juoksupyörän laskenta.* Master's Thesis, Tampere University of Technology, Tampere, 1993.

[22] Schetz, J. A. *Boundary Layer Analysis*, 1st ed. Prentice-Hall, New Jersey, 1993. 586 p.

[23] Schlichting, H., and Gersten, K. *Boundary-Layer Theory*, 8th ed. Springer, Heidelberg, 2000. 799 p.

[24] SKF Group. *SKF Ball bearings, Minimum load.* `http://www.skf.com/group/products/bearings-units-housings/ball-bearings/deep-groove-ball-bearings/single-row-deep-groove-ball-bearings/minimum-load/index.html`. Accessed September 24, 2013.

[25] Sulzer Pumps Ltd. *AHLSTAR End Suction Single Stage Centrifugal Process Pumps.* `http://www.sulzer.com/en/-/media/Documents/ProductsAndServices/Pumps_and_Systems/Single_Stage_Pumps/`

Brochures/AHLSTAREndSuctionSingleStage_E10083.pdf. Accessed June 19, 2013.

[26] Sulzer Pumps Ltd. *Sulzer DocsOnline Product Document Library*. http://docsonline.sulzer.com. Accessed June 19, 2013.

[27] Sulzer Pumps Ltd. *Sulzer Select Online Pumps Selection Tool*. http://www.sulzer.com/fi/Products-and-Services/Pumps-Services/Special-Functionalities-Pumps/Sulzer-Select-Welcome-Page. Accessed June 19, 2013.

[28] Sulzer Pumps Ltd. *Centrifugal Pump Handbook*, 3rd ed. Butterworth-Heinemann, Winterthur, 2010. 289 p.

[29] Versteeg, H. K., and Malalasekera, W. *An Introduction to Computational Fluid Dynamics*, 2nd ed. Pearson Education Limited, Harlow, 2007. 503 p.

[30] White, F. M. *Viscous Fluid Flow*, 3rd ed. McGraw-Hill, New York, 2006. 629 p.

APPENDIX 1: IMPELLER DIMENSIONS

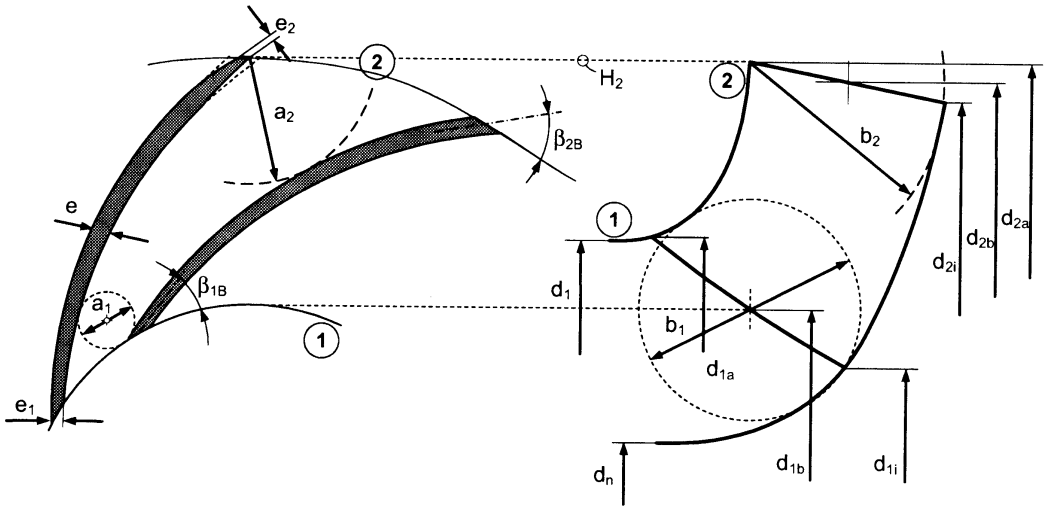

Figure L1.1: *Impeller dimensions [9].*

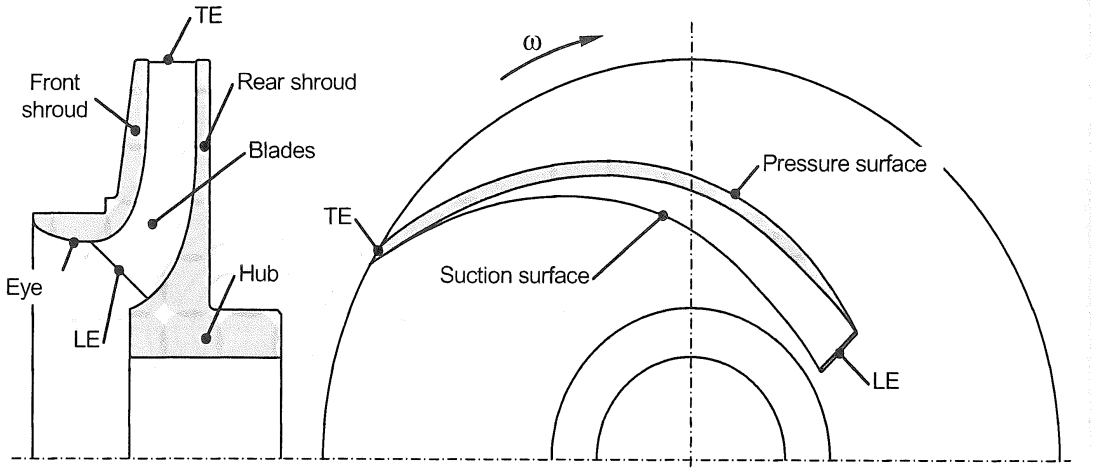

Figure L1.2: *Side section and plan view [9].*

APPENDIX 2: CAD-DRAWINGS OF MEASUREMENT SYSTEM PARTS

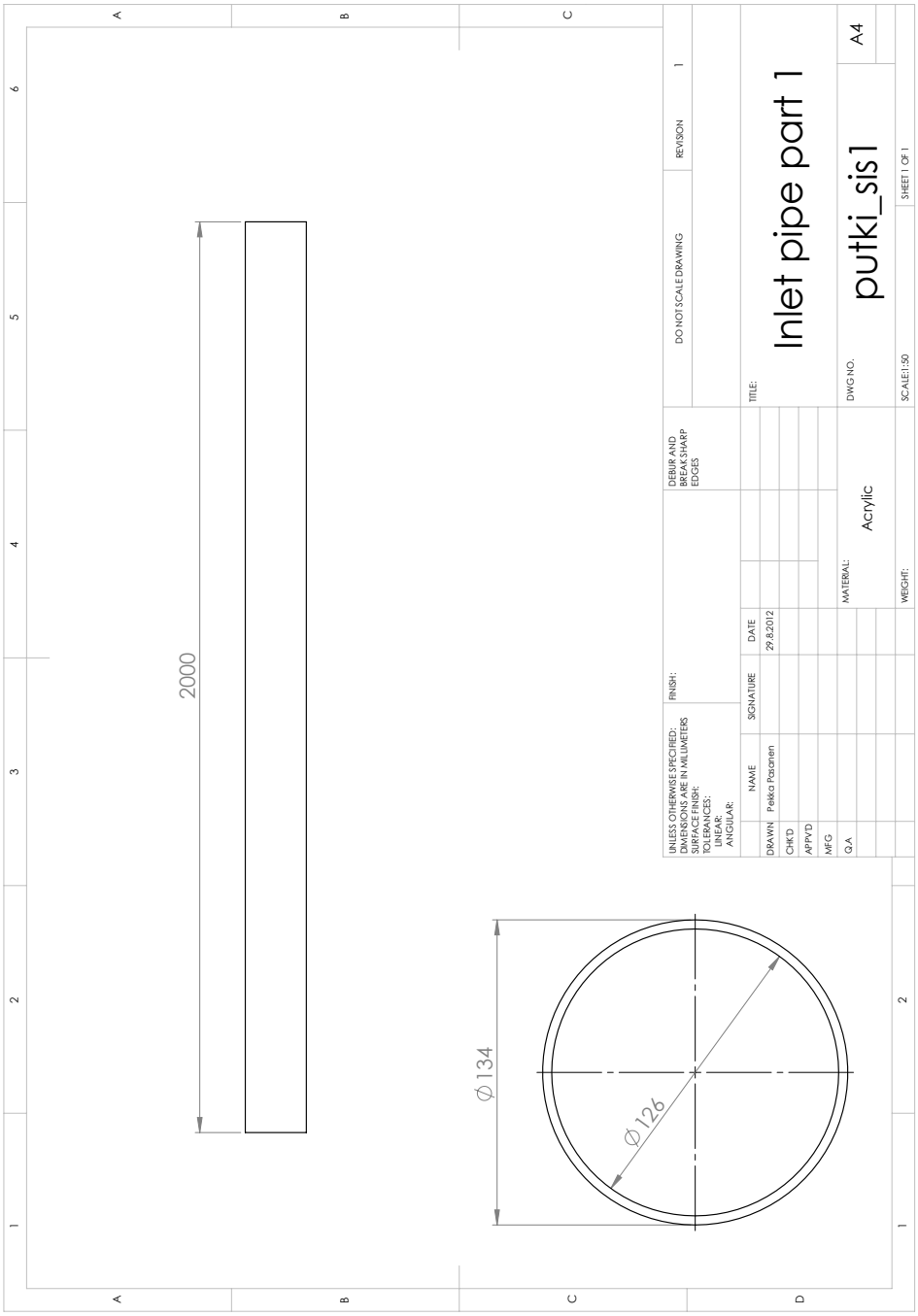

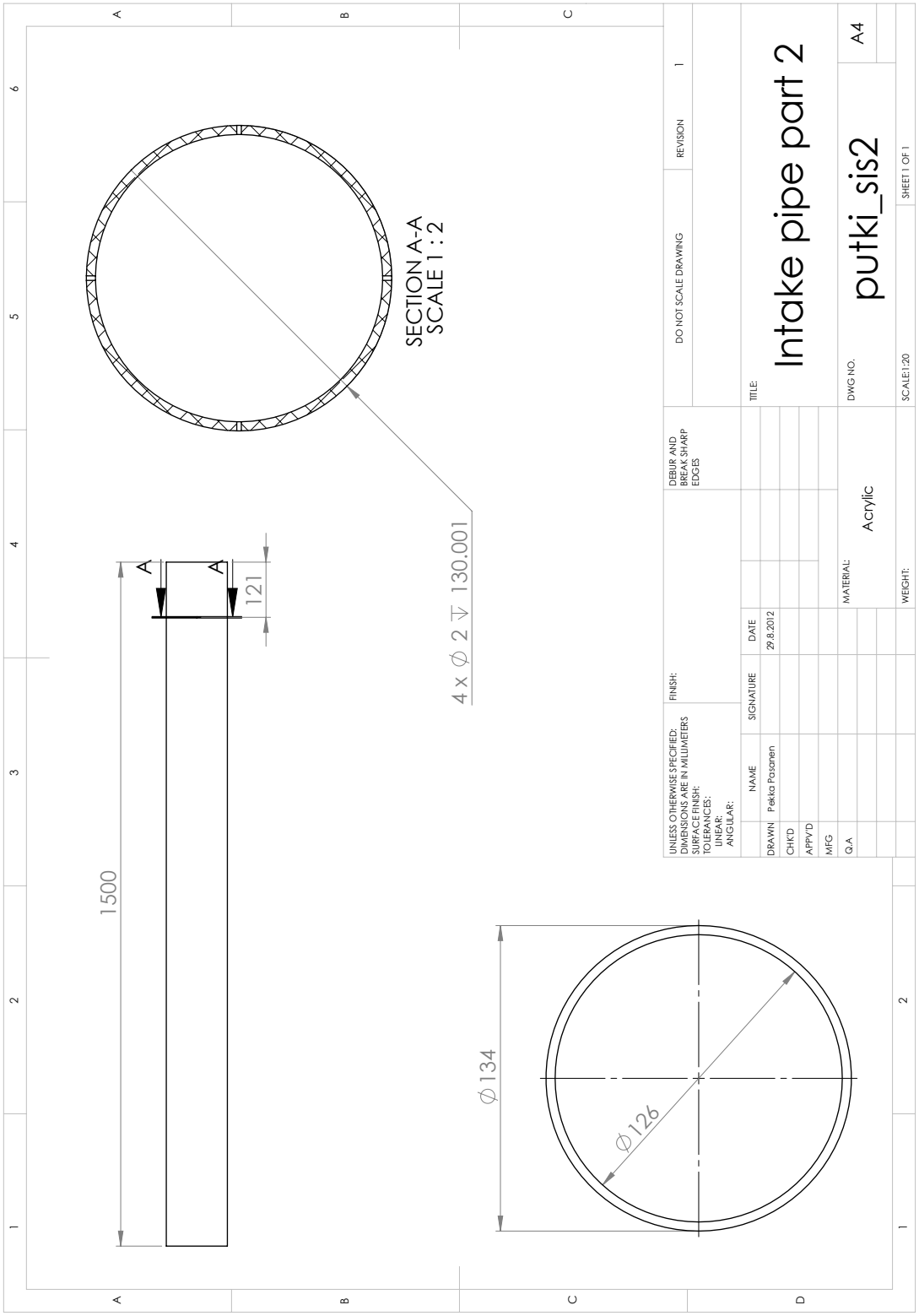
SECTION A-A
SCALE 1 : 2
4 x ∅ 2 ∓ 130.001
121
1500
∅134
∅126
A
A
Intake pipe part 2
putki_sis2
A4
Acrylic
DO NOT SCALE DRAWING
REVISION 1
DEBUR AND BREAK SHARP EDGES
FINISH:
UNLESS OTHERWISE SPECIFIED:
DIMENSIONS ARE IN MILLIMETERS
SURFACE FINISH:
TOLERANCES:
LINEAR:
ANGULAR:
NAME
SIGNATURE
DATE
DRAWN Pekka Pasanen 29.8.2012
CHK'D
APPV'D
MFG
Q.A
MATERIAL:
WEIGHT:
TITLE:
DWG NO.
SCALE:1:20
SHEET 1 OF 1

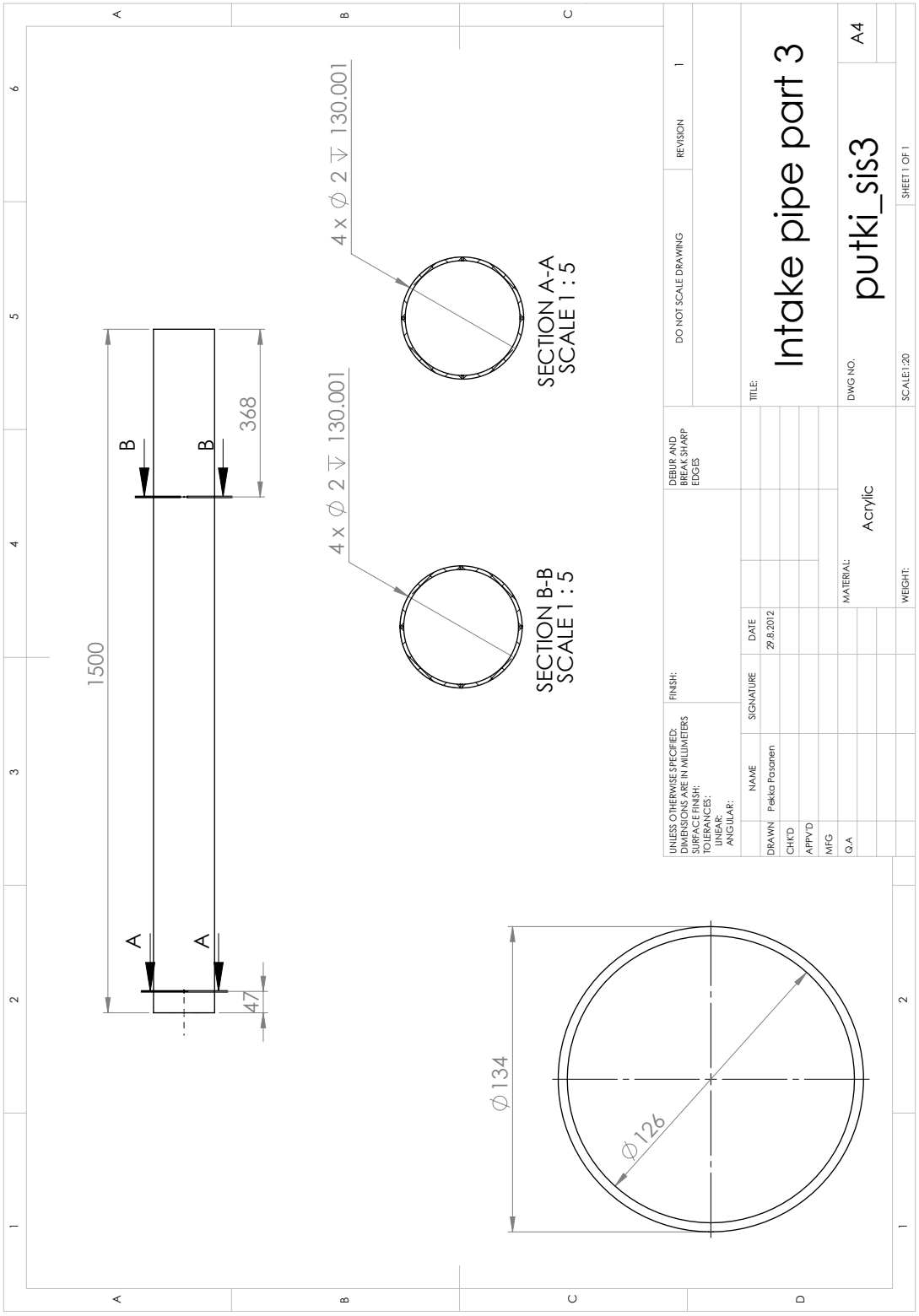
1500
368
47
B
B
A
A
4 x ⌀ 2 ⩛ 130.001
SECTION A-A
SCALE 1 : 5
4 x ⌀ 2 ⩛ 130.001
SECTION B-B
SCALE 1 : 5
⌀134
⌀126
UNLESS OTHERWISE SPECIFIED:
DIMENSIONS ARE IN MILLIMETERS
SURFACE FINISH:
TOLERANCES:
LINEAR:
ANGULAR:
FINISH:
DEBUR AND BREAK SHARP EDGES
DO NOT SCALE DRAWING
REVISION 1
NAME
SIGNATURE
DATE
DRAWN Pekka Pasanen 29.8.2012
CHK'D
APPV'D
MFG
Q.A
MATERIAL: Acrylic
WEIGHT:
TITLE: Intake pipe part 3
DWG NO. putki_sis3
A4
SCALE:1:20
SHEET 1 OF 1

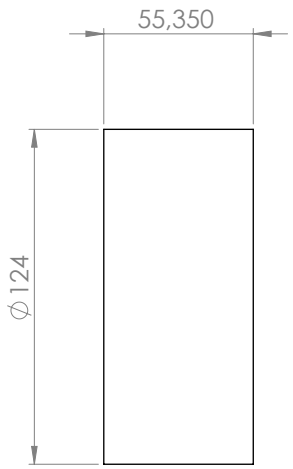

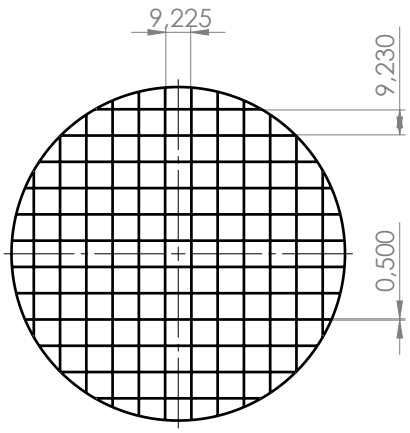

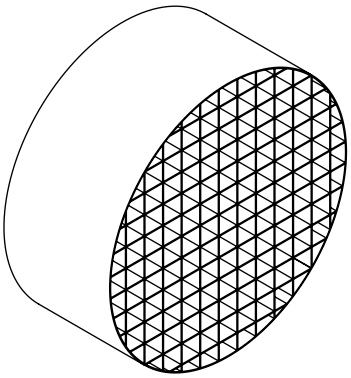

UNLESS OTHERWISE SPECIFIED: DIMENSIONS ARE IN MILLIMETERS SURFACE FINISH: TOLERANCES: LINEAR: ANGULAR:		FINISH:		DEBUR AND BREAK SHARP EDGES		DO NOT SCALE DRAWING	REVISION 1
	NAME	SIGNATURE	DATE			TITLE: AMCA cell type flow straightener	
DRAWN	Pekka Pasanen		3.7.2012				
CHK'D							
APPV'D							
MFG							
Q.A				MATERIAL: 1060 Alloy		DWG NO. amca	A4
				WEIGHT:		SCALE:1:2	SHEET 1 OF 1

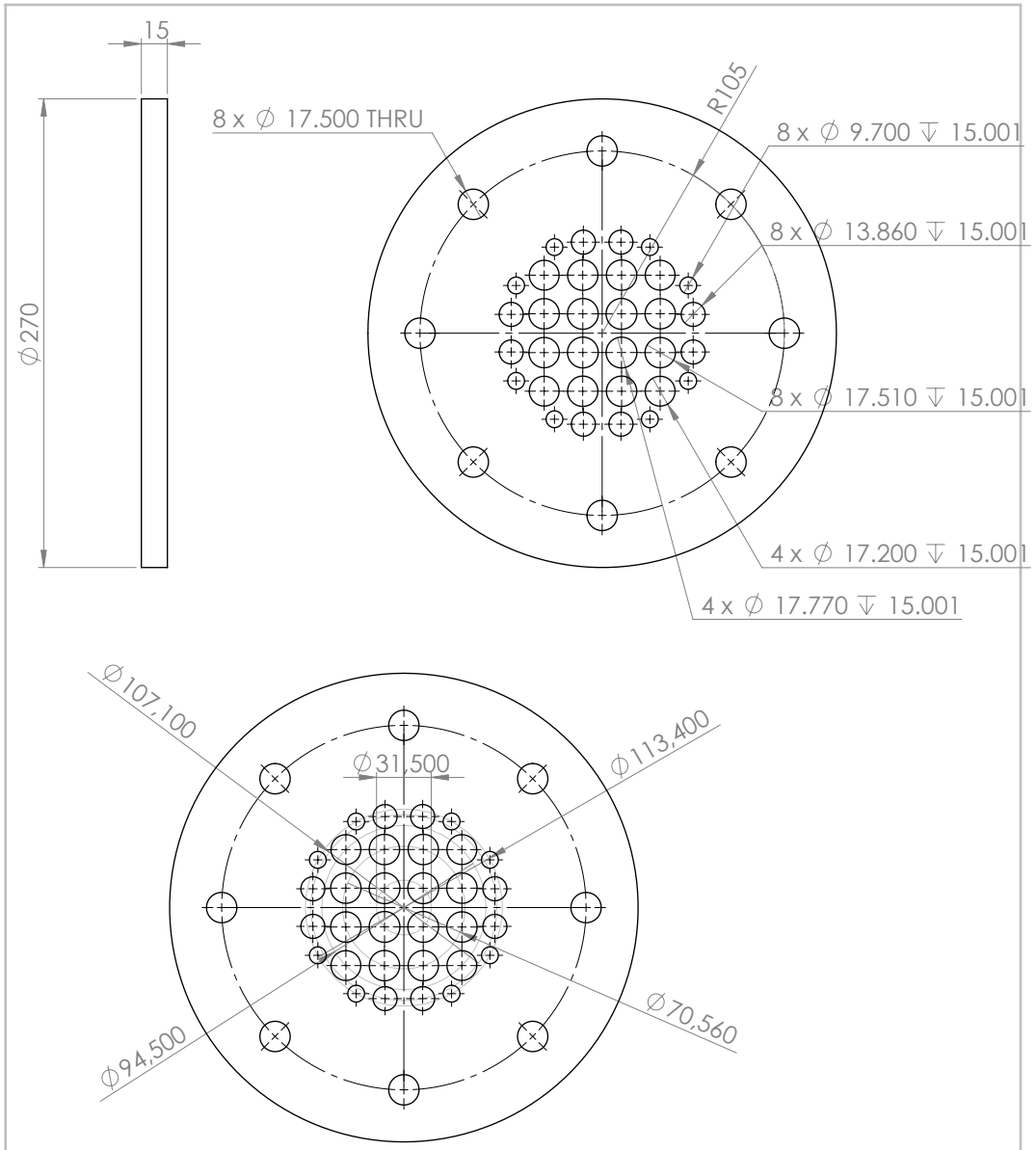

UNLESS OTHERWISE SPECIFIED: DIMENSIONS ARE IN MILLIMETERS SURFACE FINISH: TOLERANCES: LINEAR: ANGULAR:	FINISH:		DEBUR AND BREAK SHARP EDGES	DO NOT SCALE DRAWING	REVISION 1	
	NAME	SIGNATURE	DATE	TITLE: Zanker flow conditioner plate		
DRAWN	Pekka Pasanen		29.8.2012			
CHK'D						
APPV'D						
MFG						
Q.A				MATERIAL: Acrylic	DWG NO. zanker	A4
				WEIGHT:	SCALE:1:5	SHEET 1 OF 1

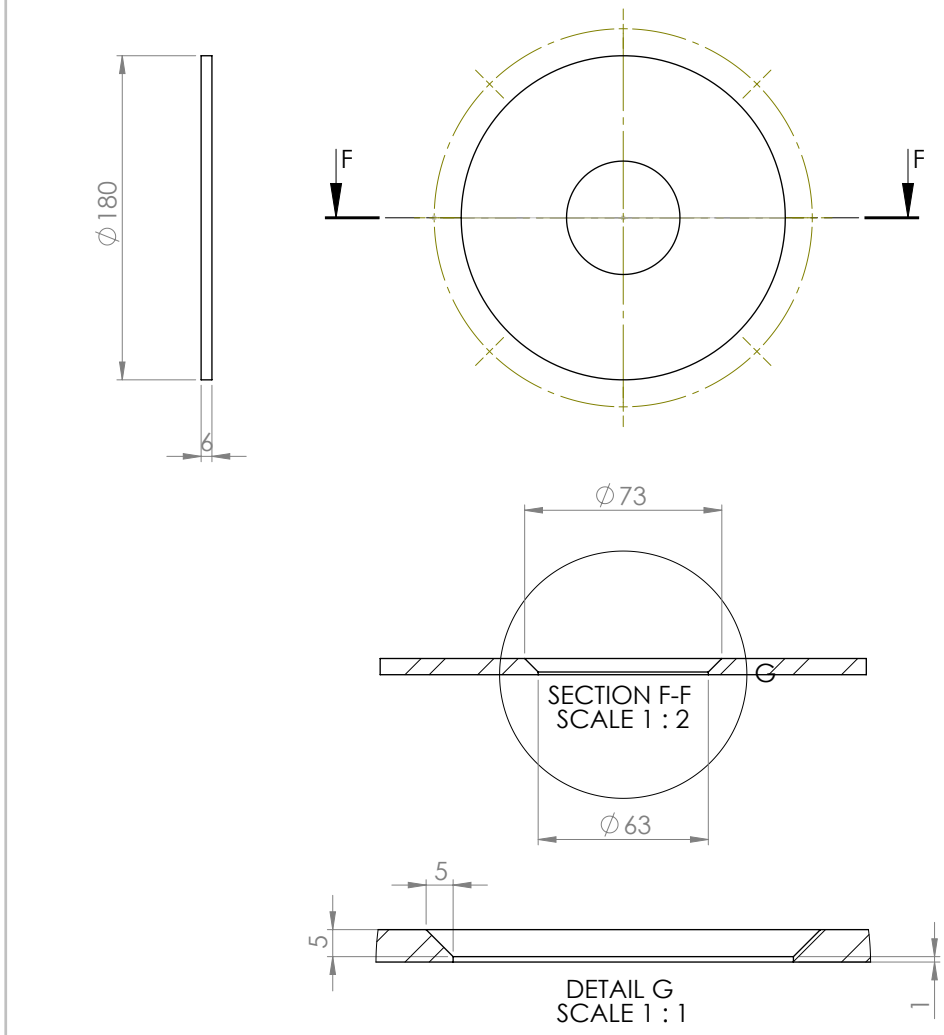

UNLESS OTHERWISE SPECIFIED: DIMENSIONS ARE IN MILLIMETERS SURFACE FINISH: TOLERANCES: LINEAR: ANGULAR:	FINISH:		DEBUR AND BREAK SHARP EDGES	DO NOT SCALE DRAWING	REVISION 2	
	NAME	SIGNATURE	DATE	TITLE: Orifice plate d=63		
DRAWN	Pekka Pasanen		29.8.2012			
CHK'D						
APPV'D						
MFG						
Q.A				MATERIAL: Plain carbon steel	DWG NO. kuristuslaippa	A4
				WEIGHT:	SCALE:1:5	SHEET 1 OF 1

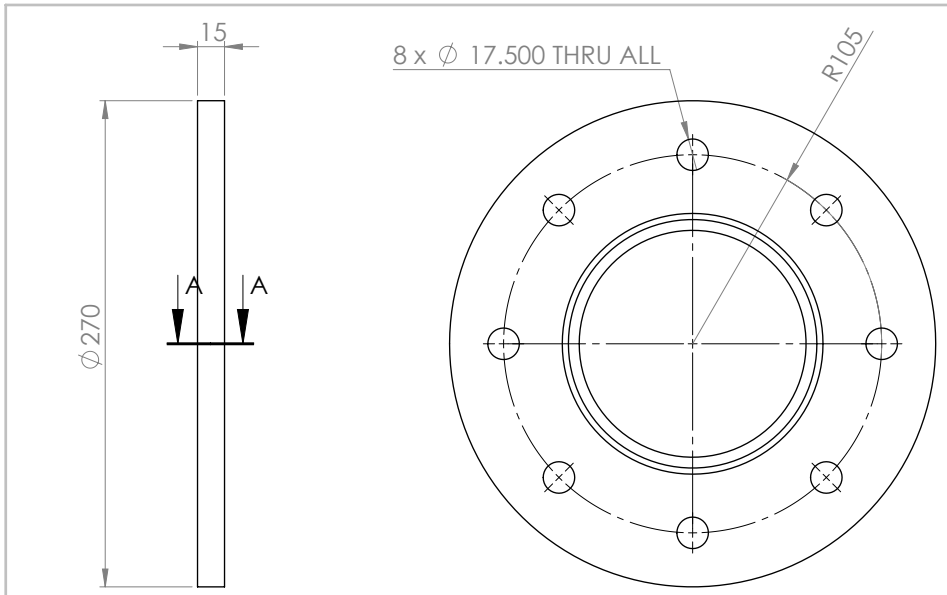

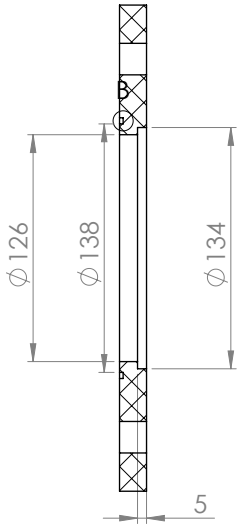

SECTION A-A
SCALE 1 : 3

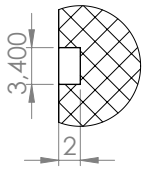

DETAIL B
SCALE 2 : 1

UNLESS OTHERWISE SPECIFIED: DIMENSIONS ARE IN MILLIMETERS SURFACE FINISH: TOLERANCES: LINEAR: ANGULAR:	FINISH:		DEBUR AND BREAK SHARP EDGES	DO NOT SCALE DRAWING	REVISION 1	
	NAME	SIGNATURE	DATE	TITLE:		
DRAWN	Pekka Pasanen		29.8.2012	Intake pipe flange		
CHK'D						
APPV'D						
MFG						
Q.A				MATERIAL: Acrylic	DWG NO. laippa	A4
				WEIGHT:	SCALE:1:5	SHEET 1 OF 1

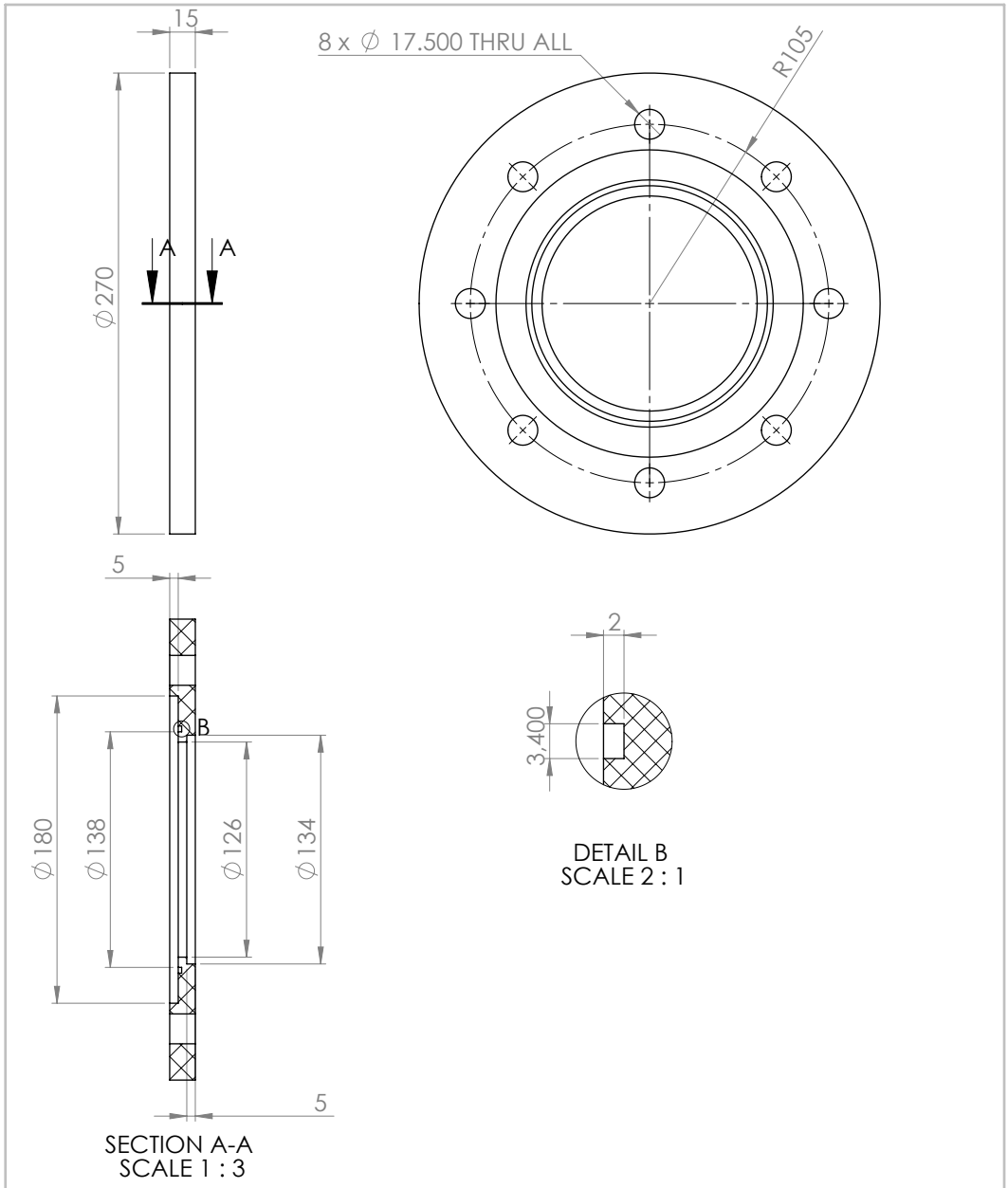
15
8 x ∅ 17.500 THRU ALL
R105
A
A
∅270
5
B
∅180
∅138
∅126
∅134
5
SECTION A-A
SCALE 1 : 3
2
3,400
DETAIL B
SCALE 2 : 1
UNLESS OTHERWISE SPECIFIED:
DIMENSIONS ARE IN MILLIMETERS
SURFACE FINISH:
TOLERANCES:
LINEAR:
ANGULAR:
FINISH:
DEBUR AND BREAK SHARP EDGES
DO NOT SCALE DRAWING
REVISION 2
NAME SIGNATURE DATE
DRAWN Pekka Pasanen 29.8.2012
CHK'D
APPV'D
MFG
Q.A
MATERIAL: Acrylic
WEIGHT:
TITLE: Intake pipe flange, orifice plate
DWG NO. laippa_kuristuslevy
A4
SCALE:1:5
SHEET 1 OF 1

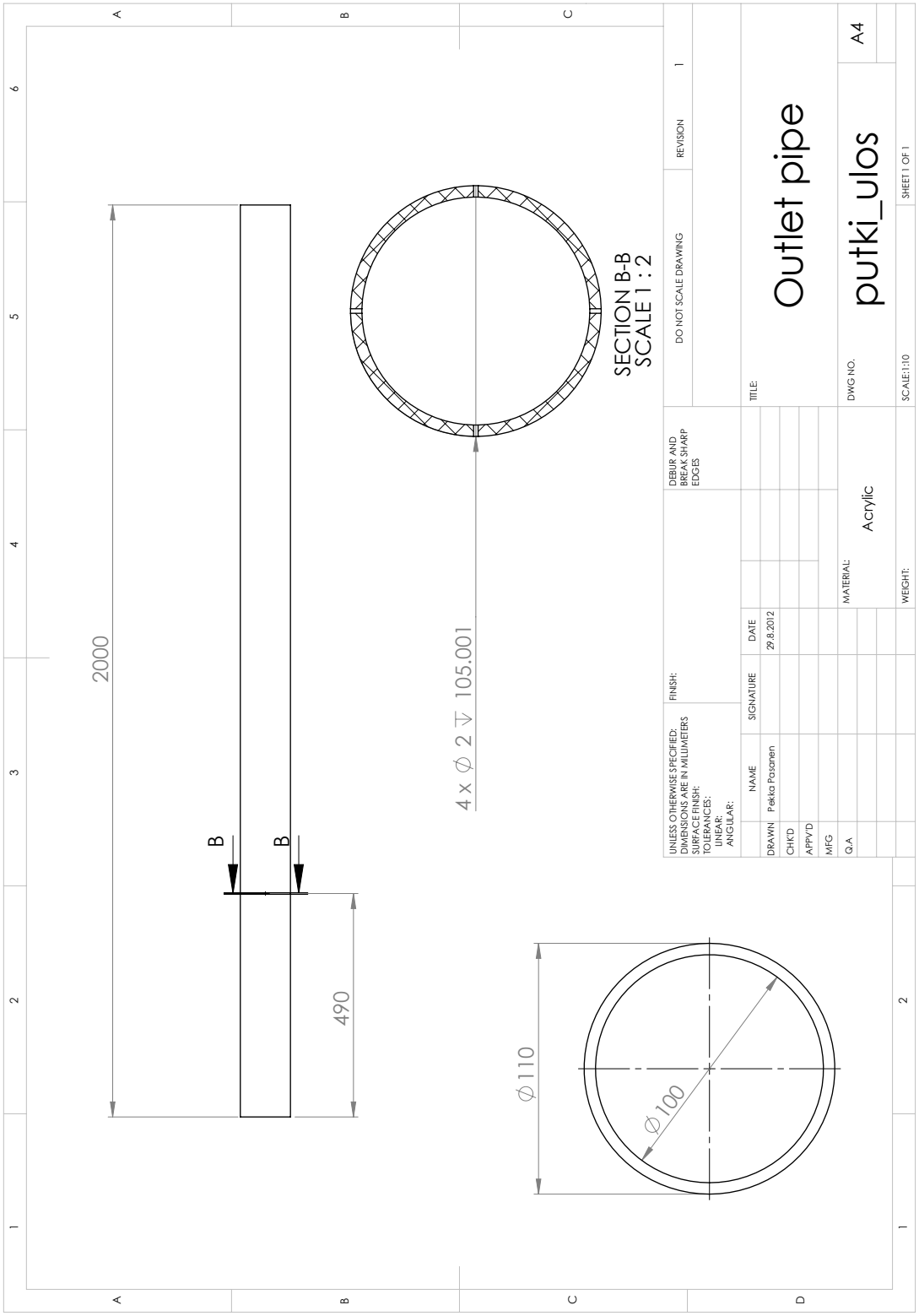
SECTION B-B
SCALE 1 : 2
2000
490
B
B
4 x ⌀ 2 ↧ 105.001
⌀110
⌀100
Outlet pipe
putki_ulos
A4
Acrylic
DO NOT SCALE DRAWING
DEBUR AND BREAK SHARP EDGES
UNLESS OTHERWISE SPECIFIED:
DIMENSIONS ARE IN MILLIMETERS
SURFACE FINISH:
TOLERANCES:
LINEAR:
ANGULAR:
FINISH:
NAME
SIGNATURE
DATE
DRAWN Pekka Pasanen
29.8.2012
CHK'D
APPV'D
MFG
Q.A
MATERIAL:
WEIGHT:
SCALE:1:10
SHEET 1 OF 1
DWG NO.
REVISION
TITLE:

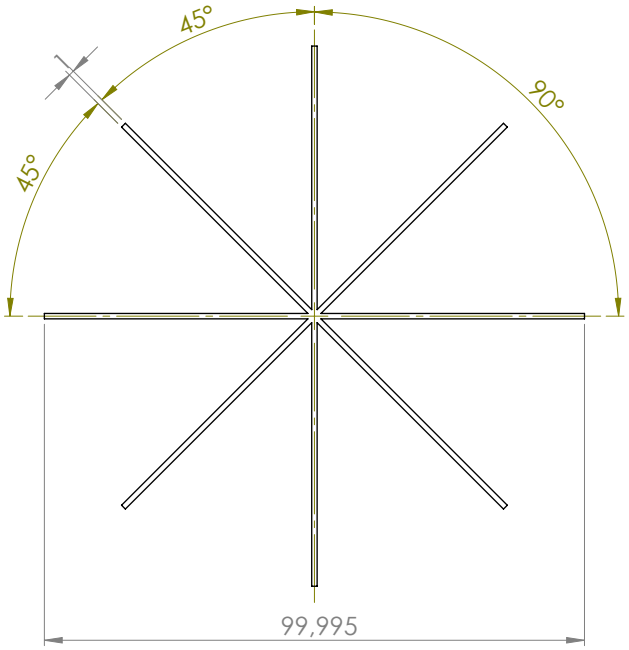

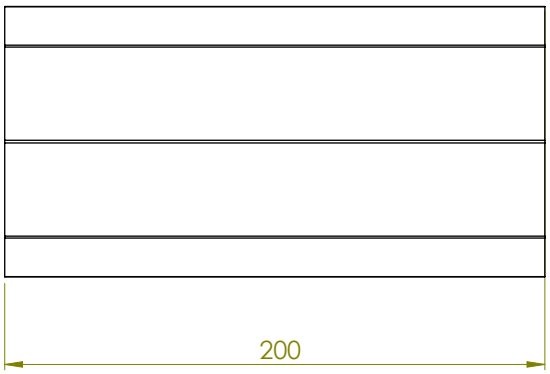

UNLESS OTHERWISE SPECIFIED: DIMENSIONS ARE IN MILLIMETERS SURFACE FINISH: TOLERANCES: LINEAR: ANGULAR:	FINISH:		DEBUR AND BREAK SHARP EDGES	DO NOT SCALE DRAWING	REVISION	2
	NAME	SIGNATURE	DATE	TITLE:	Star type flow straightener	
DRAWN	Pekka Pasanen		29.8.2012			
CHK'D						
APPV'D						
MFG						
Q.A				MATERIAL:	DWG NO.	A4
				1060 Alloy	star	
				WEIGHT:	SCALE:1:5	SHEET 1 OF 1

APPENDIX 3: SCHEMATICS OF MEASUREMENT SYSTEM AND LOCATION OF SENSORS